AD_____

Award Number: **W81XWH-11-1-0593**

TITLE: **Regenerative Stem Cell Therapy for Breast Cancer Bone Metastasis**

PRINCIPAL INVESTIGATOR: **Selvarangan Ponnazhagan, Ph.D.**

CONTRACTING ORGANIZATION: **University of Alabama at Birmingham**
Birmingham, AL 35294-0111

REPORT DATE: **November 2015**

TYPE OF REPORT: **Final Report**

PREPARED FOR: U.S. Army Medical Research and Materiel Command
Fort Detrick, Maryland 21702-5012

REPORT DOCUMENTATION PAGE		Form Approved OMB No. 0704-0188

1. REPORT DATE *(DD-MM-YYYY)*	**2. REPORT TYPE**	**3. DATES COVERED** *(From - To)*
November 2015	Final	09/15/2011 - 08/14/2015

4. TITLE AND SUBTITLE
Regenerative Stem Cell Therapy for Breast Cancer Bone Metastasis

5a. CONTRACT NUMBER
W81XWH-11-1-0593

5b. GRANT NUMBER
BC101411

5c. PROGRAM ELEMENT NUMBER

6. AUTHOR(S)

Selvarangan Ponnazhagan, Ph.D

email: pons@uab.edu

5d. PROJECT NUMBER

5e. TASK NUMBER

5f. WORK UNIT NUMBER

7. PERFORMING ORGANIZATION NAME(S) AND ADDRESS(ES)

University of Alabama at Birmingham
Birmingham, AL 35294-0111

Department of Pathology
1825, University Blvd., SHEL 814
Birmingham, AL 35294-0007

8. PERFORMING ORGANIZATION REPORT

9. SPONSORING / MONITORING AGENCY NAME(S) AND ADDRESS(ES)
U.S. Army Medical Research and Materiel Command
Fort Detrick, MD 21702-5012

10. SPONSOR/MONITOR'S ACRONYM(S)

11. SPONSOR/MONITOR'S REPORT NUMBER(S)

12. DISTRIBUTION / AVAILABILITY STATEMENT **Approved for Public Release; Distribution Unlimited**

13. SUPPLEMENTARY NOTES

14. ABSTRACT

Bone is the most common site of metastasis for human breast cancer (BCa), which results in significant morbidity and mortality in patients with advanced disease. A vicious cycle, arising due to the interaction of BCa cells and cells in the bone microenvironment results in the activation of osteoclasts and increased osteolytic bone destruction. The major treatment to reduce the burden of bone metastasis in BCa patients is bisphosphonate therapy. Despite significant efforts to improve the potency of bisphosphonates, the complications are only retarded but not prevented. Thus, development of newer therapies that can both ameliorate the threshold of bone destruction and increase survival of patients with metastatic breast disease will be highly beneficial. The central hypothesis of the proposed work is bone-targeted delivery of genetically-engineered MSC, over-expressing OPG, will prevent osteolytic bone damage and restore skeletal remodeling. Further, based on the requirement of angiogenesis for tumor growth in primary and metastatic sites, in combination with a systemically stable anti-angiogenic therapy, long-term survival will significantly increase. These hypotheses will be tested in this proposal using an immnocompetent, preclinical mouse model of BCa dissemination to all major bones as in human patients.

15. SUBJECT TERMS
Bone metastasis; osteolysis; osteoprotegerin

16. SECURITY CLASSIFICATION OF:			**17. LIMITATION OF ABSTRACT**	**18. NUMBER OF PAGES**	**19a. NAME OF RESPONSIBLE PERSON**
					USAMRMC
a. REPORT	**b. ABSTRACT**	**c. THIS PAGE**			**19b. TELEPHONE NUMBER** *(include area code)*
U	U	U	UU	64	

Standard Form 298 (Rev. 8-98)
Prescribed by ANSI Std. Z39.18

Table of Contents

Title of the Grant: Regenerative Stem Cell Therapy for Breast Cancer Bone Metastasis
Award number: W81XWH-11-1-0593
Principal Investigator: Selvarangan Ponnazhagan, Ph.D.
Final Report: 09/15/2011 - 09/14/2015

INTRODUCTION

Bone is the most common site of metastasis for human breast cancer (BCa), which results in significant morbidity and mortality in patients with advanced disease. A vicious cycle, arising due to the interaction of BCa cells and cells in the bone microenvironment results in the activation of osteoclasts and increased osteolytic bone destruction. The major treatment to reduce the burden of bone metastasis in BCa patients is bisphosphonate therapy. Despite significant efforts to improve the potency of bisphosphonates, the complications are only retarded but not prevented. Thus, development of newer therapies that can both ameliorate the threshold of bone destruction and increase survival of patients with metastatic breast disease will be highly beneficial. The central hypothesis of the proposed work is bone-targeted delivery of genetically-engineered MSC, over-expressing OPG, will prevent osteolytic bone damage and restore skeletal remodeling. Further, based on the requirement of angiogenesis for tumor growth in primary and metastatic sites, in combination with a systemically stable anti-angiogenic therapy, long-term survival will significantly increase. These hypotheses will be tested in this proposal using an immnocompetent, preclinical mouse model of BCa dissemination to all major bones as in human patients.

Specific Aims:

1) To determine therapeutic effects of genetically-modified MSC, overexpressing OPG, for osteolytic bone damage using a bone-targeted delivery, in an immunocompetent mouse model of BCa dissemination to the bone

2) To determine the combined effect of MSC-OPG therapy with systemically-stable anti-angiogenic therapy for long-term survival.

KEY WORDS

Breast cancer

Bone dissemination

Mesenchymal stem cells

Osteoclasts

Osteolytic damage

Osteoprotegerin

Stem cell therapy

ACCOMPLISHMENTS

Rationale for creating a mutant OPG retaining RANKL binding and devoid of TRAIL binding affinity: Recent breakthroughs in our understanding of osteoclast differentiation and activation have come from the analysis of a family of biologically related tumor necrosis factor (TNF) receptor (TNFR)/TNF-like proteins: Osteoprotegerin (OPG), RANK and RANKL, which together regulate osteoclast function (1). The dysregulation of the functional equilibrium in the OPG/RANK/RANKL triad is responsible for the osteolysis associated with malignant tumors. RANKL has already been detected in several tumor cells and can be considered as a key factor involved in the activation of osteoclasts associated with bone metastases (2). OPG binds RANKL to negatively regulate osteoclast differentiation (3), and has been investigated as a molecular therapeutic to inhibit bone destruction associated with osteolytic bone lesions. OPG also binds TRAIL, a critical effector molecule for tumor immunosurveillance, raising the concern that treatment with OPG might promote tumor cell survival (4). Our goal is to develop a variant of OPG that will bind to RANKL, but not to TRAIL. The specific hypothesis behind the proposed research is that structural interactions exist between TRAIL and OPG that do not take place between OPG and RANKL. In the absence of any solved structure for OPG, our hypothesis is based on the following observations. **First,** TRAIL possesses an insertion of 12 amino acids that forms an elongated loop that is structurally divergent from RANKL. Contacts between this loop and OPG would be excellent targets for this endeavor. **Second,** the residues in the TRAIL receptor Death Receptor 5 (DR5) that make contact with this loop are conserved in OPG. Conserved residues among proteins in the same family are an indication they may have functional importance, so these residues may be important in mediating the interaction of TRAIL with OPG. **Third,** deletion of this loop in TRAIL eliminated binding to DR5 (5). If this mode of interaction is conserved between OPG and TRAIL, then we believe that mutation of the residues in OPG that bind this loop will eliminate or reduce binding of OPG to TRAIL. Because this loop of TRAIL is structurally divergent from RANKL, we hoped that such mutants will retain their ability to bind RANKL. Preliminary studies using such a mutant OPG containing mutation at the amino acid 49, identified based on molecular modeling of OPG, RANKL, TRAIL and its death receptor DR5 resulted in an engineered OPG (**Figure 1**) Testing of the mutant OPG constructs indicated that a few of them retained RANKL binding but not TRAIL binding as provided in **Figure 2**. This mutant OPG was effective in inhibiting osteoclastogenesis as shown in **Figure 2B** and was devoid of significant TRAIL binding affinity, resulting in increased tumor cell apoptosis following treatment with recombinant TRAIL, as shown in **Figure 2C**.

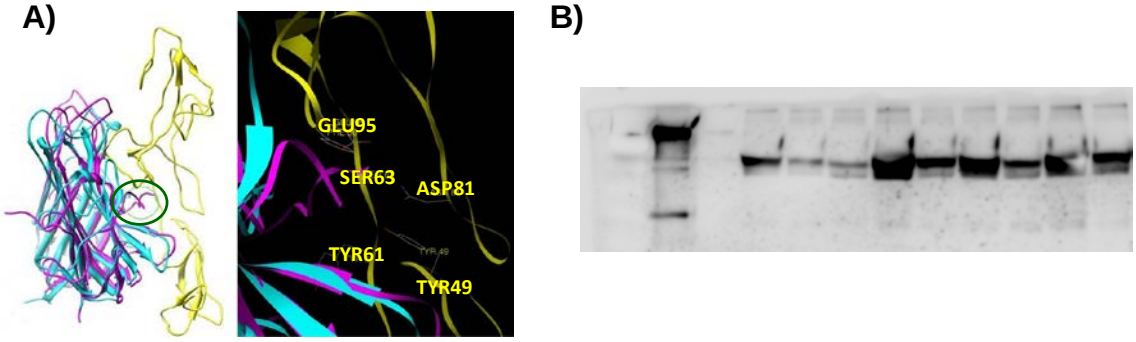

Figure 1. (A) The model of OPG complexed with TRAIL and RANKL. OPG is in yellow, RANKL is blue, and TRAIL is in purple. The AA" loop is circled in green. A close up view of the AA' loop and the interacting amino acids in the central cleft of OPG is shown on the right. **(B)** Immunoblot analysis of wild-type and mutant-OPG**.** 24 hours following transfection of expression plasmids containing the sequences of wild-type and mutant-OPG in 293 cells, supernatant were collected and concentrated using a 30 kDa cut off filter. Equal amounts of protein from indicated supernatant was separated in a SDS-PAGE and transferred to nitrocellulose membrane. Detection of wild-type and mutant-OPG was performed using an antibody for OPG (Jackson ImmunoResearch Laboratories Inc.). From left to right – Recombinant OPG, Negative control (Supernatant), Wild Type OPG, Y49A-OPG, Y49R-OPG, Y61E-OPG, Y81E-OPG, F96A-OPG, F96R-OPG, F107A-OPG, Y114A-OPG

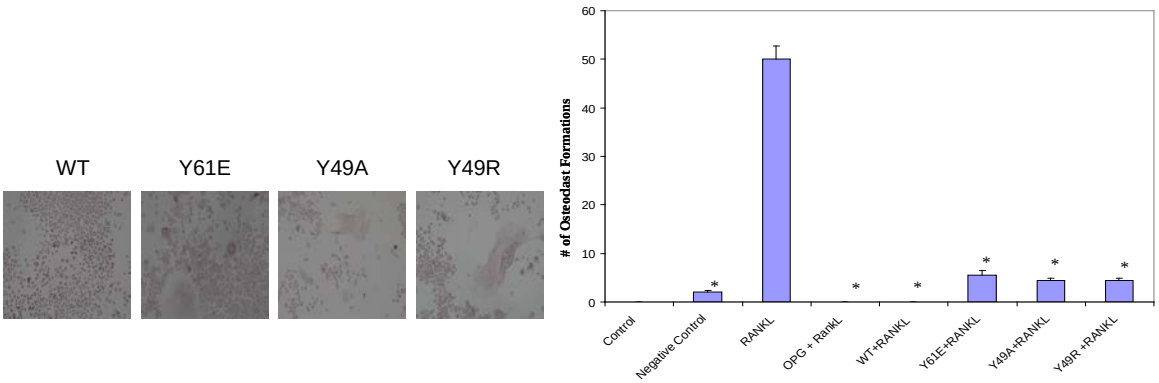

Figure 2. Osteoclast assay for wild-type and mutant-OPG. Tartrate-resistant acid phosphatase (TRAP) staining of RAW 264.7 cells was performed after 7-14 days in the presence of wild-type or mutant OPG and RANKL. As a positive control, RANKL alone was added without OPG. Recombinant protein, wild type as well as mutant OPG were all able to block osteoclastogenesis, which indicates the RANKL binding potential of wild type and mutant OPG. Quantitative analysis based on the number osteoclast seen in 10 random fields. (*p < 0.05)

In vitro TRAIL Assay: To ensure that mut-OPG do not bind to TRAIL, human BCa cell line MDA-MB 435 was cultured with recombinant, wild type and mut-OPG either alone or in combination with TRAIL. After 24 hours, MDA-MB 435 cells were fixed in 3.7% PFA and stained with 0.05% crystal violet for 30 minutes and viewed using a light microscope (100X). Cells were also cultured with 20µl of the solution 3-(4,5-dimethylthiazol-2-yl)-5-(3-carboxymethoxyphenyl)-2-(4-sulfophenyl)-2H-tetrazolium, inner salt (MTS) for 2 hours and then presence of proliferating cells was measured by absorbance at 490nm. Results are shown in Fig. 3.

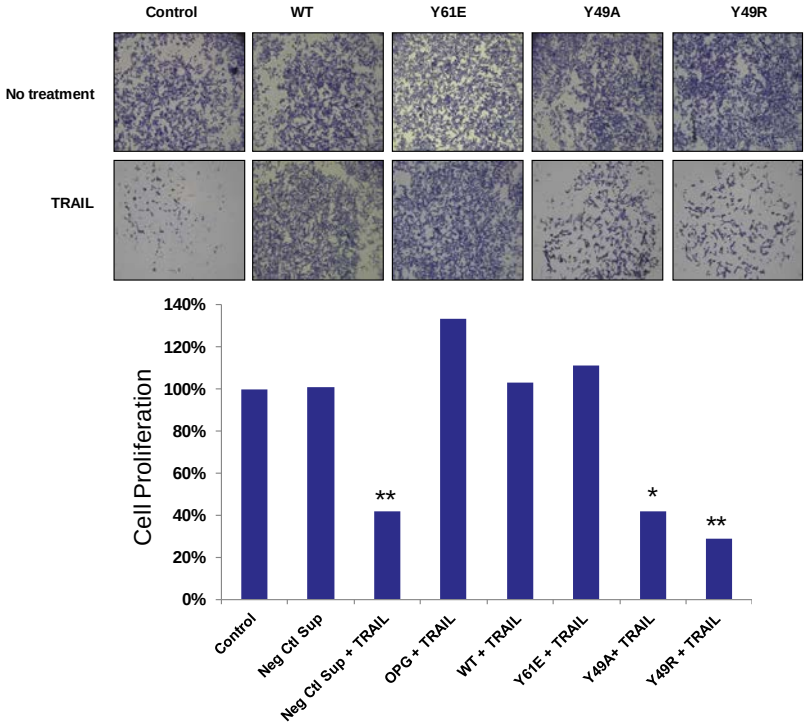

Figure 3. TRAIL assay with wild-type and mut-OPG. MDA-MB 435 cells were cultured in the presence of 100 ng of TRAIL and 400 ng of wild-type or mut-OPG. After 24 hours, MDA-MB 435 cells were either (A) fixed in 3.7% PFA and then stained with 0.05% Crystal violet for 30 minutes and viewed using a light microscope (100X) or (B) cultured with 20 µl of the solution 3-(4,5-dimethylthiazol-2-yl)-5-(3 carboxymethoxyphenyl)-2-(4-sulfophenyl)-2H-tetrazolium, inner salt (MTS) for 2 hours and then measured at an absorbance of 490nm. (* p< 0.05, ** p< 0.001)

Next we studied synergistic therapeutic effects of osteoprotegerin and endostatin in breast cancer progression and bone lesions in a mouse model.

Recombinant adeno-associated virus (rAAV) containing either OPG or endostatin were generated and purified using standard protocols. Viral titers were determined by slot-blot analysis. 10^{11} viral particles of either rAAV-OPG.Fc or rAAV-endostatin or rAAV-OPG.Fc and rAAV-endostatin combined were delivered intra-muscular in the gastrocnemius muscle of right and left leg respectively in 4-6 week-old immunocompetent BALB/c female mice. Control animals were injected with rAAV expressing GFP. Highly aggressive murine mammary cancer cell line 4T1 expressing firefly luciferase (10^5cells in 100 µl saline) was injected via intra-cardiac route one week following the viral gene transfer. Breast cancer progression was monitored via bioluminescence imaging for 3 weeks. The tumor growth is measured as ratio-increase in bioluminescence counts following tumor cell implantation until the end of the experiment.

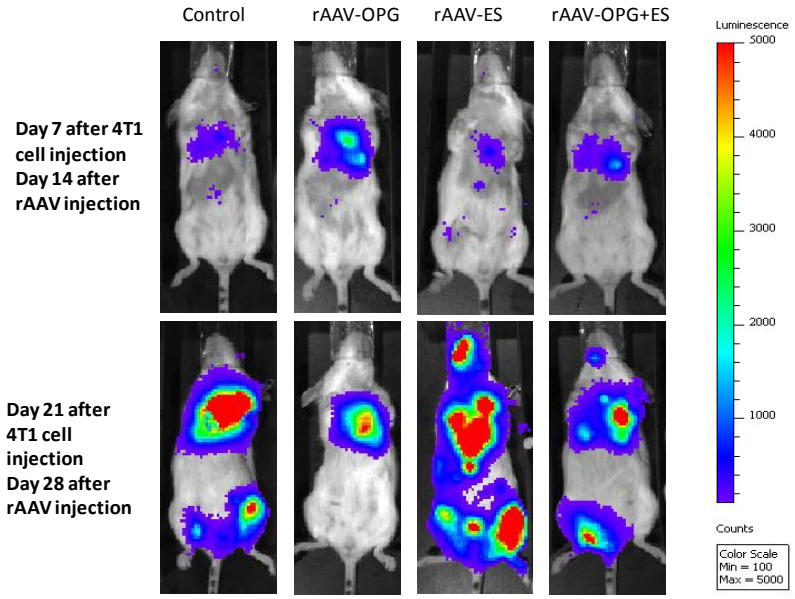

Figure 4. Growth of 4t1-Luc+ breast cancer cells in immunocompetent BALB/c mice after rAAV-OPG and rAAV-endostatin treatment.

The mice treated with only rAAV-OPG.Fc showed significant inhibition of metastatic tumor growth in the visceral organs and skeleton, whereas enhanced tumor growth was observed in mice treated with rAAV-endostatin as well as rAAV-OPG.Fc and rAAV-endostatin combined (Figures 4, 5 and 6).

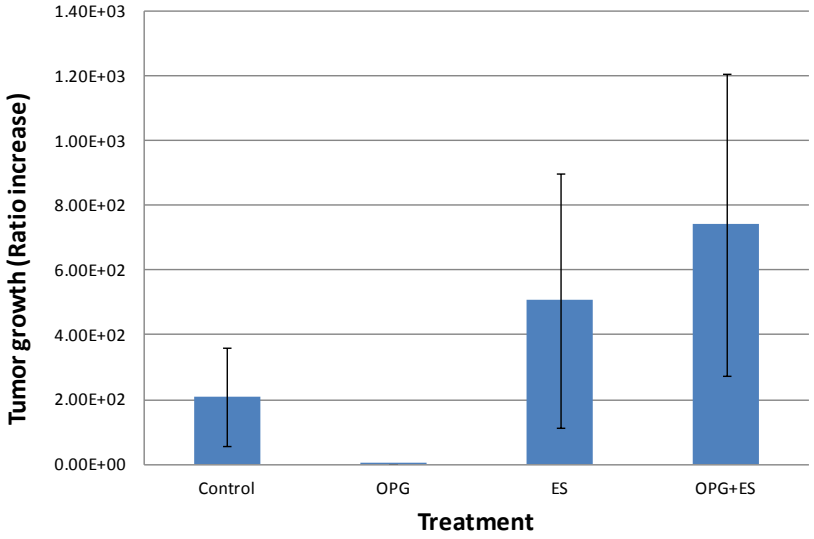

Figure 5. Tumor growth in the tibia.

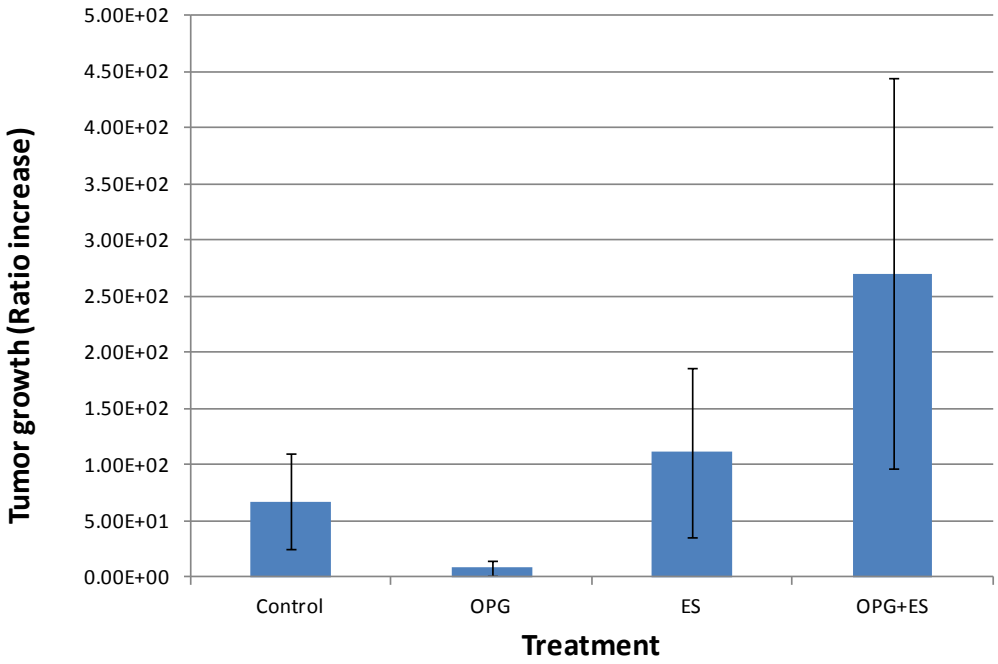

Figure 6. Overall tumor growth.

At the end of these studies, we identified domains in osteoprtegerin that bind to TRAIl and successfully abolished them to eliminate cancer cell survival, yet providing protection against cancer-induced bone loss. These studies were performed both in vitro and in vivo. Further, we tested the potential of OP, delivered using mesenchymal stem cells, engineered to overexpress OPG, in combination with an anti-angiogneic therapy. These studies were tested in a mouse model that exhibits osteolytic lesions upon tumor challenge only in limbs. Towards extrapolating the positive outcome to human situation, where breast cancer patients show osteolytic malignancy in all major bones, we developed a mouse model of osteolytic lesions in all major bones and tested the potential of modified OPG in reducing bone pathology.

Next set of experiments focused on testing the potential of OPG mutants created in our study *in vivo* by using a genetically-engineered mesenchymal stem cell (MSC) approach. First we optimized culture conditions for primary MSC and tested early passage cells for their stem cell property.
By flow cytometry analysis, positive and negative markers were enumerated on MSC (Figure 7).

Upon confirming the stem cell phenotypic markers on cultured MSC, their lineage differentiation potential was tested using adipogenic and osteogenic media. Result of this study is shown in Figure 8.

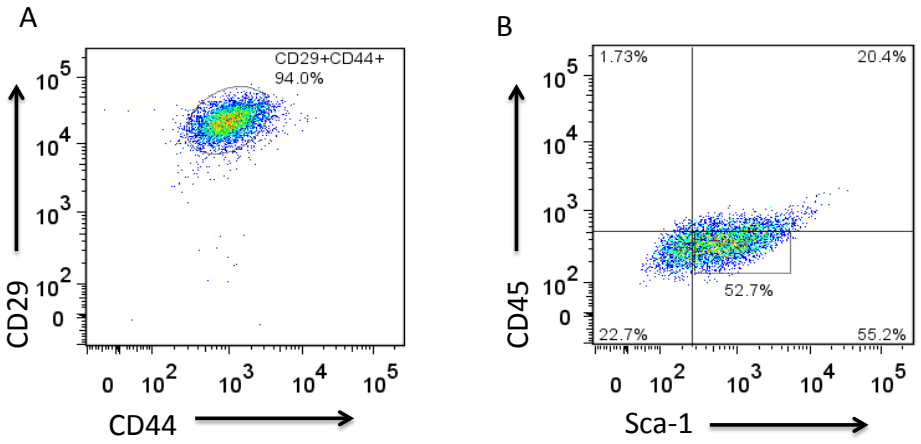

Figure 7. Characterization of MSC by flow cytometry prior to using them in *in vivo* studies. Prior to using MSC for in vivo studies, their stem cell characteristics were verified by flow cytometry. Aliquots of low-passage MSC were stained with CD29, CD44, (A), and CD45 and Sca-1 (B)antibodies and examined by FACS analysis. The stem cell nature of MSC was confirmed and phenotyped as CD29+, CD44+, CD45- and Sca-1+ cells.

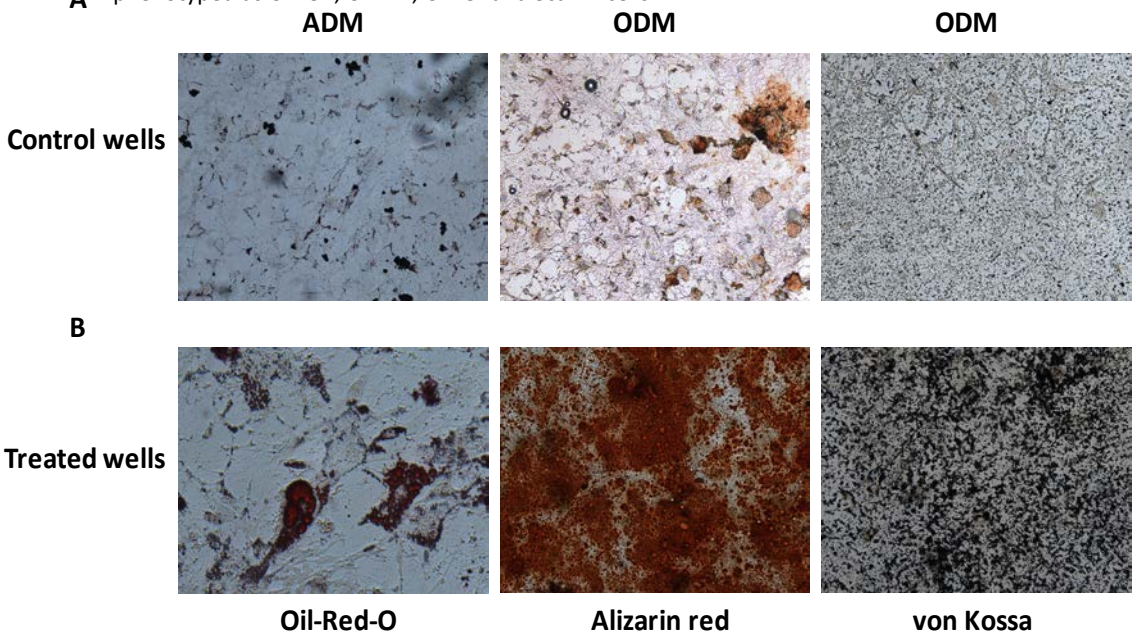

Figure 8. Characterization of MSC for stem cell potential by lineage-differentiation *in vitro.* Following phenotypic confirmation of MSC the cells were differentiated using specific media for differentiation into adipocytes (ADM) and osteoblasts (ODM). Lineage differentiation was confirmed in undifferentiated cells (A) or that grown in differentiation media (B) by oil-red staining for adipocytes and both Alizatin red and von Kossa Staining for osteoblasts.

In vivo *analysis of OPG mutants in SCID animal model with osteolytic malignancy in all major bones:* As in the first studies using MSC for in vivo expression of OPG, we used AAV-OPG-mutants to transduce hMSC to express OPG-wt or OPG-mutants (Y49R or F107A) 48 hrs before injection into

tumor challenged mice. Cohorts of SCID mice were intravenously injected with ~10^6 of the human osteolytic cancer line, CAG^{hep}, followed by non-invasive imaging. Fourteen days post tumor cell injection and upon establishment of tumor growth within the skeleton, as confirmed by non-invasive image analysis, ~10^6 hMSC that were transduced via AAV to express either OPG-wt or OPG-mutants Y49R or F107A were administered via intra-cardiac route. Mice were then monitored by non-invasive bioluminescence imaging weekly for assessment of tumor growth kinetics. Results of this study demonstrated the localization of CAG^{hep} cells to both tibia and femur as early as day-7 and by day-14 the CAG^{hep} cells could be detected in the vertebra column. Fourteen days post hMSC administration, non-invasive imaging showed an overall delay of tumor growth in mice treated with either OPG^{wt} or OPG^{mut} when compared to the naïve control group.

Osteoprotegerin mutants protect against tumor-induced osteoclastogenesis in both spine and tibia: Post hMSC-OPG therapy, bones were harvested for micro-CT analysis. Results demonstrated that mice treated with either OPG^{wt} or OPG^{mut} (Y49R or F107A) significantly protected against osteolytic bone destruction induced by CAG^{hep} cells when compared to untreated mice (CAG^{hep} cells only). Results of these studies confirmed a preliminary finding, which also demonstrated bone protection with the use of OPG^{wt} or OPG^{F107A}. It was shown for the first time that the use of OPG^{Y49R} provides protection against cancer-induced osteoclastogenesis and that overall protection is comparable to both OPG^{wt} or OPG^{F107A}. Three dimensional reconstruction of micro-CT analysis showed significant destruction to the trabecular bone under the growth plate in the tibia of mice challenged with CAG^{hep} cells. Similarly, significant bone destruction was observed in the spine, particularly the L4 bone of the lumbar region in the spinal column; as 3D reconstruction images showed complete severance of the L4 bone in some of the naïve control mice (CAG^{hep} cells only). However, images of bone 3D reconstruction for cohorts treated with OPG therapy showed intact tibia and lumbar spinal bone with bone density and trabecular connectivity comparable to age matched control groups.

OPG-mutants protect against cancer-induced osteolysis through decrease activation of osteoclasts: Harvested bones were decalcified and sectioned for IHC staining and the presence of tumor was seen in both tibia and spine when H&E stain was performed. While there was not any observable difference in bone loss within the cohorts treated with the different OPG-mutants and OPG-wt when compared to its age-matched controls, there was however, visible bone destruction both in tibia and spine in the cohorts of mice that was challenged with CAG^{hep} cells. A TRAP stain was perform to assess the osteoclast activity and as expected in the tumor challenged cohort there was an observable increase in osteoclast activity when compared to the age-matched controls. Interestingly, when comparing the hMSC-OPG treated cohorts to the age-matched controls, there was a slight increase in osteoclast activity due to the presence of tumor within the bone cavity as seen with the H&E stains, but when compared to the tumor challenged cohort, there was noticeable decrease in osteoclasts, which can account for the decrease in bone destruction observed in these treated groups. Results of these studies are provided below.

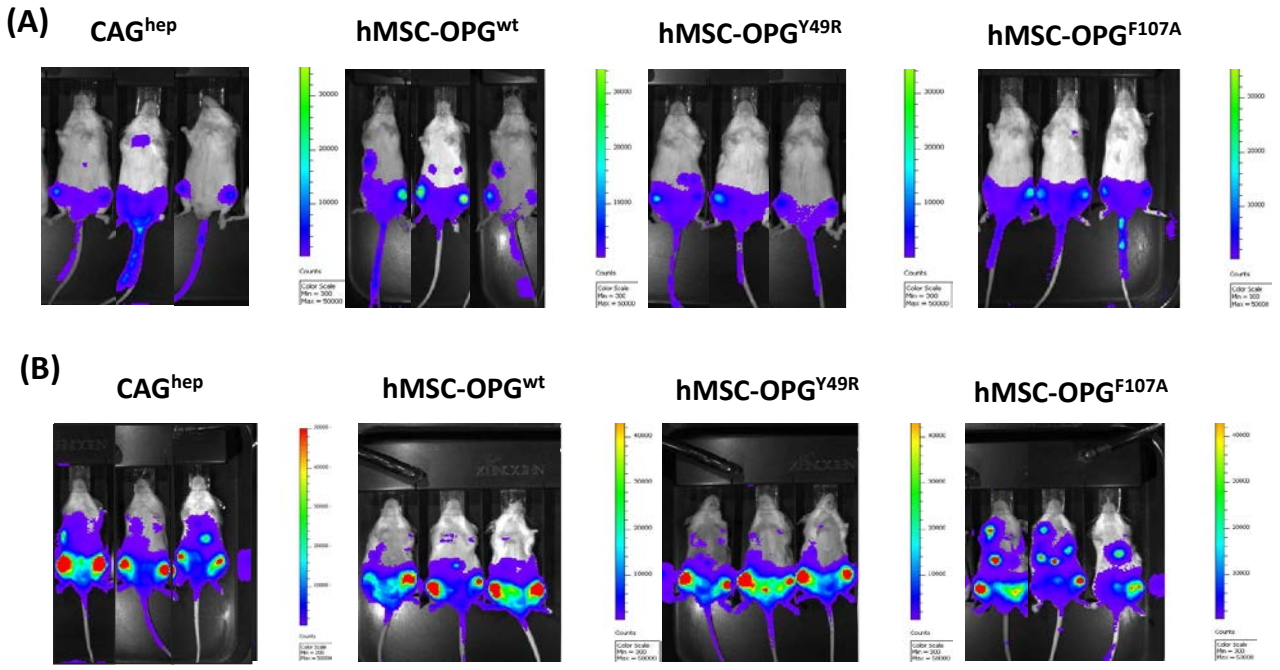

Figure 9. Monitoring of osteolytic tumor growth in both legs via noninvasive bioluminescence imaging during hMSC-OPG therapy. Cohorts of mice were challenged with ~10^6 CAG^{hep} cells via tail vein injections followed by noninvasive imaging for establishment of tumor cells within the tibia and femur. Cohorts were then administered hMSC-OPG^{wt}, hMSC-OPG^{Y49R}, or hMSC-OPG^{F107A} and continued being monitored for tumor growth in the tibia, femur and other skeletal regions on day-14, before OPG therapy (A) and day-28, 14 days after OPG therapy (B).

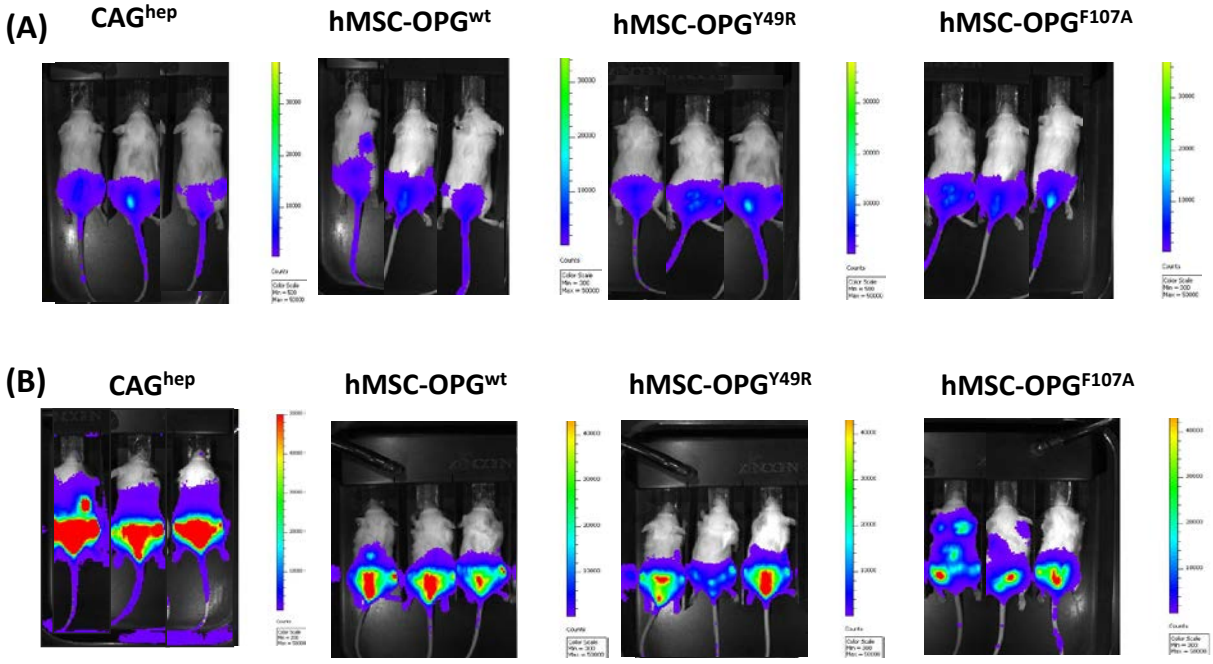

Figure 10. Monitoring of osteolytic tumor growth in spinal region via noninvasive bioluminescence imaging during hMSC-OPG therapy. Cohorts of mice were challenged with ~10^6 CAG^{hep} cells via tail vein followed by noninvasive imaging for establishment of tumor cells within the spine. Cohorts were then administered hMSC-OPG^{wt}, hMSC-OPG^{Y49R}, or hMSC-OPG^{F107A} and continued being monitored of tumor growth in the spine and other skeletal members on day-14, before OPG therapy (A) and day-28, 14 days after OPG therapy (B).

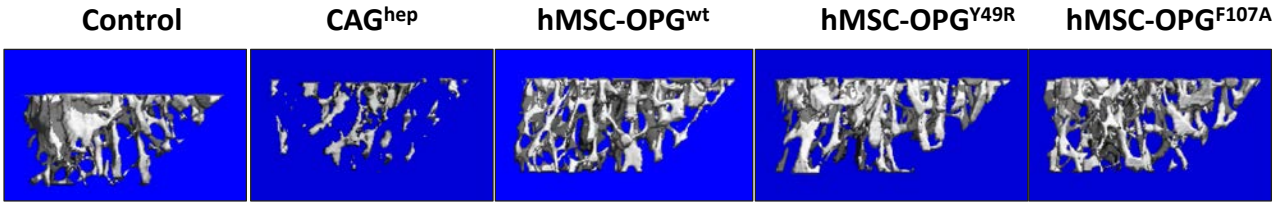

Figure 11. Evaluation of tumor-induced osteolysis by 3D reconstruction of the tibia post hMSC-OPG therapy. At the end of OPG therapy, bones were harvested from cohorts of mice for micro-CT analysis. Results of 3D reconstruction images demonstrated significant tibia destruction in cohorts of mice challenged with CAG^{hep} cells with overall bone protection observed in cohorts treated with hMSC-OPG^{wt}, hMSC-OPG^{Y49R}, or hMSC-OPG^{F107A} .

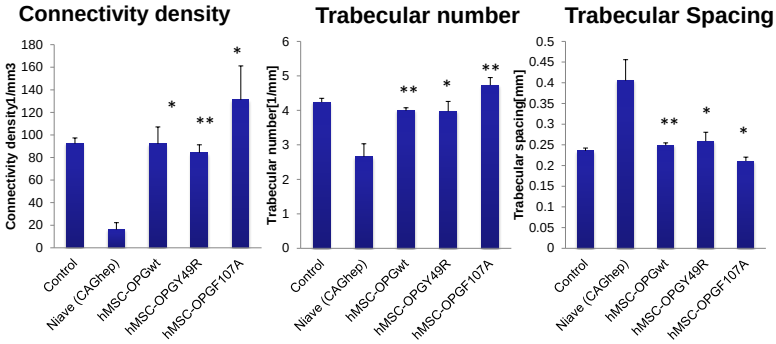

Figure 12. Micro-computed tomography analysis of tibia post hMSC-OPG therapy. Quantitative analysis revealed statistically significant differences in connectivity density, trabecular number, and trabecular spacing when comparing naïve treated group (CAG^{hep} cells only) to hMSC-OPG treated groups (B). (p* < 0.05, p** < 0.01)

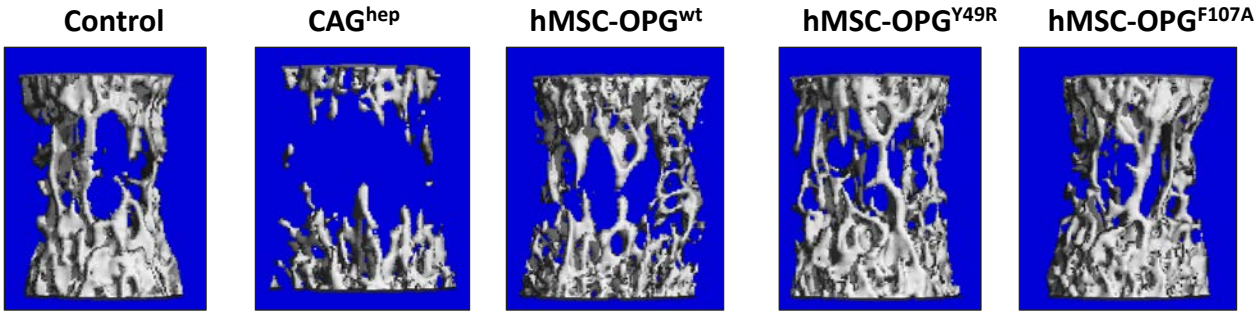

Figure 13. Evaluation for cancer-induced osteolysis by 3D reconstruction of the spine post hMSC-OPG therapy. At the end of OPG therapy, bone tissues were harvested from cohorts of mice for micro-CT analysis. Results of 3D reconstruction images demonstrated significant spinal destruction in cohorts of mice challenged with CAG^{hep} cells with overall bone protection observed in cohorts treated with hMSC-OPG^{wt}, hMSC-OPG^{Y49R}, or hMSC-OPG^{F107A}.

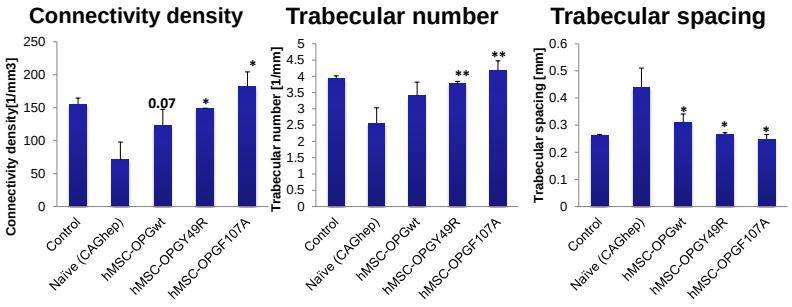

Figure 14. Micro-computed tomography analysis of L4 spinal bone post hMSC-OPG therapy. Quantitative analysis also revealed statistically significant differences in connectivity density, trabecular number, and trabecular spacing when comparing naïve treated group (CAG^{hep} cells only) to hMSC-OPG treated groups. (p* < 0.05, p** < 0.01)

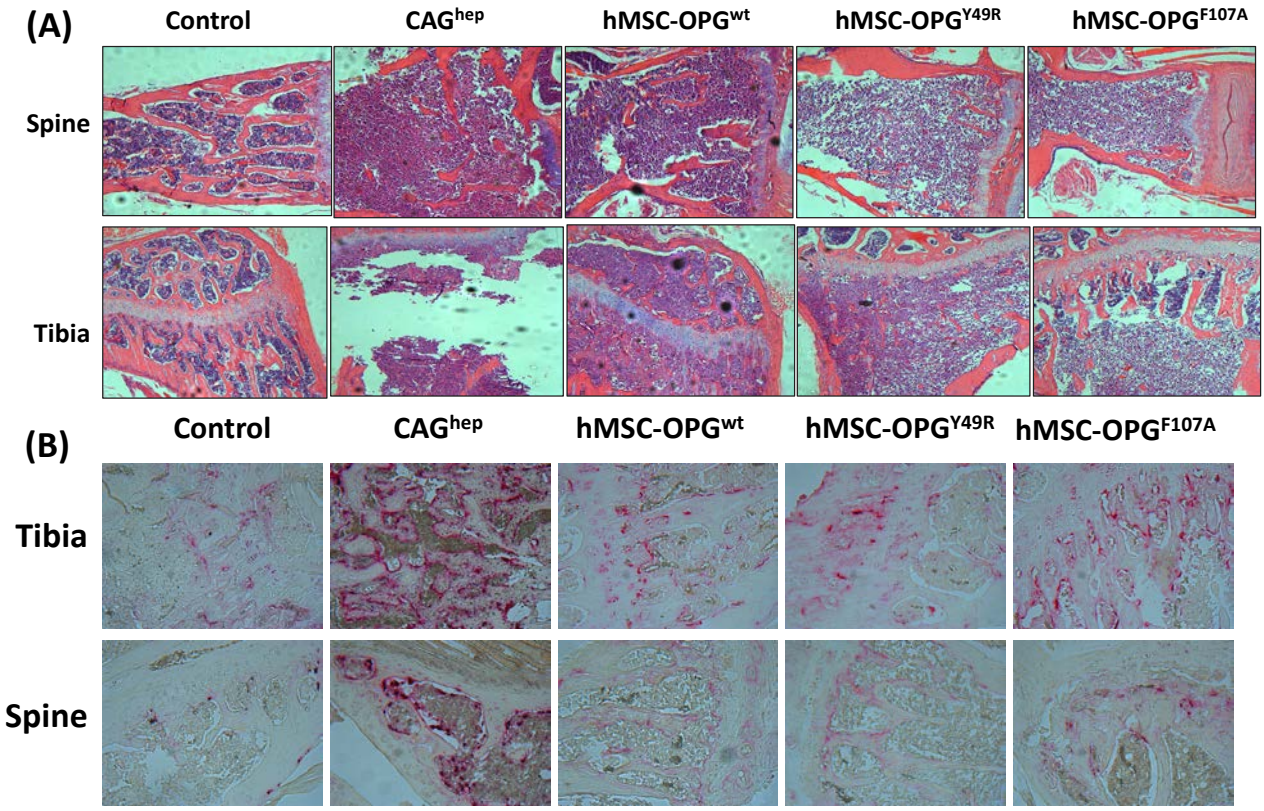

Figure 15. Immunohistochemistry staining of tibia and spine post hMSC-OPG therapy. Bone tissues were harvested post hMSC-OPG therapy, decalcified, and stained for assessment of the therapy. Hematoxalin and Eosin stain was performed for observation of tumor growth within the bone cavity of both tibia and spine (A). To assess overall osteoclast activity within the bone microenvironment, TRAP stain was performed on the both tibia and spine (B).

IMPACT

Data from these studies revealed that:

- Recombinant and wild-type OPG bound TRAIL and inhibited its cytotoxic effects as proliferation of cancer cells still occurred despite the cells being cultured in the presence of TRAIL.
- However, mutant Y61E also bound TRAIL, and exhibited protection of cancer cells from the toxic effects of TRAIL. Mutants Y49A and Y49R showed significant abolished TRAIL binding as a decrease in cell proliferation and increased cell apoptosis was observed in the assays performed.
- Data also suggested that mutants F96R and Y107A may have a greater lack of TRAIL binding property (data not shown).
- Mutants Y49R, F96R and Y107A are ideal for *in vivo* analysis.
- rAAV-OPG.Fc treatment was highly effective in inhibiting metastatic progression of 4T1 mammary carcinoma cells in this mouse model.
- On the contrary, rAAV-endostatin promoted metastatic progression of 4T1 cells when given either alone or in combination with rAAV-OPG.Fc and warrants further investigation.
- rAAV-OPG.Fc treatment was highly effective in inhibiting metastatic progression of osteolytic carcinoma cells, disseminated to various skeletal regions, similar to the human patients.

Conclusions

- Constructed and validated key OPG variants lacking TRAIL binding but retaining OPG binding.
- Developed of a mouse model with osteolytic bone dissemination of tumor in all major regions of the skeleton
- Tested the potential of OPG mutant therapy using MSC
- Observed a significant decrease in osteolytic burden following therapy with OPG mutant in both limbs and spine. rAAV-OPG.Fc treatment was highly effective in inhibiting metastatic progression of 4T1 mammary carcinoma cells in this mouse model.
- On the contrary, rAAV-endostatin promoted metastatic progression of 4T1 cells when given either alone or in combination with rAAV-OPG.Fc and warrants further investigation.

PRODUCTS

Peer-reviewed manuscripts published:

1. Sawant A, Chanda D, Hensel JA, Harris, BA, Siegal GP, Maheshwari A, and Ponnazhagan S. Depletion of plasmacytoid dendritic cells inhibits tumor growth and prevents bone metastasis of the breast cancer cells. J. Immunol. 2012, 189(9):4258-65.

2. Sawant A, Deshane J, Lee C, Harris B, Jules J, Feng X, and Ponnazhagan, S. Myeloid-derived suppressor cells function as osteoclast progenitors enhancing bone destruction in breast cancer. Cancer Research 2013, 73:672-82.

3. Sawant A, Ponnazhagan, S. Myeloid-derived suppressor cells as a novel target for the control of osteolytic bone disease. Oncoimmunol. 2013, 2:e24064.

4. Sawant A, Ponnazhagan, S. Myeloid-derived suppressor cells as osteoclast progenitors: a novel target for controlling osteolytic bone metastasis. Cancer Res. 2013, 73: 4606-4610.

5. Lee JH, Isayeva T, Larson MR, Sawant A, Cha HR, Chanda D, Chesnokov IN, Ponnazhagan S. Endostatin: A novel inhibitor of androgen receptor function in prostate cancer. Proc Natl Acad Sci U S A. 2015 Feb 3;112(5):1392-7.

6. Higgs JT, Jarboe, J, Lee JH, Deivanayagam C, Ponnazhagan S. Structural variants of osteoprotegerin lacking TRAIL binding for therapeutic bone remodeling in osteolytic malignancies. Molecular Cancer Res. 2015 May;13(5):819-27.

PARTICIPATION AND OTHER COLLABORATING ORGANIZATIONS

UAB Personnel who received financial support from this grant

Selvarangan Ponnazhagan, Ph.D.
Anandi Sawant, Ph.D.
George Tsuladze, M.D.

Other collaborating organiztions

None

APPENDICES

References cited:

1. Khosla S. Minireview: the OPG/RANKL/RANK system. Endocrinology 2001;142(12):5050-5.
2. Huang L, Cheng YY, Chow LT, Zheng MH, Kumta SM. Tumour cells produce receptor activator of NF-kappaB ligand (RANKL) in skeletal metastases. Journal of clinical pathology 2002;55(11):877-8.
3. Simonet WS, Lacey DL, Dunstan CR*, et al.* Osteoprotegerin: a novel secreted protein involved in the regulation of bone density. Cell 1997;89(2):309-19.
4. Emery JG, McDonnell P, Burke MB*, et al.* Osteoprotegerin is a receptor for the cytotoxic ligand TRAIL. The Journal of biological chemistry 1998;273(23):14363-7.
5. Cha SS, Sung BJ, Kim YA*, et al.* Crystal structure of TRAIL-DR5 complex identifies a critical role of the unique frame insertion in conferring recognition specificity. The Journal of biological chemistry 2000;275(40):31171-7.

Published manuscripts acknowledging the financial support provided by DoD are appended in the following pages

The Journal of Immunology

Depletion of Plasmacytoid Dendritic Cells Inhibits Tumor Growth and Prevents Bone Metastasis of Breast Cancer Cells

Anandi Sawant, Jonathan A. Hensel, Diptiman Chanda, Brittney A. Harris, Gene P. Siegal, Akhil Maheshwari and Selvarangan Ponnazhagan

J Immunol 2012; 189:4258-4265; Prepublished online 26 September 2012;
doi: 10.4049/jimmunol.1101855
http://www.jimmunol.org/content/189/9/4258

The Journal of Immunology is published twice each month by
The American Association of Immunologists, Inc.,
9650 Rockville Pike, Bethesda, MD 20814-3994.

Print ISSN: 0022-1767 Online ISSN: 1550-6606.

Depletion of Plasmacytoid Dendritic Cells Inhibits Tumor Growth and Prevents Bone Metastasis of Breast Cancer Cells

Anandi Sawant,* Jonathan A. Hensel,*,[1] Diptiman Chanda,* Brittney A. Harris,* Gene P. Siegal,* Akhil Maheshwari,[†,2] and Selvarangan Ponnazhagan*

Elevated levels of plasmacytoid dendritic cells (pDC) have been reported in breast cancer patients, but the significance remains undefined. Using three immunocompetent mouse models of breast cancer bone metastasis, we identified a key role for pDC in facilitating tumor growth through immunosuppression and aggressive osteolysis. Following infiltration of macrophages upon breast cancer dissemination, there was a steady increase in pDC within the bone, which resulted in a sustained Th2 response along with elevated levels of regulatory T cells and myeloid-derived suppressor cells. Subsequently, pDC and $CD4^+$ T cells, producing osteolytic cytokines, increased with tumor burden, causing severe bone damage. Microcomputed tomography and histology analyses of bone showed destruction of femur and tibia. The therapeutic significance of this finding was confirmed by depletion of pDC, which resulted in decreased tumor burden and bone loss by activating tumor-specific cytolytic $CD8^+$ T cells and decreasing suppressor cell populations. Thus, pDC depletion may offer a novel adjuvant strategy to therapeutically influence breast cancer bone metastasis. ***The Journal of Immunology*****, 2012, 189: 4258–4265.**

Nearly 80–90% of breast cancer patients with advanced disease have osteolytic disease, characterized by increased bone damage resulting from enhanced osteoclast activity (1). The presence of such bone lesions usually signifies serious morbidity and a grave prognosis, with severe pain, pathological fractures, nerve compression syndromes, and hypercalcemia (2). Current therapies for bone metastasis in breast cancer patients are limited and are focused only on symptomatic management, limiting the progression of established disease (3). Although a significant amount of research has been carried out on understanding breast cancer bone metastasis, not much is known about the events leading to the bone metastasis. Hence, a better understanding of the molecular mechanisms involved in the formation and progression of bone metastases is needed.

Dissemination of the primary tumor to the bone triggers the production of osteolytic cytokines and growth factors that result in osteoclast activation and the promotion of tumor growth and immune suppression in the bone microenvironment (4). Conversely, products of bone cells are critical for normal development of the hematopoietic and immune systems (4). In osteopenic conditions, such as osteoporosis, bone destruction results from enhanced osteoclast activity with a concomitant decrease in osteoblast numbers, without a significant alteration in the immune system (5). But the osteolytic bone changes observed in bone metastasis are triggered by a coordinated interplay of bone-homing cancer cells, osteoclasts, and the immune cells in the bone marrow (BM) (6). Thus, elucidation of the molecular mechanisms during these interactions should provide new insights into the treatment for cancer bone metastasis.

Using immunocompetent mouse models of breast cancer dissemination to bone and other organs, the current study characterized the immune mechanisms that regulate osteolytic breast cancer metastasis at different stages of tumor progression. Results indicated that the vicious cascade promoting tumor growth, immune suppression, and bone damage is regulated by plasmacytoid dendritic cells (pDC), shifting the Th cell homeostasis greatly toward the Th2 phenotype, independent of the effects of myeloid suppressor cells. Depletion of pDC in vivo resulted in a significant increase in the Th1 response, leading to a decrease in both tumor growth and bone damage. Further, reversal of the Th2 to Th1 response resulted in increased $CD8^+$ T cell activity against the tumor in bone and visceral organs. Collectively, these data indicate the potential of this strategy to decrease bone morbidity and increase survival in advanced-stage breast cancer patients.

Materials and Methods

An in vivo model for breast cancer bone metastasis

Mouse breast cancer cell lines 4T1, constitutively expressing firefly luciferase [4T1(fLuc)], TM40D, and r3T were kind gifts from Dr. Xiaoyuan Chen (Stanford University, Stanford, CA), Dr. Andre Lieber (University of Washington, Seattle, WA), and Dr. Susan Rittling (Forsyth Institute, Cambridge, MA), respectively, and were cultured as described previously (7–9). Approximately 10^5 cells from each cell line were injected via the intracardiac route in syngeneic, female mice at 6–8 wk of age (Frederick Cancer Research and Development Center, Frederick, MD). Progression of 4T1 tumor growth and dissemination to the bone were followed by noninvasive imaging of mice using the IVIS Imaging System (Xenogen). On days 3, 7, 10, and 14, cohorts of mice were sacrificed for analyses. Blood was collected, and serum was separated. Selected visceral organs and bones were collected for histology. Spleen and BM were used for enumerating the

*Department of Pathology, University of Alabama at Birmingham, Birmingham, AL 35294; and [†]Department of Pediatrics, University of Alabama at Birmingham, Birmingham, AL 35294

[1]Current address: Department of Surgery/Urology, University of Colorado, Denver, Denver, CO.

[2]Current address: Department of Pediatrics, University of Illinois, Chicago, IL.

Received for publication June 24, 2011. Accepted for publication August 26, 2012.

This work was supported in part by National Institutes of Health Grants R01AR050251, 1R01AR058344-01, R01CA133737, and P30 AR046031-10 and by U.S. Army Department of Defense Grants BC044440 and BC101411.

Address correspondence and reprint requests to Prof. Selvarangan Ponnazhagan, Department of Pathology, University of Alabama at Birmingham, 1825 University Boulevard, Shelby 814, Birmingham, AL 35294. E-mail address: pons@uab.edu

The online version of this article contains supplemental material.

Abbreviations used in this article: BM, bone marrow; MDSC, myeloid-derived suppressor cell; micro-CT, microcomputed tomography; OPG, osteoprotegerin; pDC, plasmacytoid dendritic cell; TRAP, tartrate-resistant acid phosphatase; Treg, regulatory T cell; UAB, University of Alabama at Birmingham; WT, wild-type.

www.jimmunol.org/cgi/doi/10.4049/jimmunol.1101855

immune cell profile and activation status. Tumor progression was also assessed in an IFN-αR knockout mouse model ($IFNAR^{-/-}$) on a BALB/c background (kindly provided by Dr. Andrew Mellor, Georgia Health Sciences University, Augusta, GA) and on a C57BL/6 background using a syngeneic osteolytic cell line.

Immune cell depletion

To deplete pDC mice were injected i.p. with 250 μg PDCA-1 Ab (clone # JF05-IC2.41; Miltenyi Biotec, Auburn, CA) every other day (10). As a control, mice were injected with similar amounts of IgG Ab (Miltenyi Biotec). Four days after injection of Abs, blood was collected by retinal bleeding. Mononuclear cells, obtained by Ficoll-Hypaque (GE Healthcare, Piscataway, NJ) gradient extraction, were incubated with PDCA-1–Alexa Fluor 647 Ab (eBioscience, San Diego, CA) for 30 min and enumerated by flow cytometry. Once depletion of pDC was confirmed, mice were challenged with 10^5 4T1(fLuc) cells by the intracardiac route. Injection of PDCA-1 or IgG Abs was continued until the end of the experiment.

Microcomputed tomography and histology

Upon sacrifice of tumor-challenged mice at different time points, both femur and tibia were collected and fixed in 4% buffered formalin for 2 d and subjected to microcomputed tomography (micro-CT) analysis (Micro-CT40; SCANCO Medical, Wayne, PA). The formalin-fixed bones were decalcified in 2.5% EDTA (pH 8) for 2 wk. Five-micrometer paraffin-embedded sections were used for histological analysis.

Immunohistochemistry

The presence of breast cancer cells in the visceral tissues and bone was detected by conventional light microscopic evaluation of H&E-stained tissue sections by a senior anatomic pathologist and confirmed by staining with cytokeratin-8 Ab (Abcam, Cambridge, MA), as described previously (11). The presence of osteoclasts within the bone sections was detected by tartrate-resistant acid phosphatase (TRAP) staining, as described previously (12). All of the microscopic images were obtained using a Leica DMI4000B microscope, attached to a Leica DFC500 digital camera. LASv3.6.0 software was used to optimize picture quality and to generate scale bars for individual images.

Isolation of immune cells and FACS analysis

Immune cells were isolated from the bone of tumor-challenged mice. Both femur and tibia were flushed to collect BM cells. Following RBC lysis using ACK lysis buffer (Quality Biologicals, Gaithersburg, MD), cells were suspended in FACS-staining buffer (PBS + 2% FBS + 0.01% sodium azide) and incubated with Fc Block for 15 min at 4˚C. These cells were stained (10^6 cells/group) to detect various immune cell populations using cell-specific fluorescence-conjugated Abs, purchased from eBioscience, for 30 min at 4˚C. Upon fixation with 4% paraformaldehyde, cells were enumerated using a FACSCalibur Flow Cytometer (Beckman Coulter, Hialeah, FL) (13). A total of 30×10^3 events was acquired for each sample. The data were analyzed using FlowJo software. To detect the presence of regulatory T cells (Tregs), cells stained with Abs to CD3 (clone 17A2), CD4 (clone GK1.5), and CD25 (clone PC61.5) were permeabilized with a commercially available permeabilization buffer (eBioscience) for 30 min at 4˚C and then stained with Ab to Foxp3 for 30 min at 4˚C. A subset of $CD25^+Foxp3^+$ cells was detected within the $CD3^+CD4^+$ cells; these cells were considered Tregs.

To detect the presence of PDCA-1 Ag on the 4T1(fLuc) cells, BM cells were collected upon sacrifice of mice with established breast cancer bone metastasis. Following the addition of Fc Block, cells were stained with Abs to CD45 (clone 30-F11) and PDCA-1 (clone eBio927) for 30 min at 4˚C. Cells that stained negative for both of the Abs were sorted, and cell lysate was prepared. Luciferase assay was carried out per the manufacturer's instructions (Promega). As a control, 4T1(fLuc) cells grown in vitro were used for the luciferase assay.

Coculture assay for osteoclast activity

For isolation of monocytes, cells were incubated with biotinylated CD115 Ab (eBioscience) for 15 min at 4˚C, followed by incubation with anti-biotin microbeads (Miltenyi Biotec). Magnetic separation was carried out per the manufacturer's instructions. A commercially available kit was used for isolation of $CD4^+$ T cells (Miltenyi Biotec). Monocytes and $CD4^+$ T cells were cultured at a ratio of 1:100; monocytes were plated in 96-well tissue culture plates (Corning, Corning, NY), and $CD4^+$ T cells were placed in 0.2-μm tissue culture inserts (Nalge Nunc International, Rochester, NY). Media were changed as described previously (14). To determine the role of RANKL and IL-15 in osteoclast generation, recombinant osteoprotegerin (OPG; 100 ng/ml) or IL-15 Ab (10 μg/ml) was added to the coculture either individually or in combination. After 10 d, the presence of osteoclasts was detected by TRAP staining.

Cytokine assay

RNA was isolated from $CD4^+$ T cells by the TRIzol RNA-extraction method (Invitrogen, Carlsbad, CA). cDNA was prepared per the manufacturer's instructions (Bio-Rad, Hercules, CA) and was used in real-time RT-PCR assays for detecting the presence of the cytokines IL-3, IL-6, IL-10, IL-11, IL-12, IL-15, IL-17, TGF-β, and RANKL.

Serum cytokine levels were assayed using a commercially available Mouse 22-plex cytokine assay kit obtained from Millipore (Millipore, Billerica, MA). Each assay was performed in triplicate.

Cytotoxicity assay

$CD8^+$ T cells were isolated from the BM using a commercially available $CD8a^+$ T cell isolation kit II (Miltenyi Biotec) and were used as the effector cells. 4T1(fLuc) cells were used as the target population. The assay was set up with E:T ratios of 5:1, 10:1, 20:1, and 40:1. The cytotoxicity assay was performed using the commercially available LIVE/DEAD cell-mediated cytotoxicity kit (Molecular Probes, Eugene, OR).

Statistical analysis

Data are presented as mean ± SE. Statistical analysis was performed using the Student t test. Statistical significance was determined at $p < 0.05$.

Results

An in vivo model of breast cancer bone dissemination

For understanding possible mechanisms that are conducive for the growth of breast cancer in the bone, we used three models with syngeneic breast cancer cell lines: 4T1(fLuc) cells in BALB/c, r3T cells in 129S, and TM40D cells in BALB/c mice. Upon intracardiac injection, these cells readily metastasized to various organs, including the bone (Fig. 1A). Histologic analysis verified the presence of cancer cells in the liver and lungs (Fig. 1B), as well as in the tibia and femur (Fig. 1C). Micro-CT analysis of the tibia and femur, 14 d after tumor challenge, showed a dramatic destruction of bone compared with age-matched controls (Fig. 1D, Supplemental Fig. 1), with increased osteoclast numbers (Fig. 1E).

Dissemination of cancer cells to the bone initiates an inflammatory reaction followed by pDC enrichment

As tumor cells disseminated to the bone, cohorts of mice were sacrificed, and cells were collected from the BM to examine the profile of immune cells mediating the disease pathology. Results indicated that as breast cancer disseminated to the bone, there was an initial macrophage infiltration (Fig. 2A), followed by an increase in the $B220^+CD11c^+$ (clone RA3-6B2 for B220 and clone N418 for CD11c Ab) pDC population (Fig. 2B). To further confirm the presence of pDC, $B220^+CD11c^+$ cells were stained for markers, including Singlec-H (clone eBio440c), PDCA-1, and Gr-1. Close to or >90% of the $B220^+CD11c^+$ cells were positive for these markers, confirming the pDC increase in the bone (Fig. 2C).

Increased pDC numbers with increased bone metastasis were observed in all three models, confirming that elevated pDC numbers during progressive stages of breast cancer dissemination are not due to the variability in the genetic background of the mice used. (Fig. 2D, 2E).

Elevation of pDC numbers is accompanied by skewing of immune response toward Th2

Next, the effect of elevated pDC levels on the T cell immune response was analyzed by characterizing the Th response in BALB/c mice with 4T1(fLuc) cells. The results of this study revealed significantly high levels of IL-4 compared with IFN-γ levels that progressed with tumor growth and bone metastasis, thus indicating

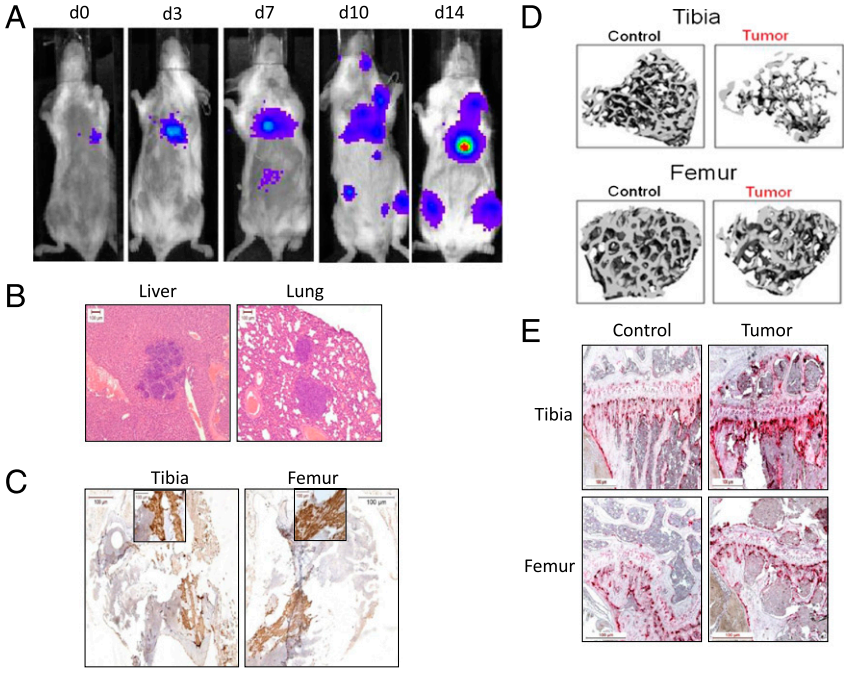

FIGURE 1. In vivo model for bone metastasis of breast cancer. (**A**) The murine breast cancer cell line 4T1(fLuc) was injected into female BALB/c mice via the intracardiac route. Growth and spread of the tumor was followed on days 3, 7, 10, and 14 by noninvasive luciferase imaging. A representative image for each time point is shown. (**B**) Mice were sacrificed, liver and lungs were collected, and paraffin sections were stained with H&E to detect the presence of tumor cells. Representative images from mice sacrificed 14 d posttumor challenge. (**C**) Cytokeratin-8 staining was performed on paraffin sections of the femur and tibia from mice 14 d after tumor challenge (*insets,* original magnification ×40). (**D**) Fourteen days posttumor challenge, tibia and femur were collected and subjected to micro-CT analysis. Tibia and femur from age-matched mice were included as a control. (**E**) Paraffin sections from 14 d posttumor-challenged mice were stained with TRAP to detect osteoclasts. Six mice were used for each time point, and the experiment was performed three times independently. Scale bars, 100 μm.

a skewing toward Th2 response as the cancer progressed to invade and proliferate within the bone (Fig. 3A). The multiplex cytokine analysis from the sera of mice revealed an increased secretion of Th2-specific cytokines (IL-5 and IL-6) and reduced levels of Th1-specific cytokines (IL-12 and IP-10) (data not shown). The switch to a Th2 response also correlated with increased pDC levels.

Because pDC skew the immune response toward a Th2 phenotype via a CD40–CD40L interaction in the presence of IL-3 (15), we examined the surface expression of CD40 (clone 1C10) on pDC and CD40L (clone PC61.5) on $CD4^+$ T cells. The skewing of the immune response toward the Th2 phenotype correlated with increased expression of CD40 and CD40L on pDC and $CD4^+$ T cells, respectively (Fig. 3B). IL-3 levels were elevated in $CD4^+$ T cells (Fig. 3C). Together, these data show that elevated pDC in the bone microenvironment polarizes the immune response toward a suppressive Th2 phenotype that allows tumor growth and spread into bone.

Increased production of osteolytic cytokines leads to increased osteoclast numbers and bone destruction

Cytokine analysis by the multiplex assay using sera from mice indicated a significant increase in the levels of IL-15, RANTES, and MCP-1, known inducers of osteoclasts, as cancer dissemination progressed into and within the bone (Supplemental Fig. 1). Because $CD4^+$ T cells are a major source of osteolytic cytokines, we assayed for the presence of these cytokines in $CD4^+$ T cells from the BM of tumor-challenged mice. Our data indicated significantly higher levels of IL-6, IL-11, and IL-15 with increased bone destruction (Fig. 4A). We next determined whether the increased cytokine production by $CD4^+$ T cells resulted in increased osteoclast numbers. To assay for osteoclast numbers, $CD4^+$ T cells, isolated from either spleen or BM, were cocultured with BM-derived monocytes. The results indicated significantly high numbers of osteoclasts by TRAP staining when monocytes were cocultured with BM-derived $CD4^+$ T cells compared with those from spleen (Fig. 4B). Further, the number of osteoclasts increased as breast cancer metastasized within the bone.

We next determined whether the $CD4^+$ T cells in the BM of tumor-bearing mice are more primed to effect monocyte differentiation into osteoclasts. For this purpose, monocytes from control mice were cocultured with $CD4^+$ T cells from tumor-challenged mice, and monocytes from the tumor-challenged mice were cocultured with $CD4^+$ T cells from control mice. The results indicated a significant increase in osteoclast numbers when $CD4^+$ T cells from tumor-bearing mice were cocultured with monocytes from tumor-challenged mice or from control mice (Fig. 4C). Conversely, $CD4^+$ T cells from control mice induced fewer osteoclasts when cultured with tumor-derived monocytes. However, osteoclast numbers were still significantly greater than that obtained after culturing monocytes and $CD4^+$ T cells from control mice, suggesting that monocytes from tumor-challenged mice are more primed toward osteoclast differentiation.

Further, to determine which osteolytic cytokines played a major role in osteoclast activation, OPG, a soluble decoy receptor of RANKL, and Ab to IL-15 were added to the culture either individually or in combination. The results of this study indicated that the number of osteoclasts was considerably reduced when OPG and IL-15 Abs were added individually or in combination (Fig. 4D), confirming that both RANKL and IL-15 induce monocyte differentiation toward osteoclasts.

Depletion of pDC in vivo results in reduced tumor growth and absence of bone metastasis

To confirm that pDC are key regulators of breast cancer bone metastasis, pDC depletion was performed in vivo with PDCA-1 Ab (Supplemental Fig. 2). As a control, cohorts of mice received isotype IgG Ab. On day 12 posttumor challenge, tumor growth was observed in the bones of both naive (challenged with 4T1 cells but without any Ab treatment) and IgG-injected mice. However, PDCA-1–injected mice showed a dramatic reduction in overall tumor burden (Fig. 5A, 5B), and the tumor cells did not disseminate to bone (Fig. 5A). Metastasis to lungs was significantly less compared with naive and IgG-injected groups (Fig. 5C, 5D). Cytokeratin-8 staining did not reveal the occult presence of cancer cells in the tibia of PDCA-1–injected mice, further supporting the luciferase image analysis (Fig. 5E).

To rule out the possibility that reduced tumor burden in PDCA-1–injected mice was not due to binding of the PDCA-1 Ab to 4T1

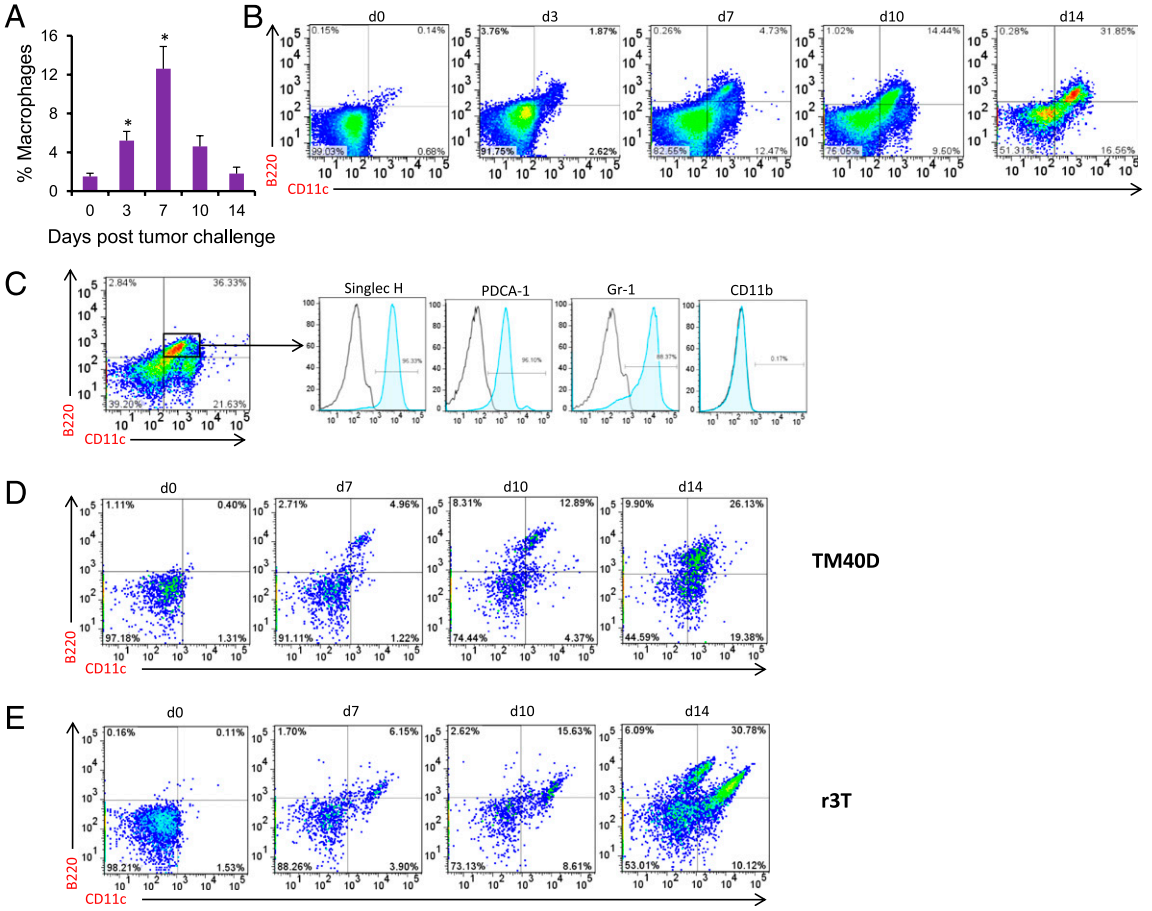

FIGURE 2. Numbers of pDC increase with increased dissemination of breast cancer to bone. (**A**) On days 3, 7, 10, and 14 following tumor cell injection, mice were sacrificed, and BM cells were isolated as described in *Materials and Methods*. The presence of macrophages was detected using anti-F4/80 and enumerated by flow cytometry. *$p < 0.05$, Student t test. (**B**) pDC were detected by staining with B220 and CD11c Abs and analyzed by flow cytometry. A representative data set from each time point is shown. (**C**) The presence of pDC ($B220^+CD11c^+$) was further confirmed with Singlec-H, PDCA-1, Gr-1, and CD11b Abs. Data are shown for mice 14 d posttumor challenge. (**D** and **E**) BALB/c and 129S mice were injected with TM40D and r3T cells, respectively, via the intracardiac route. pDC levels in BM were evaluated by flow cytometry using B220 and CD11c Abs on days 7, 10, and 14, as described in *Materials and Methods*. Representative data from each time point are shown. BM cells were isolated from six mice for every time point and were treated as individual samples. For each sample, the above-mentioned flow cytometry analysis was performed. This experiment was performed three times independently.

(fLuc) cells, which could have prevented their proliferation, 4T1 (fLuc) cells isolated from tumor-bearing mice were tested for their ability to bind to PDCA-1 Ab. Once breast cancer bone metastasis was established in mice, the animals were sacrificed, and BM cells were collected. Cells were stained for Abs to CD45 and PDCA-1. Because nonimmune cells do not express CD45, staining for PDCA-1 was detected among $CD45^-$ cells. The results clearly indicated an absence of PDCA-1 staining on $CD45^-$ cells. Further, to confirm that the $CD45^-$ cells that did not bind to PDCA-1 were indeed 4T1(fLuc) cells, these cells were sorted, and luciferase activity was determined in that population because the 4T1(fLuc) cells used in this study constitutively expressed firefly luciferase. A high luciferase count was detected, suggesting that a major fraction of $CD45^-PDCA\text{-}1^-$ cells were indeed breast cancer cells (Supplemental Fig. 2). This observation confirmed that in vivo breast cancer cells isolated from the bone microenvironment do not express PDCA-1, thus eliminating any direct effect of PDCA-1 Ab treatment on tumor growth and dissemination and validating its use for this study.

For further direct confirmation that pDC indeed play a vital role in breast cancer bone metastasis, a genetic mouse model lacking expression of IFN-αR ($IFNAR^{-/-}$) was used because these mice lack functional pDC (16, 17). A similar study in this model showed a dramatic reduction in the growth of breast cancer in $IFNAR^{-/-}$ mice compared with the syngeneic wild-type (WT) mice, thus confirming a role for pDC in promoting tumor growth and metastasis (Fig. 5F).

Micro-CT analysis of femur and tibia following PDCA-1 injection did not show the bone destruction seen in the naive and IgG-injected mice (Fig. 6A), which also correlated with fewer $TRAP^+$ osteoclasts in tibia (Fig. 6B). These results were further confirmed when, upon coculture of $CD4^+$ T cells and monocytes, the PDCA-1 group had significantly fewer osteoclasts compared with the naive and IgG groups (Fig. 6C). The decreased osteoclast numbers can be attributed to decreased amounts of osteoclast-inducing cytokines in mice treated with PDCA-1 Ab (Fig. 6D, Supplemental Fig. 3). Similar to the results observed in the PDCA-1 group, micro-CT analysis also revealed reduced bone destruction in tumor-challenged $IFNAR^{-/-}$ mice compared with the WT mice (Fig. 6E). Together, these data demonstrate that pDC enhance breast cancer bone metastasis.

Additionally, to rule out the possibility that the genetic background of $IFNAR^{-/-}$ mice (BALB/c) played a role in reduced tumor growth and osteolysis, a similar study was carried out in $IFNAR^{-/-}$ mice on a C57BL/6 background using an osteolytic cell line. The data clearly demonstrated that the genetic background of

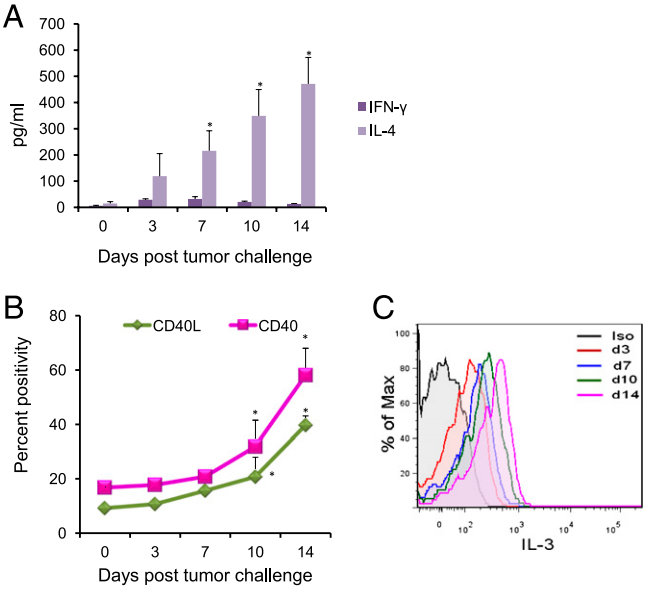

FIGURE 3. Increase in pDC is concomitant with the increase in Th2 cells. (**A**) Serum samples from mice were assayed for levels of IFN-γ and IL-4 by multiplex ELISA, per the manufacturer's instructions, on days 3, 7, 10, and 14 posttumor challenge. Results are expressed as picograms per milliliter of the respective cytokine ± SE ($n = 3$). (**B**) Cells stained for pDC and $CD4^+$ T cell markers were stained for CD40 and CD40L, respectively. Results are shown as percent positivity in the expression of these markers compared with control. (**C**) Cells isolated from BM were cultured in RPMI 1640 in the presence of 5 ng/ml PMA, 500 ng/ml ionomycin, and 1 μg/ml GolgiPlug protein transport inhibitor for 4 h. Cells were then stained with surface Abs to CD3 and CD4. Upon permeabilization, cells were stained with Ab to IL-3. The percentage of IL-3–secreting CD^+ T cells was analyzed by flow cytometry by intracellular staining. Data are a representative curve at each time point. For statistical analysis, six mice were included for each time point, and the experiment was repeated three times independently. $*p < 0.05$, Student t test.

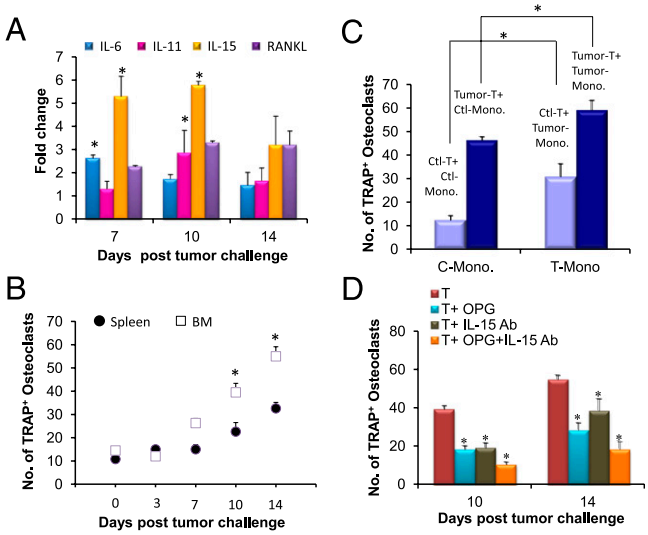

FIGURE 4. RANKL and IL-15 antagonist decrease osteoclast activity during bone metastasis of breast cancer cells. (**A**) RNA was isolated from BM $CD4^+$ T cells, and cDNA was synthesized and used in real-time RT-PCR analysis for IL-6, IL-11, IL-15, and RANKL. Data are presented as fold change in the expression of RNA compared with the control. (**B**) Monocytes and $CD4^+$ T cells isolated from BM and spleen were cocultured at a ratio of 1:100 for osteoclast differentiation. Cells with three or more nuclei were scored as osteoclasts following TRAP staining. (**C**) Monocytes isolated on day 14 from tumor-challenged mice were cocultured with $CD4^+$ T cells from either the tumor-challenged or the control mice for osteoclast differentiation. (**D**) On days 10 and 14, OPG or Ab to IL-15 was added to the cocultures of monocytes and $CD4^+$ T cells individually or in combination. After 10 d, TRAP staining was performed to detect the presence of osteoclasts. The above experiments were performed by isolating cells from six mice for each time point. The experiments were repeated three times independently. $*p < 0.05$, Student t test.

$IFNAR^{-/-}$ mice did not affect the results, because reduced tumor growth and osteolysis were also observed in $IFNAR^{-/-}$ mice on a C57BL/6 background (Supplemental Fig. 4).

Depletion of pDC restores a Th1 type immune response

We next analyzed the effect of pDC depletion on antitumor immunity. As expected, the numbers of pDC were markedly reduced in PDCA-1–injected mice compared with naive and IgG-injected mice (Fig. 7A). Decreased pDC levels resulted in an increase in Th1 cells, with a concomitant decrease in Th2 cells, as assessed by high IFN-γ and low IL-4 levels, respectively in the PDCA-1 Ab-injected group (Fig. 7B). However, in both naive and IgG Ab-injected mice, elevated Th2 cells were seen, as observed previously. Multiplex cytokine analysis further supported the immune profile, showing increased secretion of Th1-associated cytokines (Supplemental Fig. 3). Depletion of pDC also resulted in a decrease in myeloid-derived suppressor cells (MDSC) and Tregs compared with naive and IgG-injected mice (Fig. 7C, 7D). To determine the possible mechanism for reduced tumor growth in pDC-depleted mice, $CD8^+$ T cells were isolated and used in a cytotoxicity assay. Freshly isolated $CD8^+$ T cells from pDC-depleted mice exhibited significantly enhanced cytotoxicity compared with those from naive and IgG groups against 4T1 cells as the target population (Fig. 7E).

We also detected pDC levels in BM of WT and $IFNAR^{-/-}$ mice after tumor challenge. Unlike the elevated pDC levels observed in WT mice, $IFNAR^{-/-}$ mice did not exhibit such high pDC levels (Fig. 7F). This observation coincided with low pDC levels observed in the PDCA-1 Ab-injected group. Both of these groups of mice also showed drastically reduced breast cancer growth and bone metastasis.

Discussion

Studies using tissues from human breast cancer patients have documented infiltration of pDC at the periphery of tumor and at sites of metastasis (18, 19). pDC are also present in lymph nodes carrying breast cancer metastasis (20). However, the significance of this has not been clearly defined. Using metastatic models of breast cancer in immunocompetent mice, the present study initially established and then systematically defined these events connecting cancer growth and osteolysis through immune modulation. The results of these analyses clearly demonstrate that pDC play a key role in this vicious cascade.

From our studies, it is apparent that dissemination of breast cancer to the bone initiates the infiltration of macrophages (Fig. 2A), which produces an inflammatory response, resulting in the triggering of a pDC response (Fig. 2B). Although the signal that induces pDC accumulation has not been identified, it is possible that infiltration of macrophages to the site of invading cancer cells, as well as proliferating breast cancer cells in the bone microenvironment, may cause an increase in the production of Flt-3 ligand. Production of Flt-3 ligand, in turn, has been linked to inflammation in the bone postneoplastic breast cell infiltration (21).

Macrophage differentiation, growth, and chemotaxis are regulated by many growth factors, including CSF-1, GM-CSF, and IL-3, as well as several chemokines, including MCP-1 (CCL-2) and

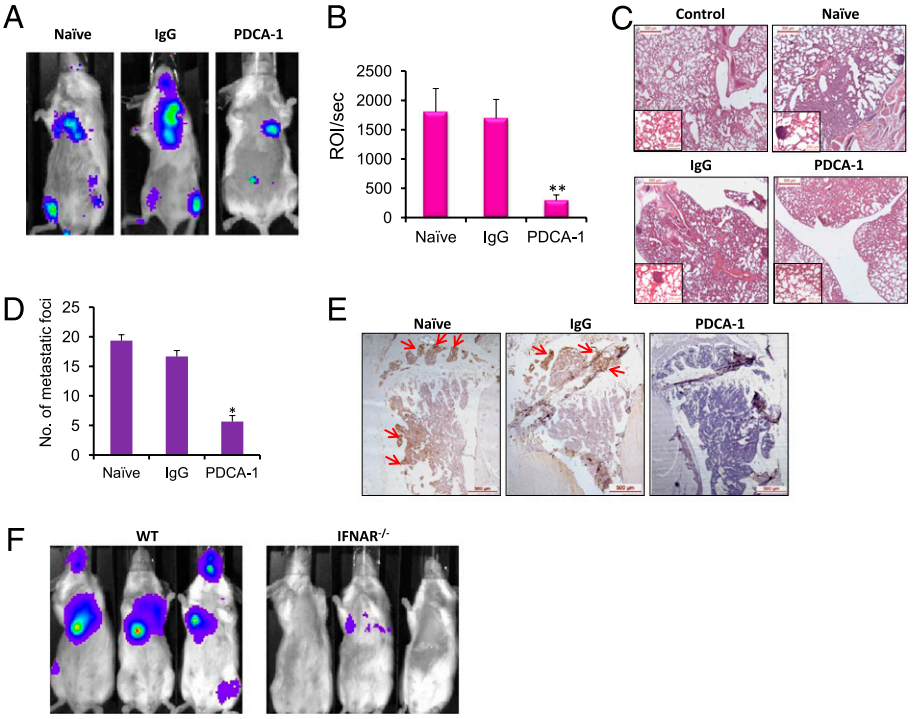

FIGURE 5. Depletion of pDC significantly reduces the growth of breast cancer cells in vivo. (**A**) Representative luciferase imaging of naive, IgG-treated, and PDCA-1–treated mice 12 d after tumor challenge. (**B**) Total luciferase counts from mice of each group 12 d posttumor challenge. (**C**) Paraffin section of lungs from naive, IgG-injected, and PDCA-1–injected mice were stained with H&E. A representative section from each group is shown (*insets*, original magnification ×20). Scale bars, 500 μm. (**D**) Breast cancer metastasis sites in the lungs were counted in naive, IgG-injected, and PDCA-1–injected mice. (**E**) Paraffin sections of tibia from naive, IgG-treated, and PDCA-1–treated mice were stained with cytokeratin-8 Ab. Arrows indicate the presence of breast cancer cells. Scale bars, 500 μm. (**F**) Representative luciferase imaging of 4T1(fLuc) cell-challenged WT and IFNAR$^{-/-}$ mice (BALB/c background) 12 d posttumor challenge. Depletion of pDC was performed twice independently. Three mice were included in naive, IgG, and PDCA-1 groups for each time point. *$p < 0.05$, **$p < 0.01$, Student *t* test.

RANTES (CCL5). MCP-1 overexpression was reported in many cancers, including breast cancer (22–25). Similarly, a significant increase in RANTES was also reported in BM microenvironment of multiple myeloma patients (26). The results of multiplex analysis indicated a significant increase in MCP-1, RANTES, IL-3, and IL-6, suggesting a probable role for these cytokines and growth factors in macrophage infiltration (Supplemental Fig. 1). The levels of proinflammatory cytokines were significantly reduced following pDC depletion, which correlated with an absence of bone metastasis. In contrast, IP-10, a potent inhibitor of both angiogenesis and tumor growth in the bone in vivo (27, 28), was upregulated in pDC-depleted mice (Supplemental Fig. 3), thus supporting the importance of these molecules in suppressing bone metastasis in these mice.

Another notable finding of the current study is elevated levels of pDC Tregs, Th2 cells, and MDSC in the BM compared with the spleen suggesting that the suppressive immune response is polarized more in the BM than in the spleen (data not shown). Because pDC reside mainly in the bone, it was not surprising to note greater levels in the BM; however, a striking discovery in the current study was the prevalence of an increasing pDC population as cancer growth progressed in the bone. pDC activation of CD4$^+$ T cells was

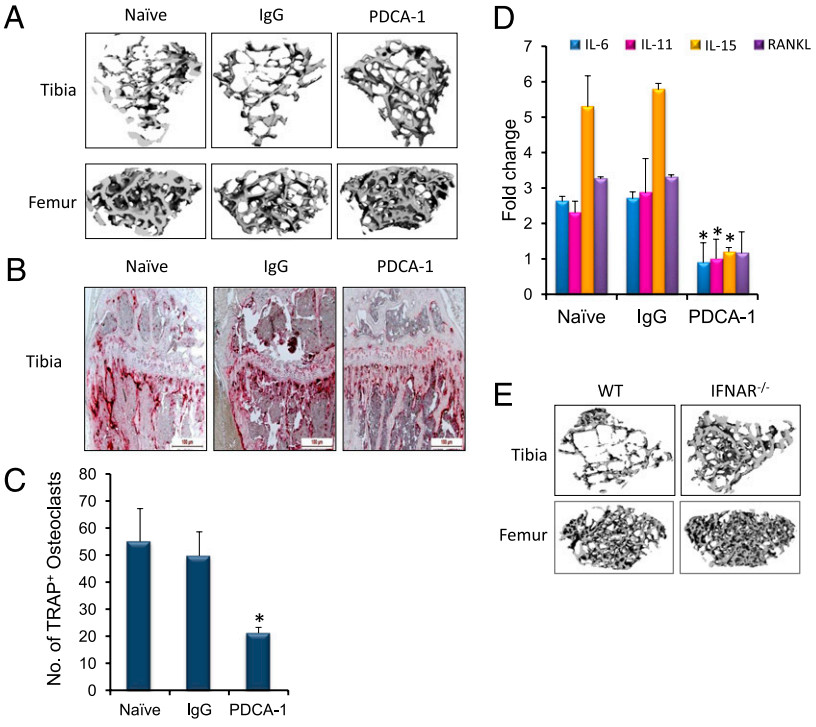

FIGURE 6. Decreased numbers of osteoclasts results in the absence of bone destruction in pDC-depleted mice. (**A**) Twelve days posttumor challenge, tibia and femur from naive and IgG- and PDCA-1–treated mice were subjected to micro-CT analysis. (**B**) Paraffin sections of tibia from naive, IgG-injected, and PDCA-1–injected mice were stained with TRAP 12 d after tumor challenge to detect osteoclasts. Scale bars, 100 μm. (**C**) On day 12 posttumor challenge, monocytes and CD4$^+$ T cells from naive and IgG- and PDCA-1 Ab-injected mice were cocultured to assay osteoclast numbers. (**D**) cDNA from CD4$^+$ T cells of naive and IgG- and PDCA-1 Ab-treated mice were used to detect the levels of IL-6, IL-11, IL-15, and RANKL by real-time RT-PCR. Data are presented as a fold change in expression of RNA compared with the control. (**E**) Micro-CT analysis of tibia and femur from WT and IFNAR$^{-/-}$ mice 12 d posttumor challenge. Data are from three mice for each group. The experiments were repeated twice separately. *$p < 0.05$, Student *t* test.

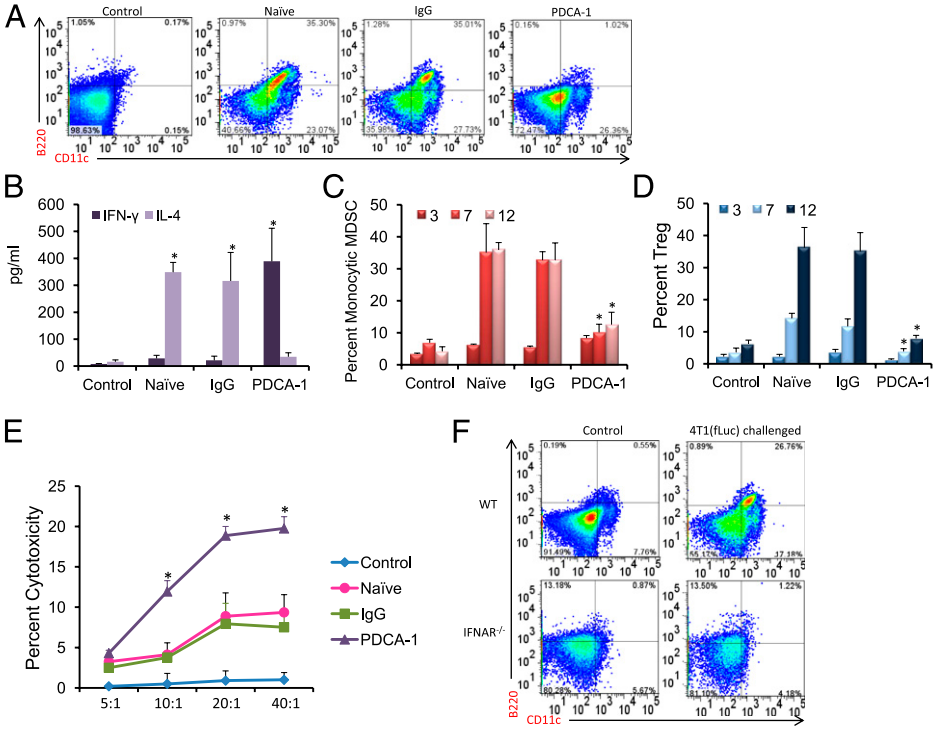

FIGURE 7. Depletion of pDC skews the immune response toward Th1 and results in decreased immunosuppression. (**A**) pDC were detected in BM from naive and IgG- and PDCA-1 Ab-injected mice 12 d posttumor challenge. A representative image from the three groups is presented. (**B**) IFN-γ and IL-4 levels were measured as described previously. (**C**) The numbers of monocytic MDSC ($CD11b^+Gr\text{-}1^+Ly6C^+Ly6G^{lo}$) in the BM after pDC depletion were enumerated by flow cytometry. (**D**) The presence of Tregs was detected by staining BM cells from control and IgG- and PDCA-1 Ab-treated mice. (**E**) $CD8^+$ T cells isolated from the BM of IgG- and PDCA-1–treated animals 3 d posttumor challenge were used as the effector population, and 4T1(fLuc) cells were used as the target population. A cytotoxicity assay was carried out using a commercially available kit. (**F**) The presence of pDC was detected in BM from WT and $IFNAR^{-/-}$ mice 12 d posttumor challenge. Mice with no tumor challenge were included as the control group. A representative image for each group, showing the percentage of pDC, is presented. The flow cytometry and cytotoxicity assay data are from three mice for each group and for each time point. The experiments were repeated twice independently. $*p < 0.05$, Student t test.

correlated with higher CD40 expression on pDC and higher CD40L expression on $CD4^+$ T cells, along with increased IL-3 production by $CD4^+$ T cells. This ligation was maintained throughout the period of progressive cancer burden and bone destruction, suggesting that constant stimulation of $CD4^+$ T cells by pDC is critical for skewing and maintaining the immune response toward a Th2 phenotype (29, 30). Concomitant with this effect, the osteolytic cytokines IL-3, IL-6, IL-11, and IL-15 were maintained at elevated levels (31, 32).

Skewing of the immune response toward the Th2 phenotype was associated with a decreased Th1 response. Elevated Th2-associated cytokines IL-13, IL-4, and IL-5, along with low levels of Th1 cytokines, such as IP-10 and IFN-γ (Fig. 3, Supplemental Fig. 3), further maintained Th2 polarization. At the initial stage of cancer dissemination (notably days 3 and 7), there was an initial spike in Th1 cells (Fig. 3). This observation suggests that, although a significant Th1 response was not noted during the progressive stages of breast cancer dissemination, a notable increase in Th1 cells during the first few days caused an initial influx of antitumor activity-inducing immune effector cells, which may have been dampened by a gradual increase in pDC and Th2 cells and associated cytokine production, facilitating immunosuppression, tumor growth, and osteolysis.

It was not surprising to observe increased levels of both Tregs and MDSC in the bone microenvironment. Both of these immunosuppressive cells are known to be upregulated in the presence of IL-10 and TGF-β (33). Interestingly, activated Tregs were noted even at a late stage of the disease, when the overall host immune response may have been greatly dampened due to increased tumor burden. Recent studies showed that MDSC induce immune suppression and allow the progression of several cancers, including breast cancer, and a reduction in MDSC significantly delays primary tumor growth (34–37).

The significance of high pDC numbers and a shift in T cell homeostasis in promoting tumor growth, immunosuppression, and osteolytic bone damage was further confirmed by depletion of the pDC population prior to tumor challenge. Dampening of the pDC response resulted in a greater decrease of tumor growth in the bone, as well as in other metastatic sites, including lungs and liver. The results indicated a shift from a Th2 to a Th1 immune response following pDC depletion, as evidenced by an increase in IL-12 production (Supplemental Fig. 3) and activated Th1 cells. A cytotoxicity assay using $CD8^+$ T cells isolated from pDC-depleted mice further confirmed a direct effect on both the reversal to Th1 polarization and antitumor activity in the bone and in visceral tissues, along with an increase in IFN-γ levels. Thus, it remains possible that augmentation of antitumor immunity may be achieved in breast cancer patients by depleting pDC accumulation (18, 19).

Coupled with other cancer immunotherapy strategies, such as active immune response through tumor Ag-specific vaccines or treatments aimed at nonspecific activation of immune effectors by passive immunotherapy, including GM-CSF and IL-2 therapies, pDC-depletion therapy is likely to promote an augmented antitumor effect and extend survival. A remarkable decrease in the production of osteolytic cytokines following pDC depletion also strongly suggests that incorporation of this unique axis into therapy regimens will improve bone remodeling significantly and decrease progressive bone loss in patients with breast cancer.

Acknowledgments

We thank Enid Keyser for technical assistance with flow cytometry and sorting and the Analytical and Preparative Cytometry Facility (supported by National Institutes of Health Grant P30 AR48311) of the Comprehensive Arthritis, Musculoskeletal and Autoimmunity Center at the University of Alabama at Birmingham (UAB). Noninvasive imaging was carried out at UAB's Small Animal Imaging facility. Bone histomorphometry and micro-CT analyses were performed at UAB's Bone Histomorphometry Core and Small Animal Bone Phenotyping Core, respectively. Flow cytometry analysis was performed at the UAB Center for AIDS Research Core facility.

Disclosures

The authors have no financial conflicts of interest.

References

1. Lippman, M. E. 2011. Breast cancer. In *Harrison's Principles of Internal Medicine*. *Part 7*. 18th Ed. Dan L. Longo, Anthony Fauci, Dennis Kasper, Stephen Hauser, J. Larry Jameson, and Joseph Loscalzo, eds. McGraw-Hill, New York, p. 516–523.
2. Roodman, G. D. 2004. Mechanisms of bone metastasis. *N. Engl. J. Med.* 350: 1655–1664.
3. Mundy, G. R. 2002. Metastasis to bone: causes, consequences and therapeutic opportunities. *Nat. Rev. Cancer* 2: 584–593.
4. Takayanagi, H. 2009. Osteoimmunology and the effects of the immune system on bone. [Published erratum appears in 2010 *Nat. Rev. Rheumatol.* 6: 4.] Nat. Rev. Rheumatol. 5: 667–676.
5. Kong, Y. Y., and J. M. Penninger. 2000. Molecular control of bone remodeling and osteoporosis. *Exp. Gerontol.* 35: 947–956.
6. Bussard, K. M., C. V. Gay, and A. M. Mastro. 2008. The bone microenvironment in metastasis; what is special about bone? *Cancer Metastasis Rev.* 27: 41–55.
7. Cao, Q., W. Cai, G. Niu, L. He, and X. Chen. 2008. Multimodality imaging of IL-18–binding protein-Fc therapy of experimental lung metastasis. *Clin. Cancer Res.* 14: 6137–6145.
8. Bernt, K. M., S. Ni, A. T. Tieu, and A. Lieber. 2005. Assessment of a combined, adenovirus-mediated oncolytic and immunostimulatory tumor therapy. *Cancer Res.* 65: 4343–4352.
9. Chen, Y., and S. R. Rittling. 2003. Novel murine mammary epithelial cell lines that form osteolytic bone metastases: effect of strain background on tumor homing. *Clin. Exp. Metastasis* 20: 111–120.
10. Bailey-Bucktrout, S. L., S. C. Caulkins, G. Goings, J. A. Fischer, A. Dzionek, and S. D. Miller. 2008. Cutting edge: central nervous system plasmacytoid dendritic cells regulate the severity of relapsing experimental autoimmune encephalomyelitis. *J. Immunol.* 180: 6457–6461.
11. Chanda, D., T. Isayeva, S. Kumar, J. A. Hensel, A. Sawant, G. Ramaswamy, G. P. Siegal, M. S. Beatty, and S. Ponnazhagan. 2009. Therapeutic potential of adult bone marrow-derived mesenchymal stem cells in prostate cancer bone metastasis. *Clin. Cancer Res.* 15: 7175–7185.
12. Erlebacher, A., and R. Derynck. 1996. Increased expression of TGF-beta 2 in osteoblasts results in an osteoporosis-like phenotype. *J. Cell Biol.* 132: 195–210.
13. duPre', S. A., D. Redelman, and K. W. Hunter, Jr. 2008. Microenvironment of the murine mammary carcinoma 4T1: endogenous IFN-gamma affects tumor phenotype, growth, and metastasis. *Exp. Mol. Pathol.* 85: 174–188.
14. Palmqvist, P., P. Lundberg, E. Persson, A. Johansson, I. Lundgren, A. Lie, H. H. Conaway, and U. H. Lerner. 2006. Inhibition of hormone and cytokine-stimulated osteoclastogenesis and bone resorption by interleukin-4 and interleukin-13 is associated with increased osteoprotegerin and decreased RANKL and RANK in a STAT6-dependent pathway. *J. Biol. Chem.* 281: 2414–2429.
15. Rissoan, M.-C., V. Soumelis, N. Kadowaki, G. Grouard, F. Briere, R. de Waal Malefyt, and Y. J. Liu. 1999. Reciprocal control of T helper cell and dendritic cell differentiation. *Science* 283: 1183–1186.
16. Muller, A. J., M. D. Sharma, P. R. Chandler, J. B. Duhadaway, M. E. Everhart, B. A. Johnson, III, D. J. Kahler, J. Pihkala, A. P. Soler, D. H. Munn, et al. 2008. Chronic inflammation that facilitates tumor progression creates local immune suppression by inducing indoleamine 2,3 dioxygenase. *Proc. Natl. Acad. Sci. USA* 105: 17073–17078.
17. Asselin-Paturel, C., G. Brizard, K. Chemin, A. Boonstra, A. O'Garra, A. Vicari, and G. Trinchieri. 2005. Type I interferon dependence of plasmacytoid dendritic cell activation and migration. *J. Exp. Med.* 201: 1157–1167.
18. Ferrari, S., F. Malugani, B. Rovati, C. Porta, A. Riccardi, and M. Danova. 2005. Flow cytometric analysis of circulating dendritic cell subsets and intracellular cytokine production in advanced breast cancer patients. *Oncol. Rep.* 14: 113–120.
19. Treilleux, I., J. Y. Blay, N. Bendriss-Vermare, I. Ray-Coquard, T. Bachelot, J. P. Guastalla, A. Bremond, S. Goddard, J. J. Pin, C. Barthelemy-Dubois, and S. Lebecque. 2004. Dendritic cell infiltration and prognosis of early stage breast cancer. *Clin. Cancer Res.* 10: 7466–7474.
20. Horny, H. P., A. C. Feller, H. A. Horst, and K. Lennert. 1987. Immunocytology of plasmacytoid T cells: marker analysis indicates a unique phenotype of this enigmatic cell. *Hum. Pathol.* 18: 28–32.
21. Cohen, P. A., G. K. Koski, B. J. Czerniecki, K. D. Bunting, X. Y. Fu, Z. Wang, W. J. Zhang, C. S. Carter, M. Awad, C. A. Distel, et al. 2008. STAT3- and STAT5-dependent pathways competitively regulate the pan-differentiation of CD34pos cells into tumor-competent dendritic cells. *Blood* 112: 1832–1843.
22. Fujimoto, H., T. Sangai, G. Ishii, A. Ikehara, T. Nagashima, M. Miyazaki, and A. Ochiai. 2009. Stromal MCP-1 in mammary tumors induces tumor-associated macrophage infiltration and contributes to tumor progression. *Int. J. Cancer* 125: 1276–1284.
23. Ksiazkiewicz, M., E. Gottfried, M. Kreutz, M. Mack, F. Hofstaedter, and L. A. Kunz-Schughart. 2010. Importance of CCL2-CCR2A/2B signaling for monocyte migration into spheroids of breast cancer-derived fibroblasts. *Immunobiology* 215: 737–747.
24. Lazar, M., J. Sullivan, G. Chipitsyna, T. Aziz, A. F. Salem, Q. Gong, A. Witkiewicz, D. T. Denhardt, C. J. Yeo, and H. A. Arafat. 2010. Induction of monocyte chemoattractant protein-1 by nicotine in pancreatic ductal adenocarcinoma cells: role of osteopontin. *Surgery* 148: 298–309.
25. Mishra P., D. Banerjee, and A. Ben-Baruch. 2011. Chemokines at the crossroads of tumor-fibroblast interactions that promote malignancy. *J. Leukoc. Biol.* 89: 31–39.
26. Cao, Y., T. Luetkens, S. Kobold, Y. Hildebrandt, M. Gordic, N. Lajmi, S. Meyer, K. Bartels, A. R. Zander, C. Bokemeyer, et al. 2010. The cytokine/chemokine pattern in the bone marrow environment of multiple myeloma patients. *Exp. Hematol.* 38: 860–867.
27. Angiolillo, A. L., C. Sgadari, D. D. Taub, F. Liao, J. M. Farber, S. Maheshwari, H. K. Kleinman, G. H. Reaman, and G. Tosato. 1995. Human interferon-inducible protein 10 is a potent inhibitor of angiogenesis in vivo. *J. Exp. Med.* 182: 155–162.
28. Dufour, J. H., M. Dziejman, M. T. Liu, J. H. Leung, T. E. Lane, and A. D. Luster. 2002. IFN-gamma-inducible protein 10 (IP-10; CXCL10)-deficient mice reveal a role for IP-10 in effector T cell generation and trafficking. *J. Immunol.* 168: 3195–3204.
29. Chaperot, L., I. Perrot, M. C. Jacob, D. Blanchard, V. Salaun, V. Deneys, S. Lebecque, F. Brière, J. C. Bensa, and J. Plumas. 2004. Leukemic plasmacytoid dendritic cells share phenotypic and functional features with their normal counterparts. *Eur. J. Immunol.* 34: 418–426.
30. Martín-Gayo, E., E. Sierra-Filardi, A. L. Corbí, and M. L. Toribio. 2010. Plasmacytoid dendritic cells resident in human thymus drive natural Treg cell development. *Blood* 115: 5366–5375.
31. Lebre, M. C., S. L. Jongbloed, S. W. Tas, T. J. Smeets, I. B. McInnes, and P. P. Tak. 2008. Rheumatoid arthritis synovium contains two subsets of CD83−DC−LAMP− dendritic cells with distinct cytokine profiles. *Am. J. Pathol.* 172: 940–950.
32. Nasrazadani, A., and C. L. Van Den Berg. 2011. c-Jun N-terminal Kinase 2 Regulates Multiple Receptor Tyrosine Kinase Pathways in Mouse Mammary Tumor Growth and Metastasis. *Genes Cancer* 2: 31–45.
33. Jia, W., C. Jackson-Cook, and M. R. Graf. 2010. Tumor-infiltrating, myeloid-derived suppressor cells inhibit T cell activity by nitric oxide production in an intracranial rat glioma + vaccination model. *J. Neuroimmunol.* 223: 20–30.
34. Sinha, P., V. K. Clements, S. K. Bunt, S. M. Albelda, and S. Ostrand-Rosenberg. 2007. Cross-talk between myeloid-derived suppressor cells and macrophages subverts tumor immunity toward a type 2 response. *J. Immunol.* 179: 977–983.
35. Corzo, C. A., T. Condamine, L. Lu, M. J. Cotter, J. I. Youn, P. Cheng, H. I. Cho, E. Celis, D. G. Quiceno, T. Padhya, et al. 2010. HIF-1α regulates function and differentiation of myeloid-derived suppressor cells in the tumor microenvironment. *J. Exp. Med.* 207: 2439–2453.
36. Cao, M., Y. Xu, J. I. Youn, R. Cabrera, X. Zhang, D. Gabrilovich, D. R. Nelson, and C. Liu. 2011. Kinase inhibitor Sorafenib modulates immunosuppressive cell populations in a murine liver cancer model. *Lab. Invest.* 91: 598–608.
37. Fujita, M., G. Kohanbash, W. Fellows-Mayle, R. L. Hamilton, Y. Komohara, S. A. Decker, J. R. Ohlfest, and H. Okada. 2011. COX-2 blockade suppresses gliomagenesis by inhibiting myeloid-derived suppressor cells. *Cancer Res.* 71: 2664–2674.

Published OnlineFirst December 14, 2012; DOI: 10.1158/0008-5472.CAN-12-2202

Myeloid-Derived Suppressor Cells Function as Novel Osteoclast Progenitors Enhancing Bone Loss in Breast Cancer

Anandi Sawant[1], Jessy Deshane[2], Joel Jules[1], Carnella M. Lee[1], Brittney A. Harris[1], Xu Feng[1], and Selvarangan Ponnazhagan[1]

Abstract

Enhanced bone destruction is a hallmark of various carcinomas such as breast cancer, where osteolytic bone metastasis is associated with increased morbidity and mortality. Immune cells contribute to osteolysis in cancer growth, but the factors contributing to aggressive bone destruction are not well understood. In this study, we show the importance of myeloid-derived suppressor cells (MDSC) in this process at bone metastatic sites. Because MDSC originate from the same myeloid lineage as macrophages, which are osteoclast precursors, we hypothesized that MDSC may undergo osteoclast differentiation and contribute to enhanced bone destruction and tumor growth. Using an immunocompetent mouse model of breast cancer bone metastasis, we confirmed that MDSC isolated from the tumor-bone microenvironment differentiated into functional osteoclasts both *in vitro* and *in vivo*. Mechanistic investigations revealed that nitric oxide signaling was critical for differentiation of MDSC into osteoclasts. Remarkably, osteoclast differentiation did not occur in MDSC isolated from control or tumor-bearing mice that lacked bone metastasis, signifying the essential cross-talk between tumor cells and myeloid progenitors in the bone microenvironment as a requirement for osteoclast differentiation of MDSC. Overall, our results identify a wholly new facet to the multifunctionality of MDSC in driving tumor progression, in this case as a novel osteoclast progenitor that specifically drives bone metastasis during cancer progression. *Cancer Res; 73(2); 672–82. ©2012 AACR.*

Introduction

Myeloid-derived suppressor cells (MDSC) play a pivotal role in cancer progression by suppressing both innate as well as adaptive immunity (1, 2). Accumulation of MDSC has been reported in almost all cancers, both in preclinical models and human patients (3–5). Tumor progression is associated with gradual accumulation of MDSC in the blood, lymph nodes, and spleen. MDSC accumulate in the primary tumor as well as at the metastatic tumor sites. Recent studies have substantiated that MDSC inhibit the antitumor immunity and promote tumor expansion and metastasis at distant sites, including the bone (6, 7). An increase in the infiltration of MDSC in the bone marrow has also been reported in tumor-bearing mice. Further, elimination or reduction in MDSC numbers significantly delays and limits tumor growth in the bone (8).

Authors' Affiliations: Departments of [1]Pathology and [2]Medicine, The University of Alabama at Birmingham, Birmingham, Alabama

Note: Supplementary data for this article are available at Cancer Research Online (http://cancerres.aacrjournals.org/).

Corresponding Author: Selvarangan Ponnazhagan, The University of Alabama at Birmingham, 1825 University Boulevard, SHEL 814, Birmingham, AL 35294-2182. Phone: 205-934-6731; Fax: 205-975-4919; E-mail: pons@uab.edu

doi: 10.1158/0008-5472.CAN-12-2202

Bone is 1 of the major metastatic sites for carcinomas of the breast, prostate, and lung as well as multiple myeloma (9). Approximately 65% to 80% of patients with disseminated breast disease show skeletal metastasis (10, 11). In order for cancer to establish in the bone, tumor cells secrete a variety of growth factors and cytokines that induce differentiation and activation of osteoclasts, which degrade bone, facilitating tumor growth. During normal bone remodeling, macrophages and monocytes remain the major precursors of osteoclasts (12). Stimulation of these cells *in vitro* with macrophage colony-stimulating factor (M-CSF) and receptor activator of NF-κB ligand (RANKL) induces their differentiation into multinucleated osteoclasts.

MDSC are a heterogeneous population comprising of immature myeloid cells (IMC). Under normal conditions, the IMC differentiate into mature macrophages, dendritic cells, and granulocytes. However, in pathologic conditions including cancer, IMC differentiation is inhibited resulting in the accumulation of immunosuppressive MDSC (13). Because MDSC are progenitors of macrophages, which differentiate into osteoclasts, and MDSC numbers are elevated in breast cancer patients, we sought to determine if MDSC in the tumor microenvironment within the bone undergo osteoclast differentiation and contribute to enhanced bone destruction and tumor growth in an immunocompetent mouse model of breast cancer.

Results of the studies clearly showed that MDSC from tumor-bearing mice with bone metastasis differentiate into

Published OnlineFirst December 14, 2012; DOI: 10.1158/0008-5472.CAN-12-2202

functional osteoclasts. Further, investigation of the underlying molecular mechanisms of MDSC differentiation into osteoclasts indicates nitric oxide (NO) signaling as the key pathway regulating the differentiation. Collectively, the present study reports a novel role for MDSC as osteoclast-forming cells, contributing to enhanced osteolysis during breast cancer bone dissemination. As MDSC are elevated in other osteolytic cancers, it remains possible that such osteolytic potential of MDSC may play a vital role in increased bone destruction and growth of tumors in the bone microenvironment, and targeting MDSC can be an effective strategy to reduce skeletal morbidity in osteolytic cancers.

Materials and Methods

Isolation of MDSC

Female BALB/c mice were injected with 10^5 4T1(fLuc) cells, a kind gift from Dr. Xiaoyuan Chen (Stanford University), via the intracardiac route. After 10 to 12 days, when bone metastases were observed by noninvasive luciferase imaging, mice were sacrificed and bone marrow cells were collected. RBCs were lysed using the ACK RBC lysis buffer. Cells were incubated with Fc block for 15 minutes at 4°C. For sorting of total MDSC population ($MDSC^{(+bone\ mets)}$), cells were stained with APC-conjugated anti-CD11b antibody and PE-Cy7-conjugated Gr-1 antibody (eBioscience) for 30 minutes at 4°C. After washing with sterile PBS, $CD11b^+Gr\text{-}1^+$ MDSC were sorted using BD FACS ARIA III (BD Biosciences). $CD11b^+Gr\text{-}1^+$ MDSC were further stained for additional markers including CD115 PE, F4/80 PE Cy5, CD80 FITC, Ly6C Per CP Cy 5.5, and Ly6G PE antibodies. MDSC were isolated from inguinal, axillary, branchial, and thymus lymph nodes ($MDSC^{(Lymph\ nodes)}$), lungs ($MDSC^{(Lungs)}$), blood ($MDSC^{(Blood)}$), and spleen ($MDSC^{(Spleen)}$) of tumor-challenged mice showing bone metastasis. MDSC were also isolated from tumor-bearing mice but without visible bone metastasis ($MDSC^{(-bone\ mets)}$) and from age-matched control mice ($MDSC^{(control)}$). Expression of arginase and iNOS were detected by permeabilization of cells and staining with iNOS-PE antibody and arginase antibody followed with Alexa 488-conjugated secondary antibody (eBioscience).

In vitro osteoclastogenesis assay

For the assay, 10^5 MDSC were seeded in 200 μL α-MEM medium in a 48-well plate (Corning Inc.) in the presence of 44 ng/mL M-CSF and 100 ng/mL RANKL (kind gifts from Dr. Xu Feng, The University of Alabama at Birmingham, Birmingham, AL; ref. 14). For some experiments, 25 μmol/L NG-monomethyl-L-arginine, monoacetate salt (L-NMMA) was added to the MDSC cultures (a kind gift from Dr. J. Zmijewski, The University of Alabama at Birmingham, Birmingham, AL; ref, 15). Media was changed every 2 days. On days 8 to 9, the presence of osteoclasts was detected by tartarate-resistant acid phosphatase (TRAP) staining. Briefly, media was removed carefully and cells were washed once in PBS before fixing in 0.2 mol/L acetate buffer for 20 minutes at room temperature (RT). At the end of incubation, cells were stained in 0.2 mmol/L acetate buffer containing 0.5 mg/mL naphtol AS-MX phosphate and 1.1 mg/mL fast-red TR salt (Sigma-Aldrich) for 30 to 45 minutes at 37°C till color change was noted. Nuclei were stained using hematoxylin for 30 seconds. Cells were washed twice in PBS and suspended in PBS (16). Cells showing 3 or more nuclei were considered as osteoclast. As a positive control, bone marrow-derived macrophages (BMM) from tumor-bearing mice were cultured under identical conditions. All assays were conducted in triplicate.

In vitro bone resorption assay

MDSC and BMMs (10^5 cells/well) were seeded on bovine cortical bone slices plated in 24-well culture plates and cultured under conditions indicated in individual experiments to promote osteoclast formation and bone resorption. The bone slices were then harvested, and the cells were subsequently removed with 0.25 mol/L ammonium hydroxide and mechanical agitation. Bone slices were analyzed using an Olympus FluorView 300 Laser Scanning Confocal Microscope. A quantitative analysis of osteolysis was conducted by measuring the percentage of the resorbed areas as compared with the entire bone surface using Adobe Photoshop Software.

In vivo MDSC depletion

To deplete MDSC *in vivo*, mice were injected intraperitoneally with 1.5 mg gemcitabine (Sigma-Aldrich) twice in the first week and once per week thereafter (17, 18). Treatment was started on day 10 post-4T1(fLuc) challenge, by when tumor was established and metastasis to the bone was confirmed by luciferase imaging. Upon sacrifice of mice on day 17 post-tumor challenge, MDSC were sorted from the bone marrow of gemcitabine-treated mice and were differentiated into osteoclasts as described earlier. MDSC from non–gemcitabine-treated mice were included as controls.

In vivo MDSC transfer assay

MDSC were isolated from the bone of tumor-bearing mice with bone metastasis ($MDSC^{(+bone\ mets)}$), as described earlier. A total of 2.5×10^5 MDSC in 50 μL PBS were injected in the long bones of BALB/c mice and was followed by a second injection of MDSC after 4 days. As a control, PBS was injected. Alternatively, before injection of $MDSC^{(+bone\ mets)}$ *in vivo*, mice were injected with 1400W (10 mg/kg body weight; Cayman Chemical Company) intraperitoneally, 2 days before the $MDSC^{(+bone\ mets)}$ injection. Injections were given every 2 days till the end of the experiment. On day 10, mice were sacrificed and femur and tibia were collected and fixed in 4% buffered-formalin for 2 days and were subjected to micro-CT analysis (Micro-CT40; SCANCO Medical). The formalin-fixed bones were then decalcified in 2.5% EDTA, at pH 8.0, for 2 weeks. Thereafter, 5-μm paraffin-embedded sections were used for histology.

To show that transferred MDSC differentiated into osteoclasts *in vivo*, $MDSC^{(+bone\ mets)}$ from tumor-challenged BALB/c mice (CD45.2 genotype) were injected into long bones of congeneic, non–tumor-challenged $CD45.1^+$ female BALB/c mice as described earlier. After 8 days, mice were sacrificed and bone marrow cells were collected. Cells were stained with CD45.2-PE antibody to detect the presence of adoptively transferred MDSC. Cells were also stained with antibody to

Published OnlineFirst December 14, 2012; DOI: 10.1158/0008-5472.CAN-12-2202

cathepsin-k (osteoclast marker) followed by Alexa 488 conjugated secondary antibody. MDSC that stained positive for CD45.2 and cathepsin-k were sorted and differentiated *in vitro* into osteoclasts as described earlier.

In vitro suppression assay

Following sacrifice of tumor-challenged mice with bone metastasis, MDSC were sorted from the bone marrow ($MDSC^{(+\ bone\ mets)}$) and $CD4^+$ T cells were sorted from the spleen. $CD4^+$ T cells were then labeled with carboxyfluorescein diacetate and succinimidyl ester (CFSE) according to the manufacturer's instructions (Molecular Probes). Following labeling, CFSE-$CD4^+$ T cells were cultured with MDSC in 1:1 ratio in media containing 0.75 μg/mL anti-CD3 and 4 μg/mL anti-CD28 antibodies together with 50 μmol/L β-mercaptoethanol for 72 hours. As a control, $CD4^+$ T cells were cultured in the absence of MDSC. After 72 hours, cells were harvested and the presence of $CD4^+$ T cells labeled with CFSE was detected by flow cytometry.

Immunohistochemistry

The presence of osteoclasts within the bone sections was detected by TRAP staining as described previously (16). All the microscopic images were obtained using a Leica DMI4000B microscope, attached to a Leica DFC500 digital camera. The LASv3.6.0 software was used to optimize picture quality. A region of interest was selected that was exactly 250 μm distal to the growth plate, and extending 1 mm downward (thereby avoiding the primary spongiosa) through the metaphysis of the femur and tibia. Standard bone histomorphometry was carried out by using Bioquant Image Analysis software (R&M Biometrics; ref. 19). The number of osteoclasts per bone surface was calculated.

Semiquantitative reverse transcription PCR

Total RNA was isolated from MDSC and BMMs using TRIzol reagent (Invitrogen). Then, 1 μg of total RNA was reversed-transcribed to cDNA with an iScriptcDNA synthesis kit (Bio-Rad). PCR amplification was carried out using primers specific for MMP9, TRAP, carbonic anhydrase II (Car2), cathepsin K (Ctsk), and GAPDH using the following condition: preheating at 95°C for 2 minutes, denaturation at 95°C for 30 seconds, annealing at 58°C for 30 seconds, and extension at 72°C for 30 seconds in a 30-cycle reaction, followed by final extension at 72°C for 5 minutes. PCR was carried out with the Dream Taq Green 2× PCR mix from Fermentas in a 50-μL reaction volume. The PCR primer sequences used are

MMP-9
Forward 5′-CTTCTTCTCTGGACGTCAAATG-3′
Reverse 5′-CATTTTGGAAACTCACACGCC-3′
Car2
Forward 5′-AGAGAACTGGCACAAGGACTT-3′
Reverse 5′-CCTCCTTTCAGCACTGCATTGT-3′
Ctsk
Forward 5′-GATGCTTACCCATATGTGGGC-3′
Reverse 5′-CATATCCTTTGTTTCCCCAGC-3′
TRAP
Forward 5′-GCCAAGATGGATTCATGGGTGG-3′
Reverse 5′-CAGAGACATGATGAAGTCAGCG-3′
GAPDH
Forward 5′-ACATCATCCCTGCATCCACTG-3′
Reverse 5′-TCATTGAGAGCAATGCCAGC-3′

Thirty microliters of PCR mixture was separated on 2% agarose gel for electrophoretic analysis. All semiquantitative reverse transcription PCR (RT-PCR) assays were independently conducted at least 3 times.

Western blot analysis

$MDSC^{(+bone\ mets)}$, $MDSC^{(-bone\ mets)}$, $MDSC^{(Lymph\ nodes)}$, $MDSC^{(Lungs)}$, $MDSC^{(Blood)}$, and $MDSC^{(Spleen)}$ were sorted from tumor-bearing mice as described earlier. Whole-cell lysates were prepared using RIPA buffer containing protease and phosphatase inhibitors according to the manufacturer's instructions (Thermo Scientific). Protein concentrations were measured using a commercially available BCA protein assay kit (Thermo Scientifc). For each sample, 100 μg of protein was used to detect the levels of HIF-1α, Phospho-ERK, Phospho-phosphoinositol 3 (PI3) kinase, Phospho–Akt, Total ERK, Total-PI3 kinase, Total-Akt, and β-actin by Western blot analysis. Following denaturation, the samples were separated on a 10% polyacrylamide gel and transferred to nitrocellulose membranes (Millipore) followed by blocking with 2% non-fat milk and incubation with primary antibodies, overnight at 4°C. The β-actin antibody was used as a loading control. After washing, the primary antibody with 1× tris-buffered saline with Tween-20 (TBST; 3 × 10 minutes) and suitable secondary antibodies, conjugated to horseradish peroxidase, were applied for 1 hour at room temperature, then washed with TBST (3 × 10 minutes) and blots were then incubated with enhanced chemiluminescence reagent (GE Healthcare Life Sciences) according to the manufacturer's instructions and developed on a Fuji LAS-3000 chemiluminescence developer. All the primary antibodies were obtained from Cell Signaling and were used at the recommended dilutions. A donkey anti-rabbit secondary antibody was used for all the proteins except for HIF-1α, for which a sheep anti-mouse secondary antibody was used. Both the secondary antibodies were purchased from GE Healthcare Life Sciences.

Measurement of nitric oxide

Levels of NO were detected by using 4-amino-5-methylamino-2′, 7′-difluorofluorescein diacetate (DAF-FMDA; Molecular Probes) reagent and the Griess Reagent (Promega) according to the manufacturer's instructions. Briefly, MDSC (10^4 cells/well) were cultured in the presence of RANKL and M-CSF for 3 days as described earlier. As controls, MDSC grown in LPS alone and MDSC grown in LPS together with RANKL and M-CSF were included (20). For detecting NO levels by using the Griess reagent, culture supernatants were collected from MDSC differentiating into osteoclasts at different time points under conditions mentioned earlier. The assay was conducted according to the manufacturer's instructions and data was normalized to a standard curve (with known concentrations of

Published OnlineFirst December 14, 2012; DOI: 10.1158/0008-5472.CAN-12-2202

nitrite) and expressed as final nitrite concentrations in media (21). NO levels were also measured for MDSC cultures differentiating into osteoclasts in the presence of L-NMMA, an NO inhibitor. The assay was repeated at least 3 times.

Measurement of arginase activity

The concentration of urea, an end product of the arginase pathway, was used as an estimate of the arginase activity in the culture supernatants of MDSC differentiating into osteoclasts. Controls were MDSC cultured in LPS alone and together with RANKL and M-CSF. Detection of urea was carried out using the Quantichrom Urea Assay kit (BioAssay Systems; ref. 20). The results are reported as urea concentrations in media. Results are derived from 3 different samples tested in triplicate.

Measurement of superoxide

Superoxide levels in MDSC differentiating into osteoclasts were detected by flow cytometry by incubating for 20 minutes at room temperature with dihydroxyethidium (DHE, 10 μmol/L; Molecular Probes) according to the manufacturer's recommendations. Cells were then washed twice in PBS and the percentage of positive cells were determined by flow cytometry (20). As controls, MDSC grown in LPS alone and in LPS together with RANKL and M-CSF were included. The assay was conducted at least 3 times.

Statistical analysis

Data were analyzed by 1-way ANOVA. A Tukey test was also applied for multiple comparisons wherever applicable. Values provided are the mean ± SE, and the differences were considered significant if P was less than 0.05.

Results

Isolation and characterization of MDSC from the breast cancer bone metastasis model

For identifying a possible role of MDSC as osteoclast progenitors, an osteolytic breast cancer cell line constitutively expressing firefly luciferase 4T1(fLuc), syngeneic in BALB/c mice, was injected via the intracardiac route into syngeneic and immunocompetent BALB/c mice. Bone metastasis was confirmed in the tumor-bearing mice after 10 to 12 days post-challenge by noninvasive imaging. MDSC populations in the bone marrow were characterized using specific cell surface markers. The CD11b and Gr-1 MDSC phenotype was further confirmed as the population that was $CD80^{Lo}$, $CD115^{+}$, and $F4/80^{-}$ (Supplementary Fig. S1). The absence of F4/80 indicated that these cells were not already committed to differentiate into macrophages. The MDSC were a mixed population of granulocytic $Ly6C^{+}Ly6G^{+}$ cells and monocytic $Ly6C^{+}Ly6G^{-}$ MDSC. MDSC were isolated from both bone marrow and lung using the same phenotype. Further, the isolated MDSC actively suppressed proliferation of splenic $CD4^{+}$ T cells; thus establishing that these are indeed immunosuppressive cells (Supplementary Fig. S1).

MDSC have potential to differentiate into osteoclasts

To determine if MDSC differentiated into osteoclasts, MDSC isolated from the bone marrow of tumor-bearing mice with bone metastasis ($MDSC^{(+bone\ mets)}$) were cultured in medium containing M-CSF and RANKL. MDSC from the lungs of tumor-bearing mice with metastasized tumor ($MDSC^{(+lung\ mets)}$) and from bone marrow of tumor-bearing mice but without bone metastasis ($MDSC^{(-bone\ mets)}$) were also included in the study. BMMs were used as a positive control. The cells were fixed and stained by TRAP after 10 days. Results of this staining indicated that $MDSC^{(+bone\ mets)}$ stained positively for TRAP as evidence for osteoclast differentiation (Fig. 1A). However, $MDSC^{(+lung\ mets)}$ and $MDSC^{(-bone\ mets)}$ did not undergo osteoclast differentiation. MDSC were also isolated from the lymph nodes ($MDSC^{(Lymph\ Nodes)}$), spleen ($MDSC^{(Spleen)}$), and blood ($MDSC^{(Blood)}$) of tumor-bearing mice showing bone metastasis. Phenotypically, such MDSC were similar to $MDSC^{(+bone\ mets)}$ but failed to differentiate into osteoclasts, suggesting that the bone microenvironment is critical for osteoclast differentiation of MDSC (Supplementary Fig. S2).

Further, $MDSC^{(+bone\ mets)}$ expressed other osteoclast-specific markers, including cathepsin-K, carbonic anhydrase-2, and MMP-9, starting at day 4 of osteoclast differentiation (Fig. 1B). However, $MDSC^{(-bone\ mets)}$ did not express any of the osteoclast-specific markers. Because $MDSC^{(+bone\ mets)}$ differentiated into osteoclasts, expression of F4/80, which is a macrophage-specific marker, was detected by flow cytometry. As shown in Supplementary Fig. S3A, $MDSC^{(+bone\ mets)}$ did not express F4/80 during osteoclast differentiation, which showed that $MDSC^{(+bone\ mets)}$ did not differentiate into macrophages and, thus, were a true novel population of osteoclast progenitor.

MDSC-derived osteoclasts are functional and capable of bone resorption

Next, we sought to determine if MDSC-derived osteoclasts from bone metastasis are functional. A hallmark of functional osteoclasts is their ability to degrade bone *in vitro* and *in vivo* (22, 23). To determine if MDSC-derived osteoclasts were capable of degrading bone, a bone resorption assay was conducted. As shown in Fig. 2, osteoclasts differentiated from $MDSC^{(+bone\ mets)}$ were functional as they degraded bone, indicated by the presence of numerous resorption pits (Fig. 2). As expected, MDSC from control mice ($MDSC^{(control)}$) and $MDSC^{(-bone\ mets)}$ failed to resorb bone.

MDSC induce bone destruction *in vivo*

To corroborate the *in vitro* finding that $MDSC^{(+bone\ mets)}$ form functional osteoclasts, these MDSC were injected into the tibia of female BALB/c mice. Ten days later, femur and tibia were analyzed by micro-CT and histochemical staining for detecting bone destruction. Mice injected with $MDSC^{(+bone\ mets)}$ showed significantly more bone destruction compared with the PBS control on micro-CT imaging (Fig. 3A; Supplementary Fig. S3B). Histochemical analysis clearly showed increased osteoclast numbers by the TRAP assay (Fig. 3B&C; Supplementary Fig. S3B).

To confirm that injected MDSC differentiated into osteoclasts *in vivo* and caused bone destruction, a congeneic transfer was carried out wherein $MDSC^{(+bone\ mets)}$ from $CD45.2^{+}$ genotype mice were transferred into the tibia of non–

Published OnlineFirst December 14, 2012; DOI: 10.1158/0008-5472.CAN-12-2202

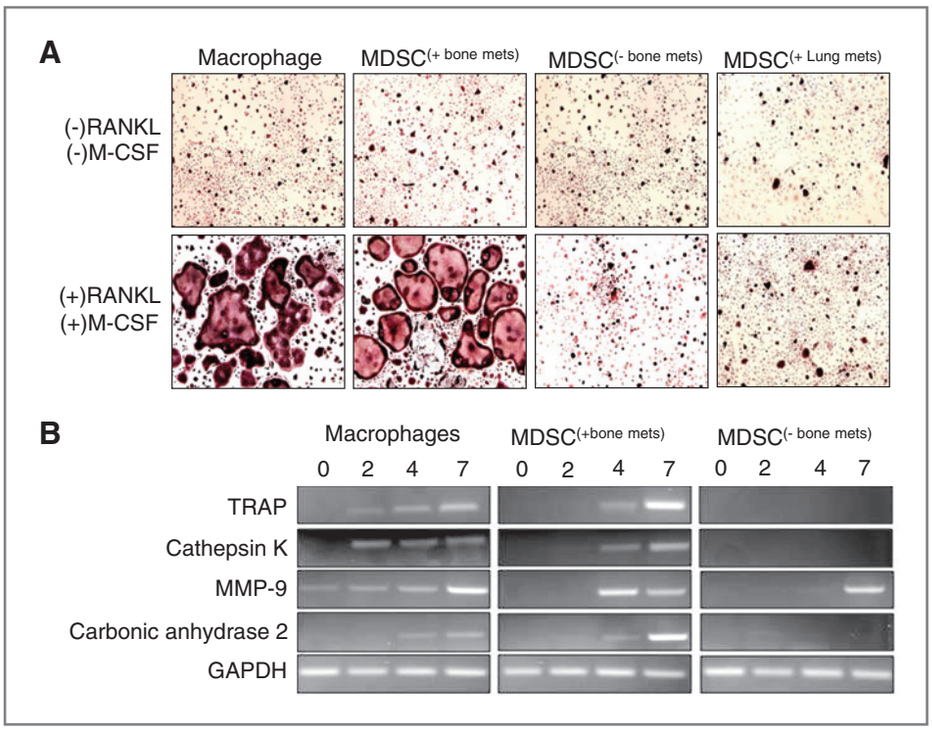

Figure 1. MDSC from bone metastasis are primed for osteoclast differentiation. A, $MDSC^{(+bone\ mets)}$, $MDSC^{(-bone\ mets)}$, and $MDSC^{(+lung\ mets)}$ were cultured in the presence of M-CSF and RANKL for osteoclast differentiation. Bone marrow-derived macrophages were used as a positive control. Presence of osteoclasts was detected by TRAP staining after 10 days. A representative image for each treatment group is shown ($n = 5$). A Leica DMI4000B microscope, attached to a Leica DFC500 digital camera, was used for obtaining images. B, bone marrow macrophages, $MDSC^{(+bone\ mets)}$, and $MDSC^{(-bone\ mets)}$ were differentiated into osteoclasts as mentioned in Materials and Methods. On days 2, 4, and 7 of differentiation, cells were collected and RNA was isolated. cDNA was synthesized and used to detect expression of TRAP, MMP-9, cathepsin K, and carbonic anhydrase-2 by semiquantitative PCR. All the experiments were repeated 3 times independently.

tumor-challenged congeneic $CD45.1^{+}$ mice. After 8 days, the presence of $MDSC^{(+bone\ mets)}$ was detected in injected tibia by CD45.2 labeling and these MDSC also expressed cathepsin K, an osteoclast marker, and differentiated into osteoclasts *in vivo* (Fig. 3D).

NO levels are elevated as MDSC differentiate into osteoclasts

The mechanisms by which MDSC promote immunosuppression are by increased arginase activity, reactive oxygen species (ROS), and/or NO production (2, 24, 25).

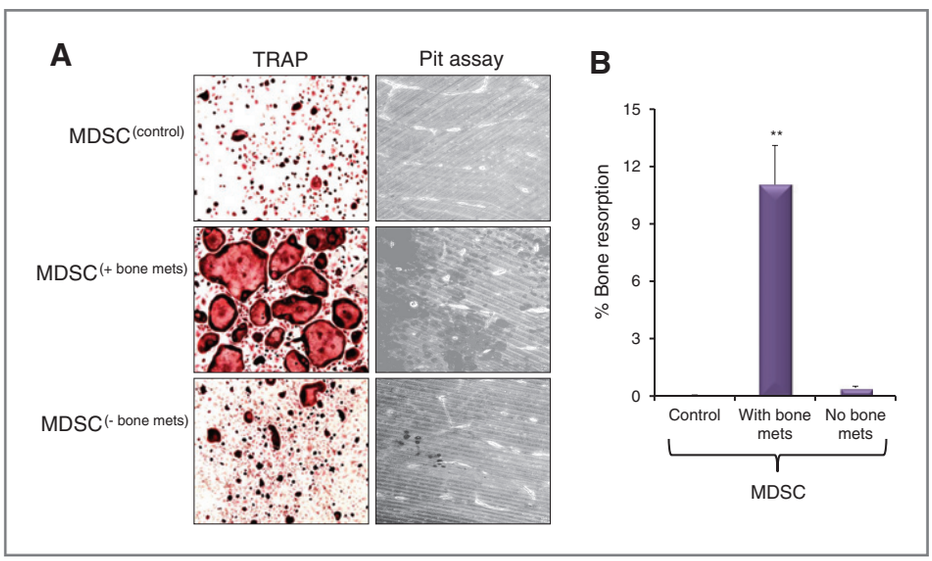

Figure 2. $MDSC^{(+bone\ mets)}$-derived osteoclasts are functional in bone resorption. A, $MDSC^{(control)}$, $MDSC^{(+bone\ mets)}$, and $MDSC^{(-bone\ mets)}$ were seeded on sterile porcine cortical bone slices (10^5 cells per slice). After 13 days of culture, presence of pits (resorption areas) was detected by using a Olympus FluorView 300 laser scanning confocal microscope. A representative image for each experimental group is presented. Experiments were repeated 3 times independently. B, percentage of resorption was calculated from the laser scanning confocal microscope images using Adobe Photoshop software. Results are representative of 3 independent experiments (**, $P < 0.001$).

Published OnlineFirst December 14, 2012; DOI: 10.1158/0008-5472.CAN-12-2202

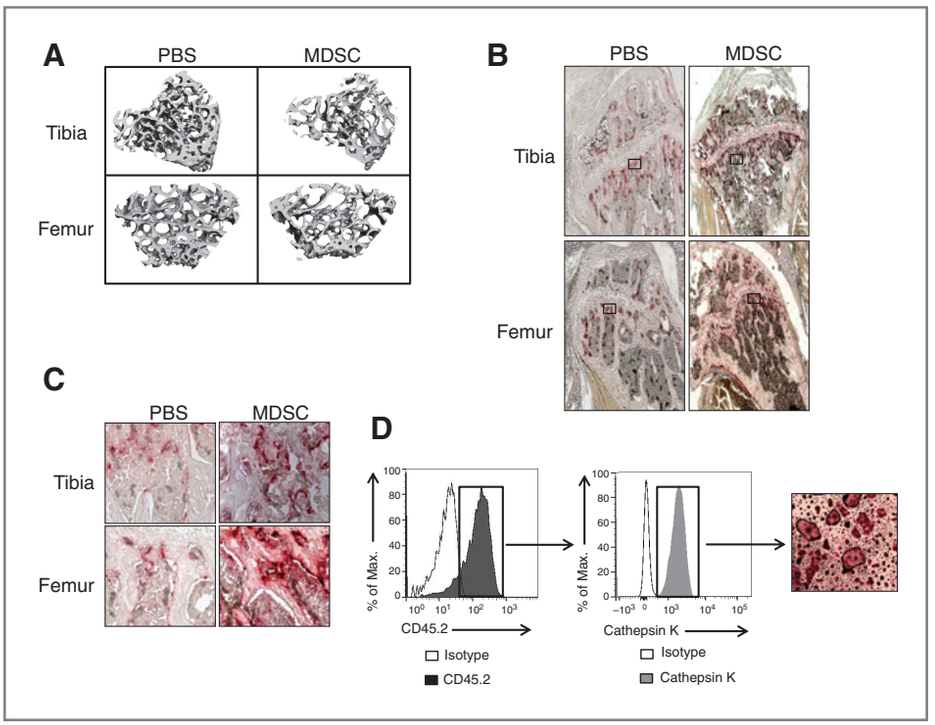

Figure 3. Syngeneic transplantation of MDSC from bone metastasis induces increased bone destruction in recipient mice *in vivo*. A, 2.5×10^5 MDSC from mice bearing bone metastasis were injected in the tibia of syngeneic, normal female mice on days 1 and 5. As a control, mice were injected with PBS. On day 10, mice were sacrificed and MDSC-injected tibia and adjacent femur were processed for micro-CT analysis to determine the extent of bone destruction. A representative image for each experimental group is shown ($n = 3$). Paraffin sections of the above femur and tibia were stained by TRAP to detect the presence of osteoclasts. Representative images of ×20 (B) and ×40 (C) magnifications are shown. Images were taken using a Leica DMI4000B microscope, attached to a Leica DFC500 digital camera. The LASv3.6.0 software was used to optimize picture quality. D, $MDSC^{(+bone\ mets)}$ from CD45.2 genotype BALB/c mice were injected into tibia of non–tumor-challenged CD45.1 congeneic BALB/c mice as described in Materials and Methods. On day 8, mice were sacrificed and bone marrow cells were collected from the MDSC-injected tibia and adjacent femur. Cells were stained with antibodies to CD45.2 and cathepsin k. Presence of $CD45.2^+$ cells, which also stained for cathepsin k, was sorted. Sorted cells were differentiated into osteoclasts as mentioned previously. A representative dataset showing presence of transferred $MDSC^{(+bone\ mets)}$ and differentiation into osteoclast is presented ($n = 3$).

To examine whether any of these mechanisms were involved in differentiation of MDSC into osteoclasts, arginase activity, ROS, and NO levels were measured at various stages of osteoclast differentiation of MDSC. Arginase activity and ROS levels remained unchanged (Fig. 4A–B; Supplementary Figs. S4 and S5). Further, the NO levels were greatly elevated only in $MDSC^{(+bone\ mets)}$ and not in $MDSC^{(control)}$, $MDSC^{(-bone\ mets)}$, $MDSC^{(Lymph\ Nodes)}$, $MDSC^{(Lungs)}$, $MDSC^{(Blood)}$, and $MDSC^{(Spleen)}$ as these MDSC differentiated into osteoclasts (Figs. 4C and D, 5A; Supplementary Figs. S4 and S5), thus showing a possible role for NO in inducing osteoclast differentiation of $MDSC^{(+bone\ mets)}$.

NO is essential for differentiation of MDSC into osteoclasts

Next, to determine that NO is essential for osteoclast differentiation of $MDSC^{(+bone\ mets)}$, these cells were cultured in RANKL and M-CSF in the presence of L-NMMA, which is a specific inhibitor of inducible nitric oxide synthase (iNOS; ref. 15). Results clearly showed that $MDSC^{(+bone\ mets)}$ failed to differentiate into osteoclasts in the presence of 25 μmol/L L-NMMA, showing that NO production is crucial for the differentiation of $MDSC^{(+bone\ mets)}$ into the osteoclasts (Fig. 5B and C).

Further, to delineate a pivotal role of NO in the differentiation of $MDSC^{(+bone\ mets)}$ into osteoclasts, before *in vivo* transfer of $MDSC^{(+bone\ mets)}$, mice were injected with 1400W, a specific iNOS inhibitor, intraperitoneally. Treatment with 1400W was continued until the end of the experiment, at which point mice were sacrificed to collect MDSC-injected long-bones for micro-CT analysis. Data clearly showed reduced bone damage in the bone of mice injected with 1400W together with $MDSC^{(+bone\ mets)}$, signifying the importance of NO in MDSC-mediated bone damage *in vivo* (Supplementary Fig. S6).

NO elevation is accompanied with increased activation of PI3 kinase, ERK, and hypoxia-inducible factor-1α

Because elevation of NO was specific to $MDSC^{(+bone\ mets)}$, which differentiated into osteoclasts, we then investigated the pathways that might contribute to high NO production in $MDSC^{+bone\ mets}$. Hypoxia-inducible factor-1 (HIF-1α) is known to be upregulated in MDSC in the tumor microenvironment (26). Considering the hypoxic tumor microenvironment of the bone, we hypothesized that these MDSC may have elevated HIF-1α levels. In addition, NO levels are elevated in

Published OnlineFirst December 14, 2012; DOI: 10.1158/0008-5472.CAN-12-2202

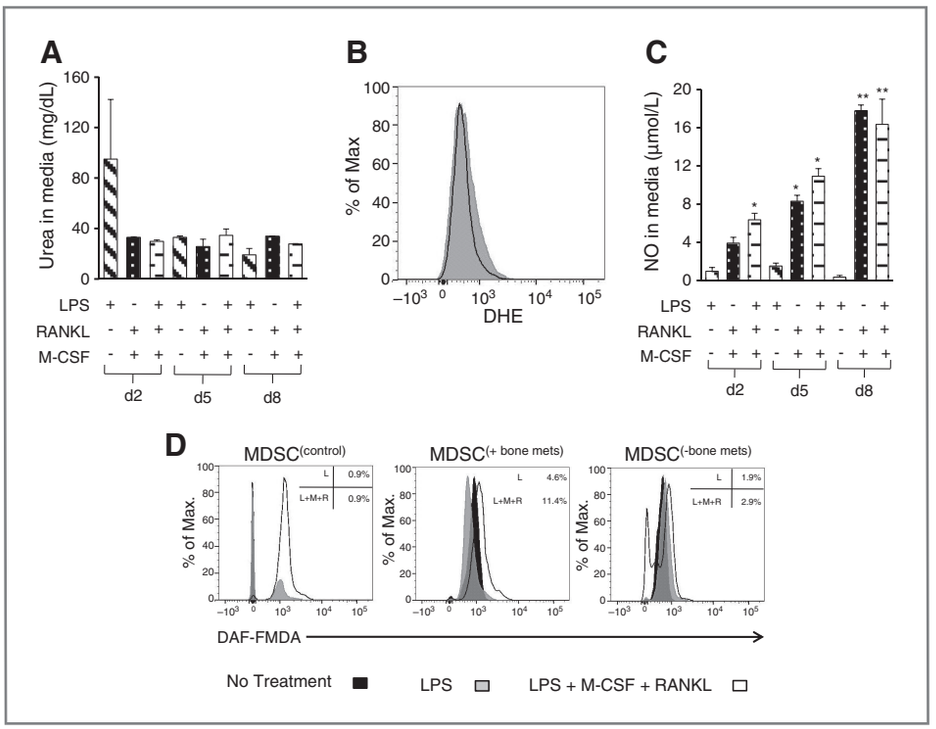

Figure 4. Nitric oxide levels are elevated in MDSC$^{(+\text{bone mets})}$ during osteoclast differentiation. MDSC, derived from the bone marrow of tumor-bearing mice, were cultured in the presence of M-CSF and RANKL with or without LPS. On days 2, 5, and 8 of differentiation, culture supernatants were collected to assay arginase levels and NO levels. Quantitative differences in arginase level as measured by urea production are provided (A). Levels of ROS were detected by flow cytometry by incubating MDSC$^{(+\text{bone mets})}$ for 20 minutes at RT with dihydroxyethidium after 5 days of culture in osteoclast differentiation medium (B). Culture supernatants were also used to detect NO levels by Griess assay (C). MDSC$^{(\text{control})}$, MDSC$^{(+\text{bone mets})}$, and MDSC$^{(-\text{bone mets})}$ were differentiated into osteoclasts in M-CSF and RANKL-containing medium with or without LPS. Five days after differentiation, levels of NO were detected by the addition of DAF-FMDA. Flow cytometry was used to quantify NO levels. A representative histogram is shown together with the percentage of cells with increased NO content. All the experiments were repeated 5 times independently (*, $P < 0.05$; **, $P < 0.001$].

MDSC under hypoxia (26). As shown in Fig. 6A, HIF-1α levels decreased on treatment of MDSC$^{(+\text{bone mets})}$ with L-NMMA. HIF-1α levels were higher in MDSC$^{(+\text{bone mets})}$ compared with MDSC$^{(-\text{bone mets})}$ (Fig. 6B). NO can further induce HIF-1α via signaling through PI3 kinase or ERK or Akt (27). MDSC$^{(+\text{bone mets})}$ also showed elevated levels of phosphorylated PI3 kinase and ERK (Fig. 6C). As expected, low levels of phosphorylated PI3 kinase and ERK were detected in MDSC$^{(\text{Lymph Nodes})}$, MDSC$^{(\text{Lungs})}$, MDSC$^{(\text{Blood})}$, and MDSC$^{(\text{Spleen})}$ (Supplementary Fig. S7).

Taken together, this study clearly shows that MDSC, in the bone microenvironment with disseminated tumor, are novel osteoclast progenitors which contribute to osteolysis of breast cancer. Further, studies delineate a NO-dependent mechanism that drives MDSC differentiation into osteoclasts in the bone microenvironment via the HIF-1α signaling pathway. Thus, targeting MDSC in breast cancer patients will not only reduce tumor growth but also lower the growth of breast cancer in the bone.

Discussion

The present study elucidates a novel role for MDSC as osteoclast progenitors in breast cancer. Importantly, the finding that only MDSC from the bone microenvironment with disseminated breast cancer were capable of undergoing osteoclast differentiation suggests the importance of interaction of MDSC with other cells, including cancer cells, and the reactive stroma that might induce appropriate stimuli for osteoclastogenesis. Although results of the current study delineating the role of MDSC as osteoclast progenitor are from using a breast cancer model, these findings can be also extended to other osteolytic carcinomas such as lung and multiple myeloma that predominantly metastasize to bone.

MDSC constitute approximaytely1 30% of cells in the bone marrow of normal mice (13). However, following bone metastasis of breast cancer, MDSC numbers are elevated not only at the primary tumor site, but also at metastatic sites including lung, liver, and bone. It is very interesting from the results of the present study that only resident MDSC isolated from the bone microenvironment following cancer dissemination can become osteoclasts. Studies to understand possible mechanisms that might have triggered the differentiation of bone-derived MDSC into osteoclasts indicated the significance of NO signaling.

It is likely that increased hypoxia in the bone, on tumor growth, triggers osteoclast differentiation of MDSC. Hypoxia and HIF-1α expression have been known to enhance osteolytic bone metastases of breast cancer by promoting

Published OnlineFirst December 14, 2012; DOI: 10.1158/0008-5472.CAN-12-2202

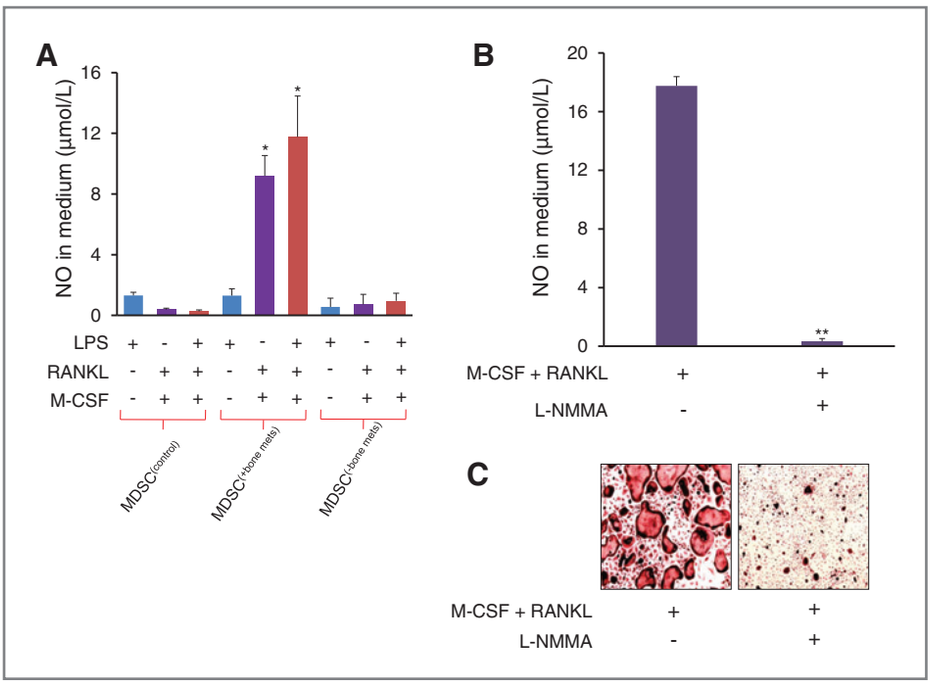

Figure 5. Nitric oxide is essential for differentiation of MDSC$^{(+\text{bone mets})}$ into osteoclasts. A, nitric oxide levels were detected on day 8 in MDSC$^{(\text{control})}$, MDSC$^{(+\text{bone mets})}$, and MDSC$^{(-\text{bone mets})}$ as they differentiated into osteoclasts. Representative data from 3 independent experiments is presented ($n = 3$; *, $P < 0.05$). B, MDSC$^{(+\text{bone mets})}$ were differentiated into osteoclasts in the presence of L-NMMA. Griess assay was carried out to detect NO levels. Data are representative of 3 different experiments ($n = 3$; **, $P < 0.001$). C, MDSC$^{(+\text{bone mets})}$ were differentiated into osteoclasts in the presence of L-NMMA and presence of osteoclasts was detected by TRAP assay ($n = 3$).

osteoclastogenesis (28). As described previously, HIF-1α stimulates and regulates osteoclasts (29, 30). In line with these reports, the present study clearly shows that HIF-1α levels are dramatically increased specifically only in MDSC$^{(+\text{bone mets})}$ and this is the only MDSC population that differentiated into osteoclasts. Interestingly, HIF-1α also induces NO production via iNOS (26), which again was found to be elevated in MDSC$^{(+\text{bone mets})}$ only. Studies have shown that NO induces HIF-1α activation via MAPK and PI3 kinase signaling pathway

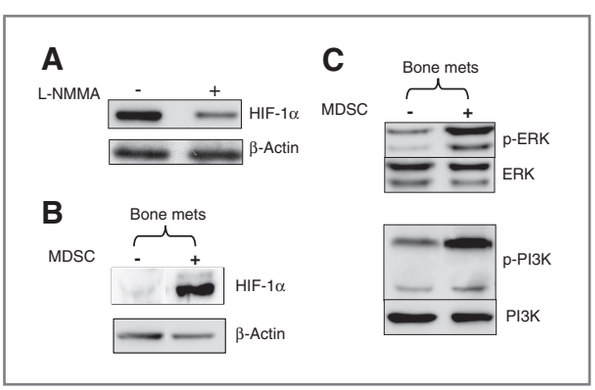

Figure 6. MDSC$^{(+\text{bone mets})}$-derived osteoclasts have elevated HIF-1α, ERK, and PI3 kinase pathways. MDSC$^{(+\text{bone mets})}$ and MDSC$^{(-\text{bone mets})}$ were isolated from tumor-bearing mice and cultured in the presence or absence of L-NMMA for 4 days, following which, cell lysates were prepared. Presence of HIF-1α was detected by Western blot as mentioned in Materials and Methods (A). MDSC$^{(+\text{bone mets})}$ and MDSC$^{(-\text{bone mets})}$ were isolated from tumor-bearing mice and cell lysates were prepared. Lysates containing equal amounts of total protein were separated on SDS-PAGE and transferred onto nitrocellulose membranes. Detection of HIF-1α (B), ERK, PI3 kinase, and β-actin (C) were carried out as described in Materials and Methods ($n = 3$).

(27, 31) and further analysis of bone-derived MDSC following cancer dissemination revealed that PI3 kinase levels are elevated during osteoclast differentiation of MDSC. L-NMMA treatment of MDSC$^{(+\text{bone mets})}$ not only reduced the NO levels in these MDSC but also drastically reduced the HIF-1 α levels. Thus, it is likely that increased HIF-1α levels, combined with elevated NO levels in MDSC, promote osteoclast differentiation of MDSC$^{(+\text{bone mets})}$.

Involvement of NO in osteoclast differentiation of MDSC$^{(+\text{bone mets})}$ was further confirmed by using a specific iNOS inhibitor. NO is known to induce osteoclast differentiation of macrophages (32, 33). In the present study, very high levels of NO were observed as macrophages differentiated into osteoclasts (data not shown). BMMs from mice lacking iNOS showed reduced osteoclast formation and bone resorption (33, 34). Inhibition of NO levels in wild-type (WT) mice using iNOS inhibitors also showed reduced osteoclast potential of BMMs. These observations further corroborate the findings in the present study.

MDSC from tumor-bearing mice with bone metastasis also induced osteolysis *in vivo* in syngeneic mice. This further indicates that these cells are primed to be osteoclast progenitors and the bone microenvironment *in vivo* triggers their differentiation into functional osteoclasts. Increased osteolysis in MDSC$^{(+\text{bone mets})}$-injected mice was the result of increased osteoclast numbers. It was interesting that the femur, adjacent to the MDSC-injected tibia, also showed significant amount of bone destruction. One of the possibilities is that the MDSC-generated osteoclasts could migrate to the neighboring femur and induce osteolysis. MMP-9 is critical for osteoclast migration (35, 36). Our data indicated that as MDSC$^{(+\text{bone mets})}$ differentiate into osteoclasts, they express MMP-9, and this may contribute to their migration *in vivo*. By congeneic transfer

Published OnlineFirst December 14, 2012; DOI: 10.1158/0008-5472.CAN-12-2202

of MDSC$^{(+\text{bone mets})}$, it was clear that transferred MDSC remained confined in injected tibia and did not migrate to the adjacent femur (data not shown). Therefore, there is a strong possibility that the observed bone destruction in the adjacent femur may be due to MDSC$^{(+\text{bone mets})}$-secreted growth factors such as interleukin 1 (IL-1), IL-6, M-CSF, which may further stimulate endogenous macrophages in the bone microenvironment to differentiate into osteoclasts. On the basis of these observations, it may be anticipated that in the bone carrying metastasized tumor, infiltration of MDSC would function in a dual capacity; first, MDSC can directly contribute to osteolysis by differentiating into osteoclasts and, secondly, MDSC-produced cytokines can induce endogenous osteoclast progenitors to induce bone damage.

It is clear from the current study that a cross-talk among MDSC, tumor cells, and the bone microenvironment is necessary for MDSC differentiation into osteoclasts. It remains possible that soluble factors secreted by tumor cells in the bone 'prime' these MDSC as osteoclast progenitors. Approximately 83% of breast tumors metastasized to bone express osteopontin (OPN), which contributes to osteolysis by inducing expression of cathepsin K and MMP-9 that are essential for osteoclast function (37). 4T1 cells used in this study have been known to express OPN (38). In addition, breast cancer cells metastasized to the bone also secrete various chemokines such as MCP-1 and RANTES, which are known to enhance osteoclastogenesis (39). Interestingly, MCP-1 can induce NO secretion, a molecular mediator that is essential for osteoclast differentiation of MDSC$^{(+\text{bone mets})}$ (40). MDSC express CCR-2, which is a receptor for MCP-1, and thus are responsive to this chemokine (41). Elevated levels of both MCP-1 and RANTES were observed in the 4T1 breast cancer model as cancer metastasizes to bone, which corroborated with published reports (data not shown). Therefore, the presence of such pro-osteolytic factors may induce differentiation of MDSC$^{(+\text{bone mets})}$ into osteoclasts.

Noting that MDSC are novel osteoclast progenitors, it will be interesting to investigate further the potential of MDSC from the breast cancer patients to induce osteolysis. Ongoing studies are focused on obtaining peripheral MDSC from breast cancer patients with bone metastasis, with further studies planned with MDSC from the bone marrow aspirates of these patients.

Overall, the present study gives a new impetus to the role of MDSC in tumor progression, especially for carcinomas with a propensity to metastasize to the bone. It will also allow designing better treatment regimen for patients with breast cancer bone pathology. For example, gemcitabine, a commonly used chemotherapy agent for breast and lung carcinomas (42–44) is also known to specifically inhibit MDSC (18, 45). Thus, gemcitabine may be used not only as an antitumorigenic drug, but also for reducing bone destruction. Indeed, our *in vivo* study showed that gemcitabine-treated mice not only had lesser MDSC, but also the tumor growth in the bone was reduced (Supplementary Fig. S8). Further, bisphosphonates are commonly used for breast cancer patients with bone metastasis (46, 47). Interestingly, bisphosphonates also inhibit MDSC (8). In the context with the present study, it is relevant to speculate that bisphosphonates, besides inhibiting tumor angiogenesis and inducing apoptosis, can also directly reduce osteolysis by inhibiting MDSC, which are novel osteoclast progenitors.

In summary, the findings presented here provide a novel role for MDSC as cells capable of differentiating into functional, bone-resorbing osteoclasts that contribute to aggressive osteolysis. For long, this population of myeloid cells was thought of as being an immunosuppressive population. Evidence from this study further adds an intriguing multifaceted role for MDSC in cancer bone pathology.

Disclosure of Potential Conflicts of Interest

No potential conflicts of interest were disclosed.

Authors' Contributions

Conception and design: A. Sawant, S. Ponnazhagan
Development of methodology: A. Sawant, J. Jules, C. Lee, S. Ponnazhagan
Acquisition of data (provided animals, acquired and managed patients, provided facilities, etc.): A. Sawant, X. Feng, S. Ponnazhagan
Analysis and interpretation of data (e.g., statistical analysis, biostatistics, computational analysis): A. Sawant, J. Deshane, S. Ponnazhagan
Writing, review, and/or revision of the manuscript: A. Sawant, J. Deshane, S. Ponnazhagan
Administrative, technical, or material support (i.e., reporting or organizing data, constructing databases): J. Jules, B. Harris, S. Ponnazhagan
Study supervision: S. Ponnazhagan

Acknowledgments

Noninvasive imaging was carried out at the UAB's Small Animal Imaging. Bone histomorphometry and micro-CT analyses were carried out in the UAB Bone Histomorphometry Core and Small Animal Bone Phenotyping Core, respectively. The authors thank Enid Keyser for technical assistance in flow cytometry and sorting and the Analytical and Preparative Cytometry Facility of the Comprehensive Arthritis, Musculoskeletal and Autoimmunity Center at UAB. Flow cytometric analysis was carried out in the UAB-CFAR Core facility.

Grant Support

This study was financially supported by the NIH grants AR050251, AR560948, CA132077, CA133737, P30 AR046031, and P30 AR48311 as well as DoD grant DoD-BC101411.

The costs of publication of this article were defrayed in part by the payment of page charges. This article must therefore be hereby marked *advertisement* in accordance with 18 U.S.C. Section 1734 solely to indicate this fact.

Received June 6, 2012; revised October 5, 2012; accepted November 10, 2012; published OnlineFirst December 14, 2012.

References

1. Gabrilovich DI, Ostrand-Rosenberg S, Bronte V. Coordinated regulation of myeloid cells by tumours. Nat Rev Immunol 2012;12:253–268.
2. Ostrand-Rosenberg SSP. Myeloid-derived suppressor cells: linking inflammation and cancer. J Immunol 2009;182:4499–506.
3. Nagaraj S, Gabrilovich DI. Myeloid-derived suppressor cells in human cancer. Cancer J 2010;16:348–53.
4. Ostrand-Rosenberg S. Myeloid-derived suppressor cells: more mechanisms for inhibiting antitumor immunity. Cancer Immunol Immunother 2010;59:1593–600.
5. Tadmor T, Attias D, Polliack A. Myeloid-derived suppressor cells–their role in haemato-oncological malignancies and other cancers and possible implications for therapy. Br J Haematol 2011;153:557–67.

Published OnlineFirst December 14, 2012; DOI: 10.1158/0008-5472.CAN-12-2202

6. Morales JK, Kmieciak M, Graham L, Feldmesser M, Bear HD, Manjili M H. Adoptive transfer of HER2/neu-specific T cells expanded with alternating gamma chain cytokines mediate tumor regression when combined with the depletion of myeloid-derived suppressor cells. Cancer Immunol Immunother 2009; 58:941–53.
7. Young MR, Young ME, Wepsic HT. Effect of prostaglandin E2-producing nonmetastatic Lewis lung carcinoma cells on the migration of prostaglandin E2-responsive metastatic Lewis lung carcinoma cells. Cancer Res 1987;47:3679–83.
8. Melani C, Sangaletti S, Barazzetta FM, Werb Z, Colombo MP. Amino-biphosphonate-mediated MMP-9 inhibition breaks the tumor–bone marrow axis responsible for myeloid-derived suppressor cell expansion and macrophage infiltration in tumor stroma. Cancer Res 2007; 67:11438–46.
9. Coleman RE. Metastatic bone disease: clinical features, pathophysiology and treatment strategies. Cancer Treat Rev 2001;27: 165–76.
10. Coleman RE, Rubens RD. 3(Amino-1,1-hydroxypropylidene) bisphosphonate (APD) for hypercalcaemia of breast cancer. Br J Cancer 1987;56:465–9.
11. Roodman GD. Mechanisms of bone metastasis. N Engl J Med 2004;350:1655–64.
12. Udagawa N, Takahashi N, Akatsu T, Tanaka H, Sasaki T, Nishihara T, et al. Origin of osteoclasts: mature monocytes and macrophages are capable of differentiating into osteoclasts under a suitable microenvironment prepared by bone marrow-derived stromal cells. Proc Natl Acad Sci U S A 1990;87:7260–64.
13. Gabrilovich DI, Nagaraj S. Myeloid-derived suppressor cells as regulators of the immune system. Nat Rev Immunol 2009;9: 162–74.
14. Jules J, Shi Z, Liu J, Xu D, Wang S, Feng X. Receptor activator of NF-{kappa}B (RANK) cytoplasmic IVVY535-538 motif plays an essential role in tumor necrosis factor-{alpha} (TNF)-mediated osteoclastogenesis. J Biol Chem 2010;285:37427–35.
15. Jia W, Jackson-Cook C, Graf MR. Tumor-infiltrating, myeloid-derived suppressor cells inhibit T cell activity by nitric oxide production in an intracranial rat glioma + vaccination model. J Neuroimmunol 2010; 223:20–30.
16. Erlebacher A, Derynck R. Increased expression of TGF-beta 2 in osteoblasts results in an osteoporosis-like phenotype. J Cell Biol 1996;132:195–210.
17. Sinha P, Clements VK, Bunt SK, Albelda SM, Ostrand-Rosenberg S. Cross-talk between myeloid-derived suppressor cells and macrophages subverts tumor immunity toward a type 2 response. J Immunol 2007;179:977–83.
18. Suzuki E, Kapoor V, Jassar AS, Kaiser LR, Albelda SM. Gemcitabine selectively eliminates splenic Gr-1+/CD11b+ myeloid suppressor cells in tumor-bearing animals and enhances antitumor immune activity. Clin Cancer Res 2005;11:6713–21.
19. Parfitt AM, Simon LS, Villanueva AR, Krane SM. Procollagen type I carboxy-terminal extension peptide in serum as a marker of collagen biosynthesis in bone. Correlation with iliac bone formation rates and comparison with total alkaline phosphatase. J Bone Miner Res 1987;2:427–36.
20. Anderson JT, Zeng M, Li Q, Stapley R, Moore DR 2nd, Chenna B, et al. Elevated levels of NO are localized to distal airways in asthma. Free Radic Biol Med 2011;50:1679–88.
21. Deshane J, Zmijewski JW, Luther R, Gaggar A, Deshane R, Lai JF, et al. Free radical-producing myeloid-derived regulatory cells: potent activators and suppressors of lung inflammation and airway hyperresponsiveness. Mucosal Immunol 2011;4: 503–18.
22. Ashley JW, Shi Z, Zhao H, Li X, Kesterson RA, Feng X. Genetic ablation of CD68 results in mice with increased bone and dysfunctional osteoclasts. Plos One 2011;6:e25838.
23. Hsu YC, Cheng CP, Chang DM. *Plectranthus amboinicus* attenuates inflammatory bone erosion in mice with collagen-induced arthritis by downregulation of RANKL-induced NFATc1 expression. J Rheumatol 2011;38:1844–57.
24. Youn JIGD. The biology of myeloid-derived suppressor cells: the blessing and the curse of morphological and functional heterogeneity. Eur J Immunol 2010;40:2969–75.
25. Peranzoni EZS, Marigo I, Dolcetti L, Zanovello P, Mandruzzato S, Bronte V. Myeloid-derived suppressor cell heterogeneity and subset definition. Curr Opinion Immunol 2010;22:238–44.
26. Corzo CA, Condamine T, Lu L, Cotter MJ, Youn JI, Cheng P, et al. HIF-1alpha regulates function and differentiation of myeloid-derived suppressor cells in the tumor microenvironment. J Exp Med 2010;207: 2439–53.
27. Kasuno K, Takabuchi S, Fukuda K, Kizaka-Kondoh S, Yodoi J, Adachi T, et al. Nitric oxide induces hypoxia-inducible factor 1 activation that is dependent on MAPK and phosphatidylinositol 3-kinase signaling. J Biol Chem 2004;279:2550–8.
28. Hiraga T, Kizaka-Kondoh S, Hirota K, Hiraoka M, Yoneda T. Hypoxia and hypoxia-inducible factor-1 expression enhance osteolytic bone metastases of breast cancer. Cancer Res 2007; 67:4157–63.
29. Knowles HJ, Athanasou NA. Acute hypoxia and osteoclast activity: a balance between enhanced resorption and increased apoptosis. J Pathol 2009;218:256–64.
30. Knowles HJ, Cleton-Jansen AM, Korsching E, Athanasou NA. Hypoxia-inducible factor regulates osteoclast-mediated bone resorption: role of angiopoietin-like 4. Faseb J 2010;24:4648–59.
31. Sheta EA, Trout H, Gildea JJ, Harding MA, Theodorescu D. Cell density mediated pericellular hypoxia leads to induction of HIF-1alpha via nitric oxide and Ras/MAP kinase mediated signaling pathways. Oncogene 2001;20:7624–34.
32. Nilforoushan DGA, Glogauer M, Manolson MF. Nitric oxide enhances osteoclastogenesis possibly by mediating cell fusion. Nitric Oxide 2009;21:27–36.
33. Herrera BSM-PR, Maia-Dantas A, Campi P, Spolidorio LC, Costa SK, Van Dyke TE, et al. iNOS-derived nitric oxide stimulates osteoclast activity and alveolar bone loss in ligature-induced periodontitis in rats. J Periodontol 2011;82:1608–15.
34. Gyurko RSH, Battaglino RA, Boustany G, Gibson FC 3rd, Genco CA, Stashenko P, et al. Inducible nitric oxide synthase mediates bone development and *P. gingivalis*-induced alveolar bone loss. Bone 2005; 36:472–9.
35. Blavier L, Delaisse JM. Matrix metalloproteinases are obligatory for the migration of preosteoclasts to the developing marrow cavity of primitive long bones. J Cell Sci 1995;108 (Pt 12):3649–59.
36. Sato T, Foged NT, Delaisse JM. The migration of purified osteoclasts through collagen is inhibited by matrix metalloproteinase inhibitors. J Bone Miner Res 1998;13:59–66.
37. Das S, Samant RS, Shevde LA. Hedgehog signaling induced by breast cancer cells promotes osteoclastogenesis and osteolysis. J Biol Chem 2011;286:9612–22.
38. Mi Z, Guo H, Wai PY, Gao C, Wei J, Kuo PC. Differential osteopontin expression in phenotypically distinct subclones of murine breast cancer cells mediates metastatic behavior. J Biol Chem 2004;279: 46659–67.
39. Soria G, Ben-Baruch A. The inflammatory chemokines CCL2 and CCL5 in breast cancer. Cancer Lett 2008;267:271–85.
40. Skuljec J, Sun H, Pul R, Benardais K, Ragancokova D, Moharregh-Khiabani D, et al. CCL5 induces a pro-inflammatory profile in microglia *in vitro*. Cell Immunol 2011;270:164–71.
41. Huang B, Lei Z, Zhao J, Gong W, Liu J, Chen Z, et al. CCL2/CCR2 pathway mediates recruitment of myeloid suppressor cells to cancers. Cancer Lett 2007;252:86–92.
42. Loesch D, Asmar L, McIntyre K, Doane L, Monticelli M, Paul D, et al. Phase II trial of gemcitabine/carboplatin (plus trastuzumab in HER2-positive disease) in patients with metastatic breast cancer. Clin Breast Cancer 2008;8:178–86.
43. Brito LG, de Andrade JM, Lins-Almeida T, Zola FE, Pinheiro MN, Marana HR, et al. Safety and efficacy of gemcitabine plus cisplatin combination in pretreated metastatic breast cancer patients. Med Oncol 2012;29:33–8.
44. Chun SH, Lee JE, Park MH, Kang JH, Kim YK, Wang YP, et al. Gemcitabine plus platinum combination chemotherapy for elderly

Published OnlineFirst December 14, 2012; DOI: 10.1158/0008-5472.CAN-12-2202

patients with advanced non-small cell lung cancer: a retrospective analysis. Cancer Res Treat 2011;43:217–24.

45. Le HK, Graham L, Cha E, Morales JK, Manjili MH, Bear HD. Gemcitabine directly inhibits myeloid derived suppressor cells in BALB/c mice bearing 4T1 mammary carcinoma and augments expansion of T cells from tumor-bearing mice. Int Immunopharmacol 2009;9:900–9.

46. Gnant M, Dubsky P, Hadji P. Bisphosphonates: prevention of bone metastases in breast cancer. Recent Results Cancer Res 2012;192:65–91.

47. Monsees GM, Malone KE, Tang MT, Newcomb PA, Li CI. Bisphosphonate use after estrogen receptor-positive breast cancer and risk of contralateral breast cancer. J Natl Cancer Inst 2011;103:1752–60.

Published OnlineFirst December 14, 2012; DOI: 10.1158/0008-5472.CAN-12-2202

Cancer Research
The Journal of Cancer Research (1916–1930) | The American Journal of Cancer (1931–1940)

AACR American Association for Cancer Research

Myeloid-Derived Suppressor Cells Function as Novel Osteoclast Progenitors Enhancing Bone Loss in Breast Cancer

Anandi Sawant, Jessy Deshane, Joel Jules, et al.

Cancer Res 2013;73:672-682. Published OnlineFirst December 14, 2012.

OncoImmunology 2:5, e24064; May 2013; © 2013 Landes Bioscience

Myeloid-derived suppressor cells as a novel target for the control of osteolytic bone disease

Anandi Sawant and Selvarangan Ponnazhagan*

Department of Pathology; University of Alabama at Birmingham; Birmingham, AL USA

Keywords: bone metastasis, breast cancer, myeloid-derived suppressor cells, osteoclasts

Myeloid-derived suppressor cells (MDSCs) from mice bearing bone metastases differentiate into functional osteoclasts in vitro and in vivo, through a signaling pathway that relies on nitric oxide. In addition, MDSC-targeting drugs have been shown to robustly inhibit osteolysis. Thus, MDSCs stand out as novel osteoclast progenitors and hence as candidate targets for the control of osteolytic bone disease.

Myeloid-derived suppressor cells (MDSC) constitute a major immunosuppressive cell population that has been correlated with poor prognosis in multiple neoplasms. MDSC are a heterogeneous population of myeloid precursors that fail to undergo maturation. MDSC exert immunosuppressive effects through a variety of mechanisms, many of which are mediated by the upregulation of arginase 1 and production of reactive oxygen and nitrogen species (ROS and RNS, respectively).[1]

In healthy individuals, MDSC constitute about 0.5% of peripheral blood mononuclear cells. In patients at early stages of neoplastic diseases, this proportion can increase by more than 5-fold.[2] About 30% of cells in the bone marrow (BM) of normal mice can be considered as MDSC. Following the metastatic spread of experimental cancers to the bone, the amount of MDSC increases by 2–3-fold, promoting local immunosuppression and hence allowing for the growth of metastatic cells. Considering such a high influx of MDSC to the bone, we hypothesized that MDSC may contribute to metastasis in more than one way. Hence, we investigated if MDSC directly contribute to osteolysis by differentiating into osteoclasts.

Using a pre-clinical model of breast cancer (BCa) bone dissemination, we demonstrated that MDSC can function as osteoclast precursors.[3] MDSC isolated from mice bearing bone metastases underwent osteoclast differentiation in vitro in the presence of receptor activator of nuclear factor-κB ligand (RANKL) and macrophage colony-stimulating factor (M-CSF). In addition, MDSC gave rise to bone-resorbing osteoclasts, causing increased osteolysis in vivo. As MDSC exert immunosuppression via arginase 1-, ROS- and RNS-dependent pathways, we investigated if any of these mechanisms would also be involved in the differentiation of MDSC into osteoclasts. Our data indicated a possible role of nitric oxide (NO) signaling in the differentiation of bone-derived MDSC into osteoclasts (**Fig. 1**).[3]

The role of MDSC as osteoclast progenitors in BCa was also demonstrated in an independent study by Danilin et al.[4] This study indicated MDSC as osteoclast precursors using the human BCa cell line MDA-MB-231. MDA-MB-231 cells cultured with tumor-derived MDSCs express high levels of GLI family zinc finger 2 (GLI2)- and parathyroid hormone-like hormone (PTHLH)-coding mRNAs. Both these factors are important in osteoclast activation and in the induction of osteolysis. MDSC-mediated osteolysis was also observed in multiple myeloma (MM).[5] Thus, using a murine syngenic MM model, Zhuang et al. demonstrated that MDSC are capable of mediating bone resorption in vitro and in vivo. Both BCa and MM metastases are characterized by increased MDSC infiltration as neoplastic cells grow in the bone, and both these carcinomas are associated with osteolytic bone lesions. Osteolysis is a prominent feature of metastatic cancer as well as of rheumatoid arthritis (RA). MDSC isolated from a murine RA model also functioned as primary osteoclast progenitors and were capable of differentiating into functional osteoclasts in a NO-dependent fashion.[6]

One of the major findings of our study is that only MDSC obtained from the bone microenvironment of tumor-bearing mice can undergo osteoclast differentiation. Thus, neither MDSC from other metastatic sites nor MDSC from the bone of tumor-bearing mice devoid of bone metastases differentiated into osteoclasts. Similar observations were also reported by Danilin et al.[4] and Zhuang et al.[5] Hence, it is clear that a cross-talk between MDSC, tumor cells and the bone microenvironment is necessary for the differentiation of MDSC into osteoclasts. MDSC from mice bearing bone metastases also induced osteolysis in syngenic animals, indicating that these cells are primed as osteoclast progenitors and that the bone microenvironment triggers their differentiation into functional osteoclasts in vivo. It is possible that soluble factors secreted by tumor cells in the bone "prime" these cells to be osteoclast progenitors. BCa

*Correspondence to: Selvarangan Ponnazhagan; Email: pons@uab.edu
Submitted: 02/13/13; Accepted: 02/21/13
Citation: Sawant A, Ponnazhagan S. Myeloid-derived suppressor cells as a novel target for the control of osteolytic bone disease. OncoImmunology 2013; 2:e24064; http://dx.doi.org/10.4161/onci.24064

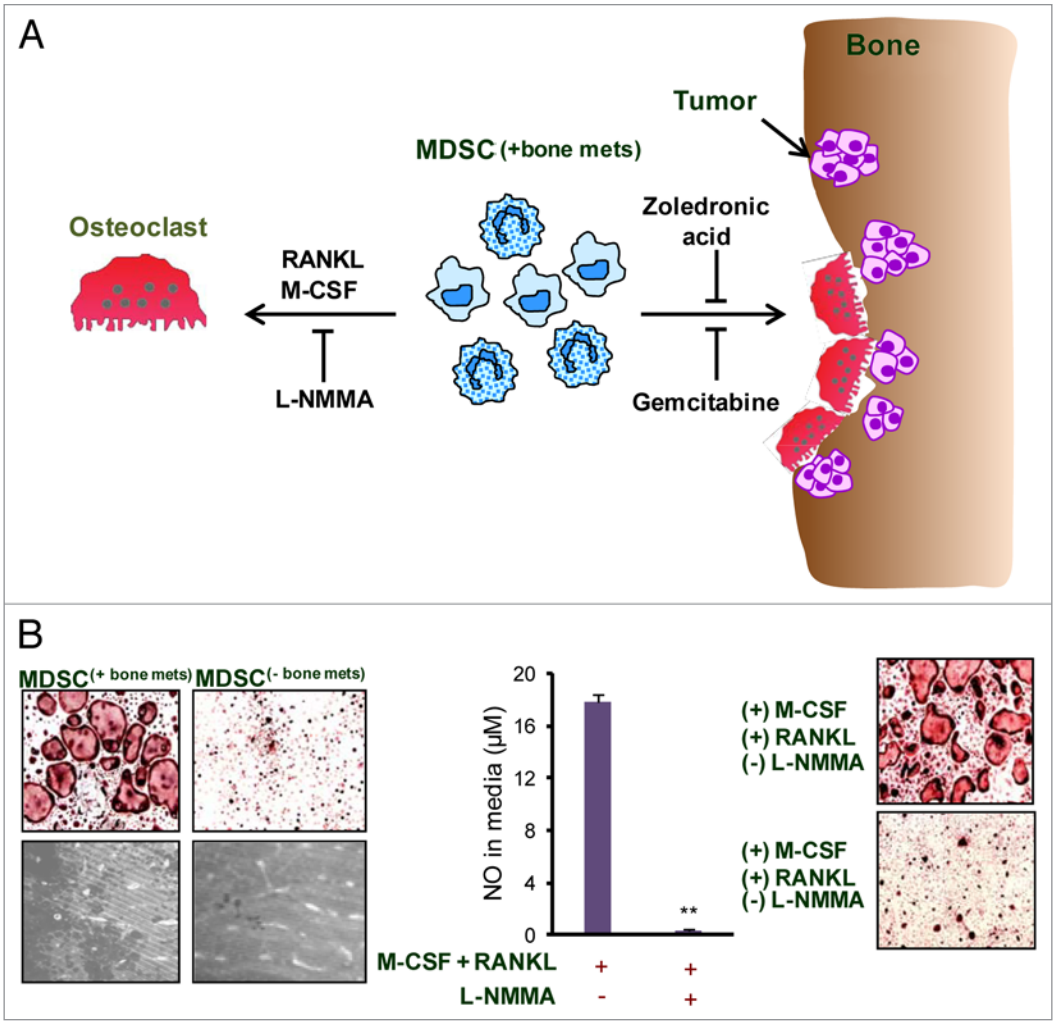

Figure 1. Role and mechanism of MDSC-mediated osteoclastogenesis in bone metastases. (**A**) As osteolytic cancers grow within bone, an increased influx of myeloid derived suppressor cells ($MDSC^{(+bone\ mets)}$) is noted. When these $MDSC^{(+bone\ mets)}$ are cultured in the presence of receptor activator of nuclear factor-κB ligand (RANKL) and macrophage colony-stimulating factor (M-CSF), they undergo differentiation into multi-nucleated, acid phosphatase 5, tartrate resistant $(ACP5)^{+}$ osteoclasts. Nitric oxide (NO) signaling is crucial for MDSC differentiation into osteoclasts and can be blunted using NG-monomethyl-*L*-arginine acetate (L-NMMA), an inducible NO synthase (iNOS) inhibitor. The adoptive transfer of $MDSC^{(+bone\ mets)}$ results in increased osteolytic lesions and tumor growth in the bone of recipient mice. MDSC-mediated osteolysis can also be controlled in vivo by gemcitabine or zoledronic acid. The administration of either these agents reduces MDSC abundance, hence limiting osteolytic lesions and tumor growth. (**B**) Data show that MDSC isolated from mice bearing bone metastases ($MDSC^{(+bone\ mets)}$) are capable of differentiating into osteoclasts and resorbing bone, whereas MDSC from mice bearing non-metastatic tumors ($MDSC^{(-bone\ mets)}$) failed to differentiate into osteoclasts or exert bone-resorbing functions. NO levels are elevated in $MDSC^{(+bone\ mets)}$ and NO production can be inhibited with L-NMMA. In the presence of L-NMMA, $MDSC^{(+bone\ mets)}$ fail to differentiate into osteoclasts, proving the critical role of NO in this process.

cells secrete a variety of pro-osteoclastogenic growth factors. For instance, the chemokines chemokine (C-C motif) ligand 2 (CCL2, also known as monocyte chemoattractant protein 1) and CCL5 (best known as RANTES), secreted by BCa bone metastases are known stimulators of osteoclastogenesis. MDSC express CCR2, the receptor for CCL2, implying that they are responsive to this chemokine. Secreted phosphoprotein 1 (SSP1, best known as osteopontin) is expressed by a majority of Bca metastatic lesions and promote the expression of cathepsin K and matrix metallopeptidase 9 (MMP9), thus enhancing osteoclast functions.[7] The BM in MM lesions contains high levels of interleukin (IL)-1, IL-3, IL-6, IL-7, CCL20 and activin, all of which are osteoclast activating factors.[8] Moreover, factors secreted by cancer cells as well as mediators released by immune cells in the bone microenvironment also contribute to osteolysis. Both BCa and MM bone metastases are infiltrated by plasmacytoid dendritic cells (pDC), which promote immunosuppressive effects.[9,10] In both these settings, robust pDC infiltration is associated with high levels of IL-3, IL-6, IL-10, IL-15, CCL2, CCL5 and chemokine (C-X-C motif) ligand 10 (CXCL10). Some of these cytokines can induce osteoclastogenesis, either directly or indirectly by promoting the expression of RANKL. So, the presence of a pro-osteoclastogenic milieu in the metastatic

bone microenvironment may drive the differentiation of MDSCs into osteoclasts.

Considering the complications and poor prognosis that are associated with metastatic disease, there is an urgent need to develop novel specific therapeutic strategies. Targeting MDSC can be one of such approaches. For instance, the inhibition of NO signaling in MDSC may reduce MDSC-mediated osteolysis. Nitroaspirin is known to inhibit the inducible nitric oxide synthease (iNOS) in MDSC. Targeting the NO pathway in MDSCs may also inhibit MDSC-mediated immunosuppression. MDSC can be targeted using chemotherapeutics such as gemcitabine, which selectively and efficiently suppresses MDSC. In a pre-clinical BCa model, the administration of gemcitabine reduced indeed MDSC levels, controlled the extent of bone metastases and overall tumor growth.[3] Bisphosphonate, which is the primary therapeutic option for patients with bone metastases, also reduces the proliferation of MDSC. The treatment of MDSC isolated from MM-bearing mice with zoledronic acid significantly inhibited MDSC-mediated bone destruction in vivo.[5] Hence, a carefully designed combination therapy may reduce MDSC-mediated bone destruction and immunosuppression (**Fig. 1**).

Disclosure of Potential Conflicts of Interest

This work was supported in part by National Institutes of Health grants R01AR050251, 1R01AR058344-01, R01CA133737, and P30 AR046031-10 and by the U.S. Army Department of Defense grants BC044440 and BC101411.

References

1. Gabrilovich DI, Ostrand-Rosenberg S, Bronte V. Coordinated regulation of myeloid cells by tumours. Nat Rev Immunol 2012; 12:253-68; PMID:22437938; http://dx.doi.org/10.1038/nri3175
2. Almand B, Clark JI, Nikitina E, van Beynen J, English NR, Knight SC, et al. Increased production of immature myeloid cells in cancer patients: a mechanism of immunosuppression in cancer. J Immunol 2001; 166:678-89; PMID:11123353
3. Sawant A, Deshane J, Jules J, Lee CM, Harris BA, Feng X, et al. Myeloid-derived suppressor cells function as novel osteoclast progenitors enhancing bone loss in breast cancer. Cancer Res 2013; 73:672-82; PMID:23243021; http://dx.doi.org/10.1158/0008-5472.CAN-12-2202
4. Danilin S, Merkel AR, Johnson JR, Johnson RW, Edwards JR, Sterling JA. Myeloid-derived suppressor cells expand during breast cancer progression and promote tumor-induced bone destruction. Oncoimmunology 2012; 1:1484-94; PMID:23264895; http://dx.doi.org/10.4161/onci.21990
5. Zhuang J, Zhang J, Lwin ST, Edwards JR, Edwards CM, Mundy GR, et al. Osteoclasts in multiple myeloma are derived from Gr-1+CD11b+myeloid-derived suppressor cells. PLoS One 2012; 7:e48871; PMID:23173040; http://dx.doi.org/10.1371/journal.pone.0048871
6. Charles JF, Hsu LY, Niemi EC, Weiss A, Aliprantis AO, Nakamura MC. Inflammatory arthritis increases mouse osteoclast precursors with myeloid suppressor function. J Clin Invest 2012; 122:4592-605; PMID:23114597; http://dx.doi.org/10.1172/JCI60920
7. Das S, Samant RS, Shevde LA. Hedgehog signaling induced by breast cancer cells promotes osteoclastogenesis and osteolysis. J Biol Chem 2011; 286:9612-22; PMID:21169638; http://dx.doi.org/10.1074/jbc.M110.174920
8. Raje N, Roodman GD. Advances in the biology and treatment of bone disease in multiple myeloma. Clin Cancer Res 2011; 17:1278-86; PMID:21411443; http://dx.doi.org/10.1158/1078-0432.CCR-10-1804
9. Sawant A, Hensel JA, Chanda D, Harris BA, Siegal GP, Maheshwari A, et al. Depletion of plasmacytoid dendritic cells inhibits tumor growth and prevents bone metastasis of breast cancer cells. J Immunol 2012; 189:4258-65; PMID:23018462; http://dx.doi.org/10.4049/jimmunol.1101855
10. Chauhan D, Singh AV, Brahmandam M, Carrasco R, Bandi M, Hideshima T, et al. Functional interaction of plasmacytoid dendritic cells with multiple myeloma cells: a therapeutic target. Cancer Cell 2009; 16:309-23; PMID:19800576; http://dx.doi.org/10.1016/j.ccr.2009.08.019

Published OnlineFirst July 25, 2013; DOI: 10.1158/0008-5472.CAN-13-0305

Review

Cancer Research

Myeloid-Derived Suppressor Cells as Osteoclast Progenitors: A Novel Target for Controlling Osteolytic Bone Metastasis

Anandi Sawant and Selvarangan Ponnazhagan

Abstract

Immune cells and their secreted growth factors play major roles in tumor growth and metastasis. Interplay between the growing tumor and infiltrating immune cells determines the nature of immune response and ultimately, tumor fate. Increased infiltration of protumorigenic immune cells promotes tumor growth as well as dissemination to distant sites. These cells induce immunosuppression that inhibits proliferation and functions of cells of antitumor immune response. One population of immunosuppressive cells that is increasingly gaining attention is myeloid-derived suppressor cells (MDSC). MDSCs are immature myeloid progenitors that suppress T-cell effector functions and promote angiogenesis. MDSC numbers are elevated at both the primary tumor and metastatic sites, including bone. In addition to immunosuppressive functions of MDSCs, we and others have recently discovered a novel function for MDSCs as osteoclast progenitors. Osteolysis is a common complication in the carcinomas of breast, lung, prostate, and multiple myeloma with poor prognosis. Therefore, targeting the functions of MDSCs may exert dual therapeutic effects on immunosuppression and bone pathology. *Cancer Res; 73(15); 4606–10. ©2013 AACR.*

Introduction

One of the hallmarks of tumor progression is evading immunosurveillance, which allows tumor cells to escape antitumor immune response and/or to actively suppress it (1). This contributes to the establishment of primary tumors and subsequent metastasis. Innate and adaptive immune cell often infiltrate tumor sites. Different types of these immune cells and the products secreted by them determine the fate of tumor progression. Immune cells also play a major role in establishing metastasis of the primary tumor to various organs, including the bone (2, 3). A protective immune response against tumor is often prevailed by the protumor immune response and eventually, it is the balance or the lack of it between these two processes that determines the fate of tumor growth and metastasis. One of the immuosuppressive populations that is rapidly gaining interest and attention in the tumor biology is myeloid-derived suppressor cells (MDSC). These cells infiltrate various cancers and are often associated with poor prognosis (4). Several reports have shown increased infiltration of MDSCs in breast cancer, lung cancer, and multiple myeloma, both in the primary tumor and metastatic sites, including bone (5–7), which necessitates further understanding of the roles played by this population in cancer progression.

Authors' Affiliation: Department of Pathology, The University of Alabama at Birmingham, Birmingham, Alabama

Corresponding Author: Selvarangan Ponnazhagan, Department of Pathology, 1825 University Blvd., SHEL 814, The University of Alabama at Birmingham, Birmingham, AL 35294. Phone: 205-934-6731; Fax: 205-975-4919; E-mail: pons@uab.edu

doi: 10.1158/0008-5472.CAN-13-0305

MDSCs as Immunosuppressive Cells

MDSCs are a heterogeneous population comprising immature myeloid cells (IMC). Under normal conditions, the IMC differentiate into mature macrophages, dendritic cells, and granulocytes. However, in pathologic conditions, including cancer, IMC differentiation is inhibited, resulting in accumulation of immunosuppressive MDSCs (4). In mice, MDSCs are identified mainly by the presence of CD11b and Gr-1. Two main subsets of MDSCs are monocytic MDSCs (M-MDSC; $CD11b^{hi}Gr\text{-}1^{mid}Ly6C^{hi}Ly6G^{lo}$) and granulocytic MDSCs (G-MDSC; $CD11b^{hi}Gr\text{-}1^{mid}Ly6C^{lo}Ly6G^{hi}$). In humans, MDSCs are characterized mainly as $CD11b^{+}CD33^{+}HLA\text{-}DR^{-}$ cells. MDSCs expressing CD14 are M-MDSCs, whereas $CD14^{-}$ cells are G-MDSCs. In both mice and humans, M-MDSCs have high levels of nitric oxide (NO) and very low levels of reactive oxygen species (ROS), whereas the reverse is true for G-MDSCs. However, both of these subtypes have high arginase activity (4, 7, 8).

MDSCs play a pivotal role in cancer progression by suppressing both innate and adaptive immune response. Accumulation of MDSCs has been reported in almost all cancers, both in the preclinical models and human patients. MDSCs are present in abundance within primary and metastatic solid tumors (8). Tumor progression is associated with gradual accumulation of this immunosuppressive population in bone marrow, spleen, peripheral blood, and lymph nodes. MDSCs suppress T-cell effector functions in several ways. MDSCs deplete L-arginine through arginase-1 (ARG)-dependent consumption and by

Published OnlineFirst July 25, 2013; DOI: 10.1158/0008-5472.CAN-13-0305

sequestering L-cysteine and thus suppress the proliferation of T cells. ROS and NO generated by MDSCs suppress T-cell functions by loss of TCR-ζ chain expression, nitration, and desensitization of the T-cell receptor (TCR) and interference with interleukin (IL)-2 receptor signaling. MDSCs express certain surface proteins, such as ADAM 17 (a disintegrin and metalloproteinase domain-containing 17) and Galectin 9, that interfere with trafficking of T cells and induce their apoptosis, respectively. Besides suppressing effector T-cell populations, MDSCs promote the activation and expansion of regulatory T cells (Treg) and thus mediate immunosuppression. MDSCs also produce factors that promote tumor growth by inducing angiogenesis and lymphangiogenesis. MDSCs secrete several proangiogenic markers and can directly incorporate into tumor endothelium (4, 7).

These diverse mechanisms used by MDSCs allow tumor growth and metastasis to multiple organs, including the bone (4, 9). MDSC numbers are elevated in multiple myeloma and as breast cancer disseminate to the bone (5, 10). Bone is one of the major organs for breast, lung, and prostate metastasis, whereas multiple myeloma originates in the bone. Bone metastasis is often associated with poor prognosis and high morbidity. Nearly 80% to 90% of all breast cancer patients with advanced disease have osteolytic pathology as characterized by increased bone damage resulting from enhanced osteoclast activity (11). Bone undergoes a constant remodeling through osteoclast-mediated bone resorption and osteoblast-mediated bone regeneration in a tightly coupled manner to maintain homeostasis. However, during tumor growth in the bone, dysregulation of this process leads to either osteolytic or osteoblastic phenotypes (12). Bone metastases are often associated with increase in osteoclast activation and osteolysis.

Given that MDSCs are progenitors of macrophages, which are osteoclast precursor cells, and MDSC numbers greatly increase during cancer bone metastasis, their role in enhanced osteoclastogenesis is of significant interest.

MDSCs as Novel Osteoclast Progenitors

Osteoclasts are giant, multinucleated, bone-degrading cells. They are characterized by high expression of tartrate-resistant acid phosphatase (TRAP) and cathepsin K. Two critical factors for osteoclast formation are receptor activator of nuclear factor-κB ligand (RANKL) and macrophage colony-stimulating factor (M-CSF). Interactions of RANKL with the receptor RANK and that of M-CSF with its receptor colony-stimulating factor 1 receptor (c-fms) trigger a series of signaling pathways that lead to osteoclastogenesis (12). Stimulation of macrophages *in vitro* with M-CSF and RANKL induces their differentiation into multinucleated osteoclasts (13). Various signaling mechanisms, such as ROS and NO production, are involved in osteoclastogenesis (13).

Aside from being progenitors of macrophages, which differentiate into osteoclasts, MDSCs have recently been identified by ourselves and others in the bone-tumor microenvironment that undergo direct osteoclastic osteoclast differentiation and contribute to enhanced bone destruction and tumor growth. Our data show that MDSCs isolated from the tumor-bearing mice with bone metastasis differentiated into functional bone-resorbing osteoclasts *in vitro* and *in vivo* (5). This indicates that these cells are primed to be osteoclast progenitors (OCP) and the bone microenvironment *in vivo* triggers their differentiation into functional osteoclasts. More importantly, not all MDSC populations were capable of osteoclast differentiation. In our study, we differentiated MDSCs from lung, spleen, blood, and lymph nodes of tumor-challenged mice into osteoclasts. None of these MDSCs differentiated into osteoclasts, which suggested that the bone microenvironment is essential. However, MDSCs isolated from bone showing presence of metastasized tumor underwent osteoclast differentiation, but this did not happen in the ones without tumor or control bone marrow–derived MDSCs (Fig. 1). This clearly shows that for MDSCs to differentiate into osteoclasts, signals from both bone marrow cells and bone metastases are needed. It remains to be determined which factors are involved in polarizing MDSCs for osteoclast differentiation. Breast cancer cells present in the bone secrete a variety of growth factors, including MCP-1 and RANTES, both of which are osteoclastogenic. MDSCs express CCR2, the receptor for MCP-1, and thus are responsive to this cytokine. Ongoing studies in our laboratory are focused on understanding interactive signals between cancer cells, MDSCs, and the bone microenvironment.

Besides our report, Danilin and colleagues reported similar observations using a human breast cancer cell line (9). They showed that MDSCs from tumor-bearing mice upregulated parathyroid hormone-related protein (PTHrP) and Gli2 mRNA levels in cancer cells, both of which are involved in osteoclast activation. When mice were injected with breast cancer cells along with either immature myeloid precursors (iMC) from healthy donors or MDSCs from tumor-bearing mice, the latter showed significant bone metastasis and osteolysis, thus supporting our observation that MDSCs from bone, containing tumor, are primed to be osteoclast precursors. Although iMC underwent osteoclast differentiation, they generated much fewer osteoclasts and reduced bone resorption compared with MDSCs. It is possible that prolonged culture of iMC in RANKL and M-CSF may have induced their differentiation into macrophages and therefore resulted in osteoclast differentiation. Clearly, these findings also can be extended to other osteolytic malignancies such as lung metastases and multiple myeloma. A recent report by Zhuang and colleagues showed a similar function of MDSCs as OCPs in a syngeneic murine multiple myeloma model (10). MDSCs from this model could promote bone resorption both *in vitro* and *in vivo*. This study also showed that MDSCs from tumor-bearing mice differentiated with greater potential into osteoclasts, thus bolstering observations reported in breast cancer. Studies have shown that osteoclast differentiation of macrophages can occur independently of RANK stimulation during certain pathologic states (14, 15). It will be interesting to determine whether any such RANK-independent activation triggers MDSC differentiation into osteoclasts.

Similar to bone metastasis, osteolysis is also observed under other pathologic conditions such as rheumatoid arthritis. Using a murine rheumatoid arthritis model, which is clinically

Published OnlineFirst July 25, 2013; DOI: 10.1158/0008-5472.CAN-13-0305

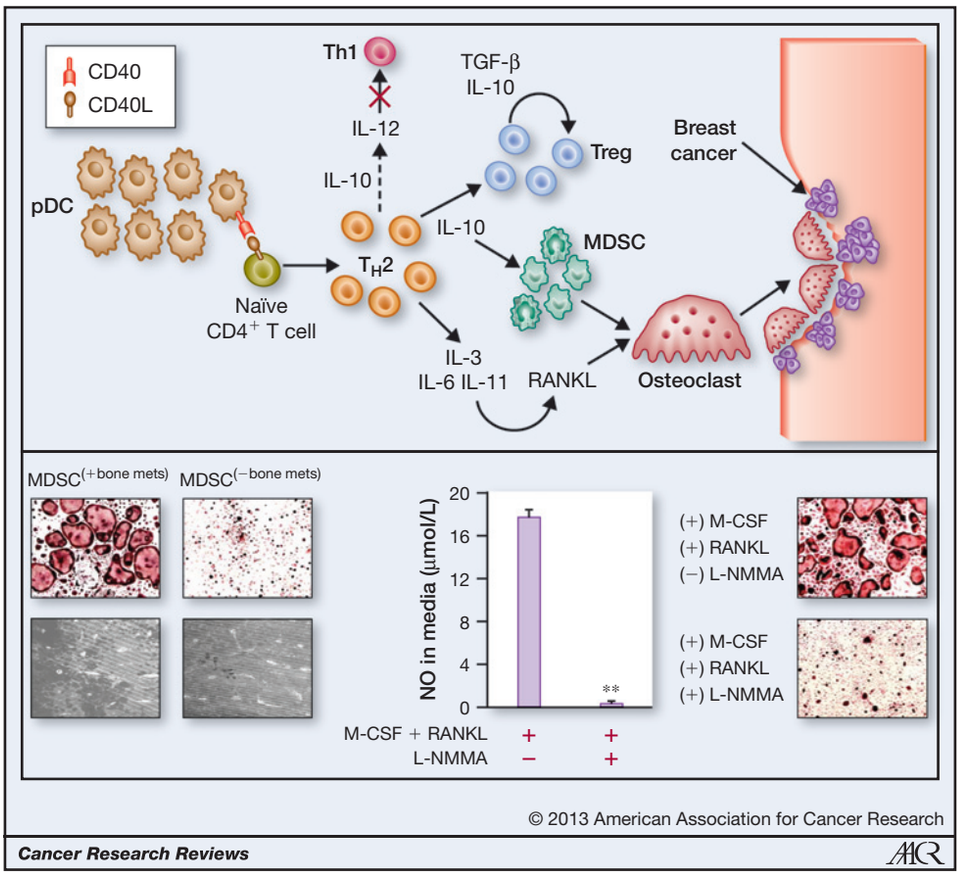

Figure 1. A, with dissemination of breast cancer to the bone, there is a significant elevation in the numbers of pDCs. pDCs interact with naïve $CD4^+$ T cells via CD40/CD40L and induce their differentiation in the immunosuppressive T_H2 cells. The presence of T_H2 cells results in suppression of T_H1 cell response and further induces immunosuppression via Tregs and MDSCs. Cytokines secreted by T_H2 cells induce RANKL. MDSCs in the bone microenvironment undergo osteoclast differentiation and induce osteolysis. This allows growth and establishment of bone metastasis of breast cancer. B, MDSCs isolated from tumor-bearing mice with bone metastasis ($MDSC^{(+bone\ mets)}$) undergo osteoclast differentiation and resorb bone, whereas those from tumor-bearing mice without bone metastasis ($MDSC^{(-bone\ mets)}$) are incapable of differentiating into osteoclasts or inducing osteolysis. Furthermore, NO is crucial for differentiation of MDSCs into osteoclasts. In the presence of L-NMMA, an inhibitor of NO synthesis, $MDSC^{(+bone\ mets)}$ do not differentiate into osteoclasts, as described earlier by Sawant and colleagues (5).

similar to human rheumatoid arthritis, Charles and colleagues showed MDSCs as the primary OCP that is capable of differentiating into functional osteoclasts involving NO signaling (16). Similar to our observation, in the rheumatoid arthritis model OCPs also expressed CD115, the M-CSF receptor. From these recent reports, it is clear that MDSCs are novel OCPs and thus targeting MDSC could help develop new therapeutic strategies for controlling osteolysis.

Role of NO in MDSC-Mediated Osteoclast Differentiation

Both NO and ROS are well-known mediators of osteoclast differentiation. NO is known to induce osteoclast differentiation of macrophages. Mice with knockout of inhibitor of inducible NO synthase (iNOS) show reduced bone loss due to impaired osteoclast function. Stimulation of macrophages via RANKL transiently increases ROS production through TNF receptor–associated factor (TRAF) 6, Rac1, and NADPH oxidase (Nox) 1. Inhibitors that block Nox1 or a deficiency in TRAF6 inhibit response of macrophages to RANKL, thus resulting in reduced osteoclastogenesis. Pretreatment of osteoclasts with antioxidants also reduced RANKL signaling and therefore osteoclast differentiation (13). Because MDSCs mediate immunosuppression via ROS and NO, we sought to find out if any of these pathways are also involved in osteoclast differentiation. Our data showed a critical role of NO synthesis in generation of MDSC-mediated osteoclastogenesis. Inhibition of NO production reduced MDSC-mediated osteolysis both *in vitro* and *in vivo*. Hence, NO production has a dual role in MDSC function. Considering that monocytic MDSCs are major producers of NO, it will be interesting to determine if M-MDSCs are the major source of MDSC-generated osteoclasts.

The question is what leads to increased NO levels in the bone-tumor microenvironment. One of the important features of the bone microenvironment during metastasis is hypoxia, which makes it a fertile ground for homing of metastatic cancer cells. The most common transcription factor that is expressed

Published OnlineFirst July 25, 2013; DOI: 10.1158/0008-5472.CAN-13-0305

under hypoxic conditions is hypoxia inducible factor (HIF)-1α. Breast cancer that has metastasized to the bone expresses higher levels of HIF-1α than the primary tumor, and it was shown, in turn, to increase the bone metastatic potential of these cells. On the other hand, reduced bone metastasis was observed in tumor cells lacking HIF-1α. Overexpression of HIF-1α increased osteoclast formation while inhibiting osteoblast differentiation, thus showing a direct role of this transcription factor in osteoclastogenesis (17).

One of the signaling pathways regulated by HIF-1α is NO production via iNOS (18). Evidence also shows that NO can induce HIF-1α by signaling through the phosphoinositide 3-kinase and mitogen-activated protein kinase (19). Hence, this positive feedback response allows for osteoclast differentiation.

Clinical Significance of MDSCs as Osteoclast Precursors

Metastasis of cancer cells to the bone is a major clinical complication that is associated with pain, bone fracture, hypercalcemia, and decreased mobility and thus affects overall quality of life for the patient. Although current therapies exist for treatment of bone metastases, they are limited and are focused on symptomatic management, thus limiting progression of established disease. Hence, a better understanding of the processes that play a role in therapy of bone metastases may offer new strategies for therapeutic intervention and extended survival. From recent evidence that MDSCs contribute to bone metastases in multiple ways, future treatment options may be developed that target this population of cells. Such approaches may be combined with existing therapies for adjuvant effect.

Gemcitabine is a chemotherapy agent used for carcinomas of the lung, pancreas, bladder, and breast. Interestingly, this drug also specifically inhibits MDSC populations *in vivo* (20). Therefore, gemcitabine may be used not only as an antitumor drug but also for reducing bone destruction. More importantly, use of gemcitabine in patients with bone metastasis may have more impact because it will not only reduce overall tumor burden but also reduce tumor growth in the bone and osteolysis. Our *in vivo* study showed that gemcitabine-treated mice not only had fewer MDSCs but the breast cancer growth in the bone was also reduced (5). Elevation in MDSCs is also observed in lung cancer. A similar approach may be used for treatment of patients with lung cancer to control both tumor growth and bone dissemination. As MDSCs function as osteoclast precursors in rheumatoid arthritis, gemcitabine could be used for controlling MDSC-mediated osteolysis under this pathologic condition. Besides gemcitabine, doxorubicin-cyclophosphamide also has inhibitory effects on MDSCs proliferation. Docetaxel, a common chemotherapy drug for patients with breast and prostate cancer, also suppresses MDSCs by polarizing their differentiation into M1 macrophages (21). Docetaxel is commonly given to patients with bone metastasis, where it delays the onset of osteolytic lesions, which may be the result of docetaxel-mediated inhibition of MDSCs (22). A therapeutic approach using combinations of these chemotherapy drugs may help in controlling bone destruction and tumor growth.

Studies have identified that plasmacytoid dendritic cells (pDC) are elevated in patients with carcinomas of breast and lung, and multiple myeloma, both in the primary cancer and at metastatic sites. Using a syngeneic mouse model of breast cancer, we reported recently that pDCs numbers are significantly elevated during progressive stages of cancer dissemination to the bone (Fig. 1). Elevated pDCs correlated with increased MDSCs infiltration in bone (6). A similar situation is noted in multiple myeloma, where immune dysfunction is caused partially by pDCs and results in high MDSCs numbers in the bone. Therefore, treatments that control pDC function may help not only to control tumor growth and osteolysis but also to reduce MDSC-mediated immunosuppression and osteolysis. Depletion of pDCs in the preclinical murine model, using a specific antibody, resulted in a reduction of breast cancer growth and bone metastasis (6). Depletion of pDCs also reduced MDSCs levels. Therefore, targeting pDCs has a dual effect on tumor growth by (i) resulting in an antitumor immune response that reduces the tumor growth and (ii) decreasing bone dissemination of cancer by reducing MDSC numbers and osteolysis induced by MDSCs. Although these antitumor effects of pDC depletion have been reported in breast cancer, they may be extended to multiple myeloma as well as lung cancer, which also show increased pDC and MDSC numbers with tumor progression. Depletion of pDCs may be a useful therapeutic approach in combination with chemotherapy or bisphosphonate therapy for achieving better antitumor activity.

The common therapy for controlling bone metastasis of cancer is use of bisphosphonates. Bisphosphonates are used for treatment of breast cancer, multiple myeloma, and prostate cancer. Bisphosphonates attach preferentially to calcium and thus are accumulated in the bone at high concentrations. Nitrogen containing bisphosphonates such as zoledronic acid are ingested by osteoclasts, in which they inhibit the enzyme farnesyl pyrophosphate synthase. The bisphosphonates induce osteoclast apoptosis that in turn leads to an antiresorptive effect (23). Such bisphosphonates also reduce proliferation of MDSCs and thus can be used as viable agents for controlling both MDSCs and MDSC-mediated osteolysis. Zhuang and colleagues treated MDSCs from multiple myeloma–challenged mice with zoledronic acid. This resulted in a significant decrease in the number of osteoclasts formed in MDSCs culture and also inhibition of MDSCs and bone lesions *in vivo* (10). Therefore, a combination therapy using zoledronic acid along with gemcitabine may help to greatly control bone loss and tumor growth. In fact, a recent report showed that gemcitabine used along with bisphosphonates was more effective in reducing the number and size of bone metastases compared with gemcitabine alone in an animal model of human breast cancer (24). In addition to drugs that decrease MDSC numbers, inhibitors that can arrest MDSC functions, including ROS and NO inhibitors, may provide significant therapeutic effects not only targeting MDSCs but also targeting other protumorigenic mechanisms in the tumor microenvironment.

Administration of all-*trans* retinoic acid (ATRA), a vitamin A metabolite, also results in substantially decreased MDSC numbers in cancer patients and tumor-bearing mice. ATRA reduces numbers of MDSCs by inducing their differentiation into

Published OnlineFirst July 25, 2013; DOI: 10.1158/0008-5472.CAN-13-0305

dendritic cells and macrophages (4). This function of ATRA will help reduce MDSC-mediated osteolysis when this agent is administered in patients with bone metastasis. Thus, there are multiple therapy options that could be used to target MDSCs. These approaches will not only reduce MDSC-mediated osteolysis but also MDSC-mediated immunosuppression.

Conclusions

MDSCs besides being immunosuppressive, contribute actively to cancer-induced osteolysis by differentiating into functional, bone-resorbing osteoclasts. This displays the plasticity of the MDSC population in regards to their ability to differentiate into osteoclasts. This phenomenon is observed under pathologic conditions of cancer and rheumatoid arthritis, both of which are associated with complications caused by bone destruction. Therefore, therapies that target MDSCs directly may not only reduce its immunosuppressive functions but also MDSC-mediated osteolysis and for controlling disease complications.

Disclosure of Potential Conflicts of Interest

No potential conflicts of interest were disclosed.

Authors' Contributions

Conception and design: A. Sawant, S. Ponnazhagan
Development of methodology: A. Sawant, S. Ponnazhagan
Acquisition of data (provided animals, acquired and managed patients, provided facilities, etc.): A. Sawant, S. Ponnazhagan
Analysis and interpretation of data (e.g., statistical analysis, biostatistics, computational analysis): A. Sawant, S. Ponnazhagan
Writing, review, and/or revision of the manuscript: A. Sawant, S. Ponnazhagan
Administrative, technical, or material support (i.e., reporting or organizing data, constructing databases): A. Sawant, S. Ponnazhagan
Study supervision: S. Ponnazhagan

Grant Support

This study was supported by NIH grants AR050251, AR560948, CA132077, CA133737, P30 AR046031, and P30 AR48311, and DoD grant DoD-BC101411.

Received January 29, 2013; revised May 3, 2013; accepted May 9, 2013; published OnlineFirst July 25, 2013.

References

1. Vesely MD, Kershaw MH, Schreiber RD, Smyth MJ. Natural innate and adaptive immunity to cancer. Annu Rev Immunol 2011;29:235–71.
2. D'Amelio P, Fornelli G, Roato I, Isaia GC. Interactions between the immune system and bone. World J Orthop 2011;2:25–30.
3. Kim R, Emi M, Tanabe K, Arihiro K. Tumor-driven evolution of immunosuppressive networks during malignant progression. Cancer Res 2006;66:5527–36.
4. Gabrilovich DI, Nagaraj S. Myeloid-derived suppressor cells as regulators of the immune system. Nat Rev Immunol 2009;9:162–74.
5. Sawant A, Deshane J, Jules J, Lee CM, Harris BA, Feng X, et al. Myeloid-derived suppressor cells function as novel osteoclast progenitors enhancing bone loss in breast cancer. Cancer Res 2012;73:672–82.
6. Sawant A, Hensel JA, Chanda D, Harris BA, Siegal GP, Maheshwari A, et al. Depletion of plasmacytoid dendritic cells inhibits tumor growth and prevents bone metastasis of breast cancer cells. J Immunol 2012;189:4258–65.
7. Ostrand-Rosenberg S, Sinha P. Myeloid-derived suppressor cells: linking inflammation and cancer. J Immunol 2009;182:4499–506.
8. Gabrilovich DI, Ostrand-Rosenberg S, Bronte V. Coordinated regulation of myeloid cells by tumours. Nat Rev Immunol 2012;12:253–68.
9. Danilin S, Merkel AR, Johnson JR, Johnson RW, Edwards JR, Sterling JA. Myeloid-derived suppressor cells expand during breast cancer progression and promote tumor-induced bone destruction. Oncoimmunology 2012;1:1484–94.
10. Zhuang J, Zhang J, Lwin ST, Edwards JR, Edwards CM, Mundy GR, et al. Osteoclasts in multiple myeloma are derived from Gr-1+CD11b+myeloid-derived suppressor cells. PLoS One 2012;7:e48871.
11. Lippman ME. Breast cancer. In: Harrison's principles of internal medicine edn 16, part 7. New York: McGraw-Hill; 2005. p. 516–23.
12. Boyce BF, Rosenberg E, de Papp AE, Duong le T. The osteoclast, bone remodelling and treatment of metabolic bone disease. Eur J Clin Invest 2012;42:1332–41.
13. Nakashima T, Takayanagi H. Osteoclasts and the immune system. J Bone Miner Metab 2009;27:519–29.
14. Kobayashi K, Takahashi N, Jimi E, Udagawa N, Takami M, Kotake S, et al. Tumor necrosis factor alpha stimulates osteoclast differentiation by a mechanism independent of the ODF/RANKL-RANK interaction. J Exp Med 2000;191:275–86.
15. Weitzmann MN, Cenci S, Rifas L, Brown C, Pacifici R. Interleukin-7 stimulates osteoclast formation by up-regulating the T-cell production of soluble osteoclastogenic cytokines. Blood 2000;96:1873–8.
16. Charles JF, Hsu LY, Niemi EC, Weiss A, Aliprantis AO, Nakamura MC. Inflammatory arthritis increases mouse osteoclast precursors with myeloid suppressor function. J Clin Invest 2012;122:4592–605.
17. Papachristou DJ, Basdra EK, Papavassiliou AG. Bone metastases: molecular mechanisms and novel therapeutic interventions. Med Res Rev 2010;32:611–36.
18. Corzo CA, Condamine T, Lu L, Cotter MJ, Youn JI, Cheng P, et al. HIF-1alpha regulates function and differentiation of myeloid-derived suppressor cells in the tumor microenvironment. J Exp Med 2010;207:2439–53.
19. Sheta EA, Trout H, Gildea JJ, Harding MA, Theodorescu D. Cell density mediated pericellular hypoxia leads to induction of HIF-1alpha via nitric oxide and Ras/MAP kinase mediated signaling pathways. Oncogene 2001;20:7624–34.
20. Sinha P, Clements VK, Bunt SK, Albelda SM, Ostrand-Rosenberg S. Cross-talk between myeloid-derived suppressor cells and macrophages subverts tumor immunity toward a type 2 response. J Immunol 2007;179:977–83.
21. Kodumudi KN, Woan K, Gilvary DL, Sahakian E, Wei S, Djeu JY. A novel chemoimmunomodulating property of docetaxel: suppression of myeloid-derived suppressor cells in tumor bearers. Clin Cancer Res 2010;16:4583–94.
22. Miller RE, Roudier M, Jones J, Armstrong A, Canon J, Dougall WC. RANK ligand inhibition plus docetaxel improves survival and reduces tumor burden in a murine model of prostate cancer bone metastasis. Mol Cancer Ther 2008;7:2160–9.
23. Gnant M, Dubsky P, Hadji P. Bisphosphonates: prevention of bone metastases in breast cancer. Recent Results Cancer Res 2007;192:65–91.
24. El-Mabhouh AA, Nation PN, Abele JT, Riauka T, Postema E, McEwan AJ, et al. A conjugate of gemcitabine with bisphosphonate (Gem/BP) shows potential as a targeted bone-specific therapeutic agent in an animal model of human breast cancer bone metastases. Oncology Res 2011;19:287–95.

Published OnlineFirst July 25, 2013; DOI: 10.1158/0008-5472.CAN-13-0305

Cancer Research
The Journal of Cancer Research (1916–1930) | The American Journal of Cancer (1931–1940)

AACR American Association for Cancer Research

Myeloid-Derived Suppressor Cells as Osteoclast Progenitors: A Novel Target for Controlling Osteolytic Bone Metastasis

Anandi Sawant and Selvarangan Ponnazhagan

Cancer Res 2013;73:4606-4610. Published OnlineFirst July 25, 2013.

Endostatin: A novel inhibitor of androgen receptor function in prostate cancer

Joo Hyoung Lee[a], Tatyana Isayeva[a], Matthew R. Larson[b], Anandi Sawant[a], Ha-Ram Cha[a], Diptiman Chanda[a], Igor N. Chesnokov[c], and Selvarangan Ponnazhagan[a,1]

Departments of [a]Pathology and [c]Biochemistry and Molecular Genetics, University of Alabama, Birmingham, AL 35294; and [b]Department of Biological Chemistry, University of Michigan Medical Center, Ann Arbor, MI 48109

Edited* by Louise T. Chow, University of Alabama at Birmingham, Birmingham, AL, and approved December 29, 2014 (received for review September 12, 2014)

Acquired resistance to androgen receptor (AR)-targeted therapies compels the development of novel treatment strategies for castration-resistant prostate cancer (CRPC). Here, we report a profound effect of endostatin on prostate cancer cells by efficient intracellular trafficking, direct interaction with AR, reduction of nuclear AR level, and down-regulation of AR-target gene transcription. Structural modeling followed by functional analyses further revealed that phenylalanine-rich α1-helix in endostatin—which shares structural similarity with noncanonical nuclear receptor box in AR—antagonizes AR transcriptional activity by occupying the activation function (AF)-2 binding interface for coactivators and N-terminal AR AF-1. Together, our data suggest that endostatin can be recognized as an endogenous AR inhibitor that impairs receptor function through protein–protein interaction. These findings provide new insights into endostatin whose antitumor effect is not limited to inhibiting angiogenesis, but can be translated to suppressing AR-mediated disease progression in CRPC.

endostatin | androgen receptor | prostate cancer | chemoresistance

Abnormalities in the androgen–androgen receptor (AR) axis have been well recognized in promoting prostate cancer (PCa) growth and metastasis. Although the current therapies using androgen deprivation and antiandrogens show transient tumor regression, the tumor relapse to castration-refractory metastatic stage remains a big challenge (1). The molecular basis of continued AR function in castration-resistant PCa (CRPC) has shifted the paradigm in our understanding of androgen-independent mechanisms, leading to therapeutic strategies directly targeting the receptor (2, 3). Despite modest improvements in AR-targeted therapies, tumor relapse ensues with up-regulated AR expression and transcriptional activation of downstream AR-target genes (4, 5). Recent studies also identified that a somatic mutation in AR ligand-binding domain (LBD; F876L) sustains AR function by converting antagonistic actions of the second-generation antiandrogens, such as enzalutamide and ARN-509, to agonist response (1, 6). Thus, discovery of potent AR antagonists that can overcome AR-associated drug resistance remains imminent for clinical management of CRPC.

Endostatin (ES) is a 20-kDa proteolytic fragment of a noncollagenous domain (NC-1) in collagen type XVIII (7). As an endogenous antiangiogenic protein, ES inhibits endothelial cell proliferation and tube formation (8, 9). Since Judah Folkman's laboratory first identified ES (10, 11), anticancer effects of ES have been extensively studied in both tumors and tumor-associated endothelia (8, 12–14). In addition, studies with recombinant human ES fused with Zinc-binding peptide (ZBP-endostatin; Endostar) showed clinical benefit in patients with non-small-cell lung cancer (NSCLC) (11). Recently, we showed that systemically stable levels of ES by vector-mediated gene transfer in vivo significantly delayed tumor growth in the transgenic adenocarcinoma of mouse prostate model (15).

AR is a 120-kDa protein, composed of an N-terminal domain (NTD), a DNA binding domain (DBD), a hinge domain, and a C-terminal LBD. Like other nuclear receptors (NRs), AR is a transcription factor regulating target-gene expression in a ligand-dependent manner (2, 16). Cognate ligand binding induces conformational changes predominantly in helix 12 of AR LBD, which enhances transcriptional activity by forming a ligand-dependent AF-2 binding interface for coactivators (17). Wilson and colleagues demonstrated that the interdomain interaction between AF-1 in NTD and AF-2 in LBD (N/C interaction) leads to AR stabilization and slower ligand dissociation (18, 19).

Functional activity of AR largely depends on AF-2 that accommodates the binding of various AR coactivators by recognizing specific sequence motifs, called NR box. Among NRs, AR is known to exhibit the binding preference to noncanonical NR box, containing FXXLF, FXXFF, and WXXLF motifs (20, 21). In addition to coactivators, AR NTD has two AF-2–binding helical segments with FXXLF (residues 23–27) and WXXLF (residues 435–439) motifs. Interestingly, such binding motifs are also observed in ES α1-helix (F31–F34) and α2-helix (W83–F87), respectively (22, 23). The similarities both in the sequence and structure between the helical motifs of ES and AR prompted us to study whether ES can mimic the structural basis of AR–NTD or coactivator binding to AR LBD. In line with our previous study showing the inhibitory effect of ES on PCa tumorigenesis, here, we provide direct evidence, for the first time, to our knowledge, that ES is a novel antagonist of AR function in PCa cells. The present study demonstrates that a direct molecular interaction of ES with AR disrupts AR-target gene transcription, leading to PCa growth inhibition.

Significance

Despite the development of second-generation androgen receptor (AR)-targeted therapies for castration-resistant prostate cancer (CRPC), the effects are only modest, compelling the need for novel therapy combinations that can maximize the antitumor effects of new-generation chemotherapies with minimal acquired resistance, attributed to AR modifications. The present study identified that endostatin (ES), known for its antiangiogenic properties on tumor vasculature, exerts a profound antiproliferative effect on AR-positive human PCa cells. By a systematic approach involving a combination of in situ, cell-free, yeast-two hybrid, structural modeling, and mutagenesis studies, we determined that intracellular trafficking of ES in AR-positive PCa cells leads to a direct interaction with AR in the cytosol, affecting the transcriptional activation of AR target genes.

Author contributions: J.H.L., T.I., and S.P. designed research; J.H.L., T.I., M.R.L., A.S., and H.-R.C. performed research; I.N.C. contributed new reagents/analytic tools; J.H.L., T.I., M.R.L., D.C., and S.P. analyzed data; and J.H.L. and S.P. wrote the paper.

The authors declare no conflict of interest.

*This Direct Submission article had a prearranged editor.

[1]To whom correspondence should be addressed. Email: pons@uab.edu.

This article contains supporting information online at www.pnas.org/lookup/suppl/doi:10.1073/pnas.1417660112/-/DCSupplemental.

Results

ES Targets AR Function in PCa Cells. To characterize the mechanism of action of ES on PCa cells, recombinant human ES was produced to homogeneity. Limitations in the production of ES in a soluble form, due to the presence of two disulfide bonds (11, 22) and complexities in refolding steps (8, 24, 25), were overcome by using the Origami B(DE3) *Escherichia coli* strain. The expression system with glutathione reductase (*gor*) and thioredoxin reductase (*trxB*) mutations resulted in a high yield of soluble ES without requiring a refolding process (Fig. S1 *A* and *B*). Recombinant ES with a C-terminal His-tag and the N-terminal heparin-binding site, formed by 11 arginines, enabled the efficient protein purification using nickel-affinity and heparin-agarose columns, respectively (Fig. S1*C*). The biological activity of the purified recombinant ES was verified on human umbilical vein endothelial cells (Fig. S1*E*).

To determine whether antitumor effects of ES are directly attributed to targeting AR function, both AR-positive (LNCaP and C4-2B) and AR-negative (PC3 and DU145) human PCa cells were included in the experiments (Fig. S2*A*). Our study indicated that ES demonstrated a dose-dependent growth inhibition preferentially on AR-positive PCa cells (Fig. 1*A*). Upon treatment with 1 μM ES for 72 h, the growth of LNCaP and C4-2B cells significantly decreased to 60.3% (±7.0) and 66.2% (±5.9), respectively ($P < 0.05$) (Fig. 1*A* and Fig. S2*B*). Furthermore, the invasiveness of ES-treated LNCaP cells decreased to 61.4% (±2.98) (Fig. S2*C*). Like other endogenous antiangiogenic factors, ES is known to induce apoptosis of endothelial cells through binding to and functionally disrupting cell-surface receptors (i.e., integrins) (26, 27). In line with our previous study (28), ES treatment also induced apoptosis in LNCaP cells by showing the activation of caspase-3 (Fig. S2*D*). However, such antiproliferative effects were not observed in AR-negative PC-3 and DU145 cells, suggesting in part that the molecular action of ES involves targeting of AR-mediated cellular event(s).

To test the effect of ES on downstream AR-target gene expression, the levels of prostate-specific antigen (PSA), transmembrane protease serine 2 (TMPRSS2), and prostatic acid phosphatase (ACPP) were examined as surrogates. Immunocytochemistry indicated that the levels of PSA and TMPRSS2 were substantially decreased in ES-treated LNCaP cells (Fig. 1*B* and Fig. S3). Quantitative mRNA and protein analyses further confirmed down-regulation of PSA and TMPRSS2 expression and up-regulation of AR-repressed ACPP expression (Fig. 1 *C* and *D*). Such changes in the AR-target gene expression profile were similarly observed in another AR-positive and androgen-responsive cell upon ES treatment (Fig. S4), indicating that ES impairs AR transcriptional activity in AR-positive PCa cells.

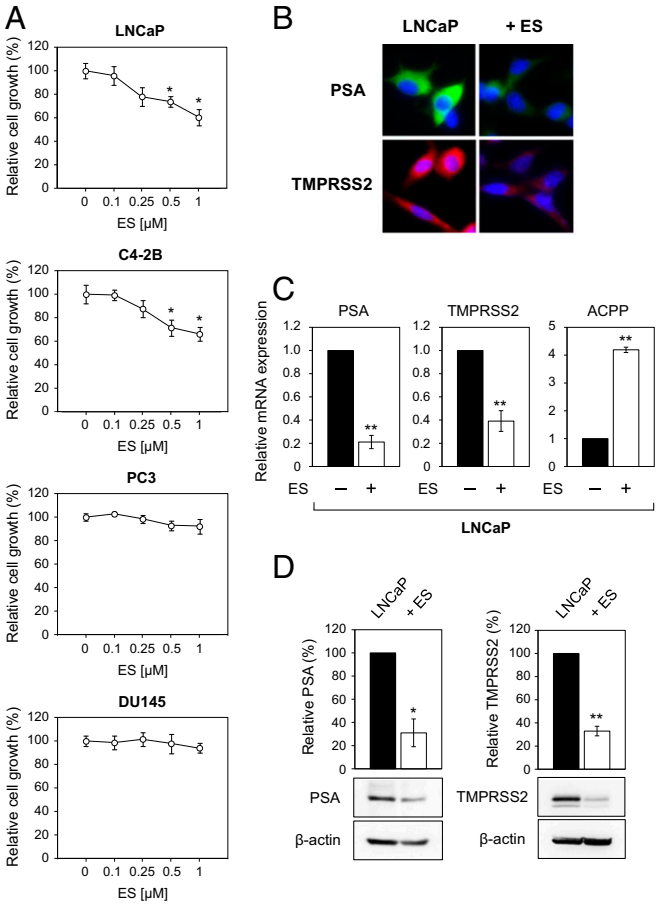

Fig. 1. Antiproliferative effect of ES in AR-positive PCa cells. (*A*) The indicated PCa cells were treated with increasing concentrations of ES for 72 h, and cell proliferation was determined every 24 h from replicate cultures (see also Fig. S2). Inhibitory effect on cell growth by ES is presented as a relative value (mean ± SD) compared with control as 100%. *$P < 0.05$ vs. control ($n = 3$). (*B–D*) To determine the effect of ES on AR-target gene transcription and translation, LNCaP cells were grown on chamber slides in the presence or absence of 1 μM ES and stained by using anti-PSA and -TMPRSS2 antibodies, followed by Alexa 488- and 594-labeled secondary antibodies, respectively (*B*). Nuclei were stained with DAPI (see also Fig. S3). From replicate experiments, total cell lysate and RNA were isolated, and the protein and mRNA expression levels of PSA, TMPRSS2, and ACPP were determined by real-time RT-PCR (*C*) and immunoblotting (*D*), respectively (see also Fig. S4). All results are expressed as mean ± SEM. *$P < 0.05$; **$P < 0.01$ vs. control.

Intracellular Trafficking of ES Reduces the Level of Nuclear AR. Next, we characterized the possible molecular mechanism of how ES disrupts AR function. When LNCaP cells were treated with recombinant ES, it was interesting to note that the majority of ES was detected in the cytoplasm. Both immunocytochemistry and subcellular fractionation analysis confirmed intracellular trafficking of ES by showing an augmentation of ES in the cytoplasmic fraction. In AR-negative PC3 cells, however, ES internalization was observed to a lesser extent (Fig. 2 *A* and *B*). This finding prompted us to further examine whether internalized ES could alter AR localization and function in situ. When compared to nontreated LNCaP cells, we found that the level of AR in the nucleus was significantly decreased by 70% ($P < 0.05$) upon ES treatment (Fig. 2*C*). In addition, immunofluorescence staining and quantitative protein analysis indicated an 86.2% decrease in total AR levels ($P < 0.01$) in ES-treated LNCaP cells (Fig. 2 *D* and *E*).

These observations raised a question of whether the internalized ES could induce AR degradation. Because 5α-dihydrotestosterone (DHT) binding to AR LBD is known to stabilize AR structure and function (3, 29), we speculated that the internalized ES may interfere with the ligand binding to AR LBD. However, diminution of DHT in culture had no influence on growth inhibition exerted by ES treatment (Fig. S2*E*). Furthermore, a similar level of growth inhibition was observed in AR-positive androgen-independent C4-2B cells (Fig. 1*A*), suggesting that the mechanism by which ES affects AR stability may not require perturbation of ligand binding to AR LBD. Secondly, ligand-dependent N/C interdomain interaction is known to stabilize the structural integrity of AR (18). Thus, it was conceivable that interaction of internalized ES with either AR NTD or LBD may have interrupted N/C interaction, thereby disrupting stability of the receptor. To test this hypothesis, it was crucial for us to investigate whether ES directly binds to AR.

ES Directly Interacts with AR. To elucidate the potential interaction of ES with AR, an array of binding assays were carried out. Recombinant ES was incubated with soluble cell lysate from

BIOCHEMISTRY

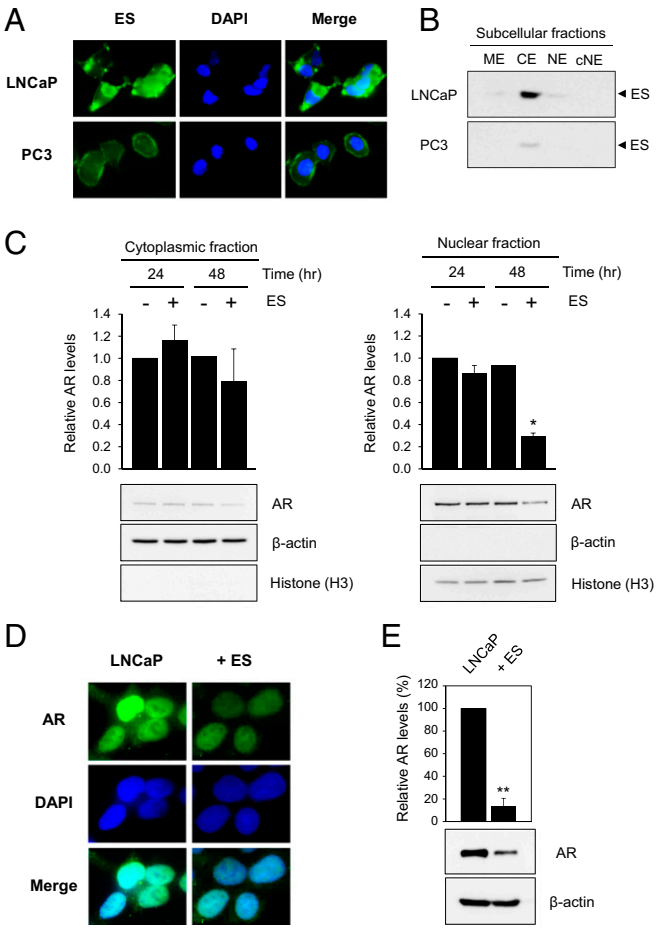

Fig. 2. Internalized ES reduces the level of nuclear AR. (*A*) LNCaP and PC3 cells were incubated with 1 μM biotin-labeled ES for 16 h. The internalized ES was probed with Alexa 488-conjugated avidin and visualized by fluorescence microscopy. (*B*) LNCaP and PC3 cells were treated with 1 μM ES for 48 h, after which membrane (ME), cytoplasmic (CE), nuclear (NE), and the chromatin-bound subnuclear (cNE) extracts were prepared stepwise for detecting ES internalization. (*C*) To determine the effect of internalized ES on AR nuclear transport, cytoplasmic (*Left*) and nuclear (*Right*) fractions from ES-treated LNCaP cells were analyzed for detecting the subcellular localization of AR. Quantitative analysis of AR levels in the cytoplasm and nucleus, relative to β-actin and histone (H3), respectively, are presented. Normalized AR levels are presented as relative values (mean ± SEM) of control. Experiments were repeated twice. $*P < 0.05$ vs. control. (*D*) To demonstrate in situ staining of AR, LNCaP cells were grown on chamber slides in the presence or absence of 1 μM ES and stained by using anti-AR antibody followed by Alexa 488-labeled secondary antibody. Nuclei were stained with DAPI. (*E*) Cell lysates from both control and ES-treated LNCaP cells were analyzed for AR expression by immunoblotting. The AR levels were normalized to β-actin levels. Results are expressed as mean ± SEM. $**P < 0.01$ vs. control ($n = 3$).

LNCaP cells that contained full-length AR, followed by immunoprecipitation using anti-ES antibody. Results indicated that AR was coimmunoprecipitated with ES (Fig. 3*A*). The ES–AR complex was also purified by pull-down of His-tagged ES using nickel-affinity chromatography (Fig. 3*B*). Protein analysis of the bound fraction showed that AR was coeluted with ES. The equivalent levels of β-actin in the input lysate and unbound fractions also confirmed predominant AR binding to ES, with a negligible level of free AR (Fig. 3*B*). The pull-down fraction was further analyzed by native-polyacrylamide gel electrophoresis (native-PAGE). In nondenaturing condition, AR with acidic isoelectric point ($p_I = 6.1$) was allowed to migrate into the native-gel at basic pH. In contrast, because of the pI (9.3) being above the pH (8.3) of Tris/glycine gel running buffer, ES did not migrate unless ES formed a complex with AR (Fig. S5). When the pull-down fraction was analyzed on native-PAGE followed by immunoblotting, both ES and AR were detected in the same band, indicating the formation of ES–AR complex (Fig. 3*C*).

In order to demonstrate unequivocally that ES binding to AR was due to a direct interaction, we performed yeast-two hybridization assay. For this experiment, ES was expressed as a protein fused with a DBD (LexA) as a bait protein, and AR was fused with a transcriptional activation domain (AD) as a prey (Fig. 3*D*). The ES–LexA and AR–AD fusion proteins were coexpressed in the EGY48 yeast cells where the binding site for LexA operator was located upstream of a *LEU2* and *LacZ* reporter genes. The results confirmed that transformed cells containing only ES–LexA or AR–AD gene failed to grow in leucine-dropout medium, indicating that overexpression of either bait or prey protein by itself did not activate downstream *LEU2* reporter gene transcription (Fig. 3*E*). The transformed cells expressing both ES–LexA and AR–AD formed blue colonies in the selective 5-bromo-4-chloro-3-indolyl β-D-galactoside (X-gal) medium without uracil, histidine, tryptophan and leucine

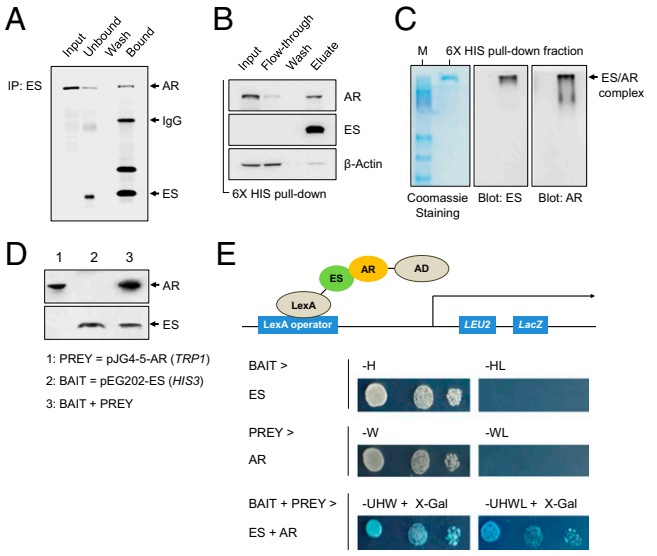

Fig. 3. Molecular interaction of ES with AR. (*A*) For coimmunoprecipitation studies, recombinant ES (1 μg) was incubated with LNCaP cell lysate (0.5 mg) in the presence of 10 nM DHT. The reaction mixture was immunoprecipitated with ES antibody. The ES–AR complex was resolved in SDS/PAGE and probed with ES and AR antibodies. Input indicates the concentration of AR used in the binding reaction. (*B*) The reaction mixture of recombinant ES and LNCaP cell lysate, in 1x PBS containing 20 mM imidazole and 10 nM DHT, was loaded onto Ni-NTA column, and the unbound proteins were collected (flow-through). After washing with 50 mM imidazole (wash), the bound fraction was pulled down by eluting with 500 mM imidazole (eluate). Immunoblots indicate ES–AR interaction. (*C*) The bound fraction (eluate) from the His-tag pull-down assay (Fig. 3*B*) was dialyzed and concentrated in 1x PBS (pH 7.4) and loaded onto 7.5% (wt/vol) polyacrylamide gel. Gel electrophoresis under nondenaturing condition confirmed apparent binding of ES and AR. See also Fig. S5. (*D* and *E*) Molecular association of ES with AR was confirmed by transcriptional activation of both colorimetric reporter (*LacZ*) and auxotrophic reporter (*LEU2*) genes in a yeast-two hybrid system. (*D*) ES and AR genes were subcloned into yeast expression vectors pEG202 and pJG4-5, respectively. The plasmids were transformed in EGY48 yeast cells, and the expression of LexA-ES (bait) and AR-AD (prey) fusion proteins were confirmed by immunoblotting. (*E*) Positive clones, coexpressing ES and AR, formed blue colonies on agar plates in the presence of X-gal (*LacZ* reporter gene transcription) and in the absence of leucine (*LEU2* reporter gene transcription), histidine (selection for pEG202-LexA-ES), tryptophan (selection for pJG4-5-AD-AR), and uracil (selection for pSH18-34).

(Fig. 3*E*). These results indicated that transcription of both *LEU2* and *LacZ* reporter genes was triggered by the bait-trap protein interaction, confirming a direct interaction between ES and AR.

In addition, because our binding experiments were carried out particularly in the presence of 10 nm DHT, it is possible that ES may target AR at the ligand-bound active conformation. To prove it experimentally, a pull-down assay was carried out in a similar manner, analyzing the reaction of ES with recombinant AR LBD. Results indicated that the LBD of AR is essentially involved in interaction with ES (Fig. 4*A*).

Structural Analysis on Putative ES-Binding Site in AR. Molecular association of ES with AR in conjunction with its mechanism of action related to AR antagonism led us to characterize the structural basis of this protein–protein interaction. Our structural analysis showed that potential interaction may occur between the positively charged cluster (R24, R27, and R139) followed by the ES α1-helix and the negatively charged cluster (E709, E873, and E897) near the AR AF-2 coactivator binding interface (Fig. 4*B*). Interestingly, we found that the α1-helix (R27–R38) and α2-helix (W83–F87) resemble the sequences of two α-helices in AR NTD that contain the FXXLF (R20–R31) and WXXLF (W435–F439) motifs, respectively (Fig. 4*C*). However, only α1-helix contains the key aromatic residues that are accessible for the surface interaction with AR LBD (Fig. S6*A*).

Based on the structure and sequence homology between the ES α1-helix and AR AF-1 helix, we generated a structural model of the ES/AR LBD complex, confining the surface contact of ES α1-helix to the AF-2 coactivator binding cleft in AR LBD (Fig. 4*D* and Fig. S6). Despite the simple superposition of ES α1-helix in human ES structure [Protein Data Bank (PDB) ID code 1BNL] over the FXXLF helical peptide bound to AR AF-2 (PDB ID code 1XOW), it yielded a model of ES/AR LBD complex with minimal clashes between side chains (Fig. S6*B*). Our model showed that ES α1-helix can mimic the FXXLF-motif binding to AR AF-2 by showing the side chains of Phe-31 and -34 in the ES helix faced to the hydrophobic core of the AF-2 binding cleft (Fig. 4*D*). However, because the model was built by rigid body movement, residues Arg-27 and -38 that bracket the ES α1-helix are responsible for side-chain clashes with AR AF-2. With regard to this interpretation, it is interesting to note that the known AR AF-1 motif (R20–R31) from the complex structure with AR LBD would also position Arg-20 and -31 around this AF-2 interaction site (17). These findings suggested that either rigid docking of ES helix to the AR LBD or cocrystal structure of AR LBD coupled with small peptides is limited by the inability to predict induced fit, and therefore some conformational flexibility may be necessary for the AR AF-2 site to accommodate either AF-1 or ES binding.

To validate the structural prediction that ES and AR NTD (or AR coactivators) may compete for AR AF-2, a peptide inhibition assay was performed. The AR20–30 peptide of AR NTD (residues 20–30) containing an FXXLF motif was used to mask the binding cleft of AF-2 in AR LBD (Fig. 4*C*). Based on prior studies that suggested this peptide binds with a K_D value of 1.2 μM to the AR LBD (21), peptide concentrations of 0.1–10 μM were tested in the experiment. We found that preincubation with 0.1–10 μM AR20–30 significantly reduced AR-LBD interaction with ES, resulting in >70–80% loss of binding to ES (Fig. 4*E*). Such inhibition by the peptide masking supported our model of ES interaction at the AF-2 coactivator binding interface in LBD. Interestingly, the binding of full-length AR to ES was decreased only by 40–50% at higher concentrations of peptide (Fig. 4*E*), suggesting in part that ES may also possess additional minor binding interface for another region of AR.

Phe-31 and -34 in ES Helix Play an Important Role in AR Binding. Structural modeling and the peptide inhibition studies suggested that putative ES-binding site includes AR AF-2, which provides

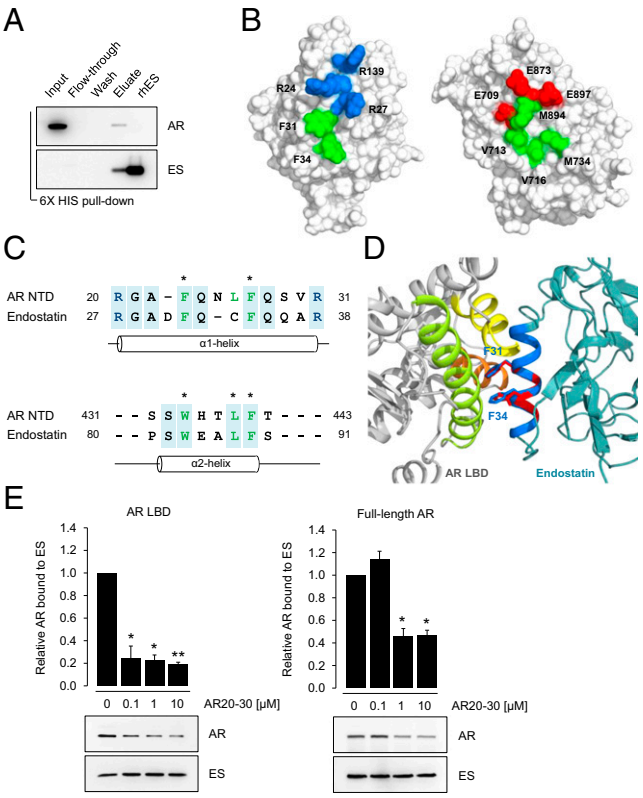

Fig. 4. ES binds to the AR AF-2 coactivator binding interface. (*A*) To demonstrate interaction of ES with AR LBD, purified ES was incubated with recombinant AR LBD. His-tag pull-down assay was carried out as described earlier. The concentrations of ES and AR LBD used in the assay were indicated as rhES and input, respectively. Approximately 20% of Eluate was loaded on a gel for immunoblotting. (*B*) Molecular surface representation of human ES (*Left*; PDB ID code 1BNL) and human AR LBD (*Right*; PDB ID code 1XOW). A positively charged cluster of ES (R24, R27, and R139) and a negatively charged cluster in AR LBD, including the residue E897 (AF-2 charge clamp), are colored in blue and red, respectively. Hydrophobic residues in ES α1-helix (F31 and F34) and AF-2 binding cleft are colored in green. (*C*) The sequences of ES and AR NTD were compared by aligning the α-helical secondary structure elements. The residues of noncanonical NR box (FXXLF and WXXLF) are shown in green, and identically matched residues are boxed in blue. Residues investigated in this study are marked by asterisks. (*D*) A structural model of ES–AR complex was built by superposing α1-helix in human ES (PDB ID code 1BNL) over the reference structure of AR20–30 peptide that interacts with AF-2 in AR LBD (PDB ID code 1XOW) (see also Fig. S6). ES α1-helix (residues 27–38) is shown as a blue ribbon, and AR20–30 helical peptide is colored in red. The model represents phenylalanine-rich ES α1-helix binding to AR AF-2, formed by helix 3 (H3; green ribbon), helix 4 (H4; orange), and helix 12 (H12; yellow). (*E*) Peptide inhibition assay. Masking of the AR AF-2 was carried out by preincubation of AR [full-length (*Right*) or LBD only (*Left*)] with 0.1–10 μM of AR20–30 peptide for 1 h. After the peptide inhibition, ES was applied to reaction mixture and incubated for additional 6–8 h. The levels of AR bound to ES were analyzed by His-tag pull-down assay. The interaction inhibited by the peptide is presented as a relative value (mean ± SEM) of control (100%) from two independent experiments. $*P < 0.05$; $**P < 0.01$ vs. control. Peptide inhibition on AR binding to ES indicates that the ES-binding interface overlaps with AR AF-2.

a binding platform for phenylalanine-rich ES α1-helix. Based on this model prediction, we further validated whether Phe-31 and -34 in the ES helix are critical for AR binding. For binding experiments, mutant forms of ES were generated by single amino acid substitution at Phe-31 and -34 to alanines (Fig. 5*A* and Table S1), and the ES antibody—recognizing amino acid residues 1–12 present in both wild-type and created mutant forms—was used for quantitative protein analysis. Compared with wild-type ES, bound

BIOCHEMISTRY

AR was reduced by 83.9% and 89.0% in the reactions with ES_{F31A} and ES_{F34A}, respectively ($P < 0.01$; Fig. 5*B*). In line with the result from pull-down assay, analysis of the ES–AR complex on a native gel also indicated 81.7% and 79.7% lower AR-binding abilities of ES_{F31A} and ES_{F34A}, respectively ($P < 0.01$; Fig. 5*C*). In addition, size-exclusion chromatography analysis exhibited coelution of AR with wild-type ES, whereas mutant forms of ES failed to form a complex with AR by showing peak separations between AR and mutated ES in the chromatogram (Fig. 5*D*). These results clearly indicated that ES binding to AR was significantly affected by substitution of aromatic side chains in the ES helix, suggesting that Phe-31 and -34 in the ES helix play an important role in AR binding. In accordance with binding assays, treatment with ES_{F31A} or ES_{F34} showed no significant growth inhibition of AR-positive LNCaP and C4-2B cells (Fig. 5*E*). These results provide direct evidence that the antiproliferative effect of ES is contributed by antagonistic action of ES on AR function via protein–protein interaction.

Discussion

Recent understanding of the role of AR in acquired resistance to antiandrogens among patients with CRPC compels a need to develop novel therapeutics capable of suppressing AR-associated tumor progression (2, 3). Particularly, a missense mutation (F876L) in the AR ligand-binding site has been reported to cause resistance to enzalutamide through an antagonist-to-agonist switch (1, 6, 30), indicating limitations in the use of small-molecule inhibitors for effective disruption of AR function. The functional activity of AR largely depends on ligand-dependent conformational change in AF-2 that accommodates coactivator binding. Therefore, instead of targeting the ligand-binding site, identifying biologically driven macromolecular inhibitors that fully occupy the AR AF-2 can be a viable alternative to current therapies.

In this context, the present study identified, to our knowledge, for the first time that ES directly binds to AR. Such a protein–protein interaction interrupts AR nuclear transport and transcriptional activation of downstream AR-target genes, thereby attenuating the AR-associated malignant phenotype. In line with experimental data, model-based functional studies on the ES/AR LBD complex confirmed that the putative binding site for ES overlaps with the AR AF-2 coactivator binding interface. Given the distinct binding preference of AR AF-2 for noncanonical NR box with bulky aromatic residues (20, 21), our structural analysis indicated a striking feature that ES contains α1-helix (R27–R38) and α2-helix (W83–F87) with amino acid sequences resembling the FXXLF and WXXLF motifs in the AR NTD (R20–R31 and W435–F439), respectively. Such a high sequence homology between the helices in ES and AR NTD suggests that ES can modulate AR function by mimicking the mode of coactivator binding or interaction between AR AF-1 with AF-2 interdomains. In agreement with the structural speculation, masking the AR AF-2 by using the synthetic peptide of AR AF-1 (R20–V30) significantly reduced the interaction of ES with AR LBD. Therefore, the molecular action of ES inhibiting AR transactivation may underlie the interruption of the AR N/C interaction as well as coactivator binding by occupying the AR AF-2.

Our study further confirms that the aromatic residues in ES α1-helix play a crucial role in AR binding. A site-directed mutagenesis study verified that ES interaction with AR was significantly reduced by the replacement of Phe-31 and -34 with alanines. The resultant decrease in AR binding substantially abolished the antagonistic action of ES on AR-mediated PCa cell growth, suggesting that the overall antiproliferative effect of ES on PCa cells is mainly attributed to the disruption of AR function via protein–protein interactions.

High sequence homology between ES α2-helix and the WXXLF motif in AR NTD also set our sights on Folkman's initial study harnessing an insoluble form of ES. This study demonstrated that delivery of insoluble ES directly into the xenograft tumors of Lewis lung carcinoma (LLC) exerted a profound antitumor effect, although the underlying mechanism remained unclear (8). Although aromatic side chains of Trp-83, Leu-86, and Phe-87 in α2-helix are embedded in the hydrophobic core (Fig. S6*A*), it is conceivable that insoluble ES, presumably due to lack of a proper folding, enables the bulky side chains of α2-helix (WXXLF) to be exposed for binding to AR AF-2. Indeed, disruption of ES folding, either by acid-induced unfolding or mutations on disulfide bonds, has been reported to increase α-helical content, suggesting that unfolded ES retains intrinsic α-helical secondary structures (31, 32). Another interesting aspect of the earlier studies is that satisfactory outcomes were predominantly reported when ES was tested in patients and animal models with lung cancer. Recent studies using recombinant ES also showed the strongest response in LLC and NSCLC (11–13). In this respect, it is noteworthy that elevated AR expression in the lung has been implicated in promoting the tumor development and progression (16, 33, 34). Thus, the potent tumor regression could also be attributed to AR antagonism in lung cancer, which may further provide an opportunity to revisit the unsolved molecular mechanism of insoluble ES.

In light of earlier preclinical and clinical studies demonstrating that high doses of ES with sustained administration is crucial for

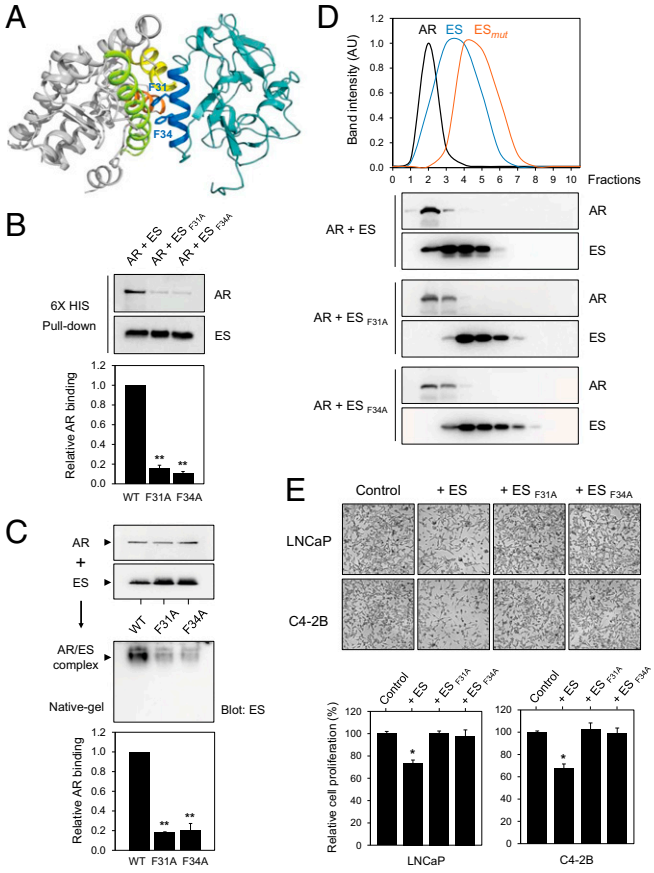

Fig. 5. Functional analyses of mutant forms of ES. (*A*) Single-point mutations (F31A and F34A) were generated to determine whether phenylalanine-rich ES α1-helix is critical for AR binding. (*B–D*) AR binding to wild-type and mutant forms of ES was compared by pull-down assay (*B*), native gel analysis (*C*), and size-exclusion chromatography (*D*). All results are expressed as mean ± SEM. $*P < 0.05$; $**P < 0.01$ vs. control. (*E*) Antiproliferative effect of ES mutants on LNCaP and C4-2B cells was compared with wild-type ES. The cell growth affected by 0.5 μM ES or ES mutants at 72 h is presented as a relative value (mean ± SD) compared with control as 100%. $*P < 0.05$ vs. control. Representative phase-contrast images of LNCaP and C4-2B cells are provided.

the tumor response (10–13), our results also indicated that a 5- to 10-fold higher concentration of ES is required for suppressing PCa cell growth, compared with IC_{50} on human umbilical vein endothelial cell (HUVEC) proliferation (Fig. 1*A* and Fig. S1). This observation further suggests that the mechanism of endostatin action may be different between HUVEC and PCa cells. Given the molecular action of ES targeting AR function, our results suggest that intracellular trafficking and cytosolic augmentation of ES may necessitate a high concentration of ES for inhibiting PCa cell proliferation (Fig. S7*A*). When exogenous supply of ES was stopped, we also found that intracellularly accumulated ES was cleared within 24 h in ES-treated LNCaP cells (Fig. S7*B*). This observation further supports our previous in vivo studies, indicating that the sustained systemic level of ES was more effective in exerting antitumor effects in a progressively developing mouse PCa model (15). With a short half-life of purified protein that requires high quantity of administration, a constant supply of ES through gene transfer would thus be an ideal approach to overcome the limitations.

The present study provides new insight into ES as an endogenous AR inhibitor whose antagonistic action could be used for suppressing CRPC. In addition, the intrinsic function of ES as an inhibitor of tumor-associated angiogenesis can synergize with the antitumor effects when applied to AR-associated malignancy. Therefore, pleiotropic anticancer activity of ES and its proven safety in clinical trials (11) could be incorporated in chemotherapy regimens as an adjuvant to reduce possibly the risk of developing chemotherapy-induced side effects by lowering drug dose. In this respect, the combination of ES with other AR-targeted chemotherapeutics using different target sites (i.e., antiandrogens) or different molecular mechanisms (i.e., taxanes) may be of particular interest. Further, the potential of ES binding to the common AR mutation (F876L) that arises as a survival mechanism to AR-targeted therapies (1, 6, 30) would greatly increase its utility in patients with CRPC. Recent studies also demonstrated that overexpression of glucocorticoid receptor (GR) up-regulates a number of AR target genes as a mechanism of developing resistance to enzalutamide (3, 35). Interestingly, AF-2 coactivator binding interface, the putative ES-binding site identified in this study, is structurally conserved between AR and GR (20, 36). Therefore, these observations further provide a great opportunity to explore the possibility of ES, targeting the compensatory action of GR upon AR antagonism. Further in vivo validation in line with our previous studies on the potential of ES and results of the present study should enable translating this novel AR-targeted therapy for CRPC.

Materials and Methods

Preparation of native and mutant forms of ES is described in *SI Materials and Methods*. A detailed description of structural modeling of the ES/AR–LBD complex, binding assays (His-tag pull-down, coimmunoprecipitation, native-PAGE, and size-exclusion chromatography), yeast-two hybridization, and in vitro experiments (cell culture assays, immunocytochemistry, and molecular analyses) can also be found in *SI Materials and Methods*.

ACKNOWLEDGMENTS. We thank Patrick Hwang for providing technical support and the University of Alabama at Birmingham (UAB) Peptide Synthesis Core Facility and UAB Center for AIDS Research DNA Sequencing Core. This work was supported by National Institutes of Health Grants CA132077, CA133737, GM97052; and Department of Defense Grant DoD-BC101411.

1. Korpal M, et al. (2013) An F876L mutation in androgen receptor confers genetic and phenotypic resistance to MDV3100 (enzalutamide). *Cancer Disc* 3(9):1030–1043.
2. Shafi AA, Yen AE, Weigel NL (2013) Androgen receptors in hormone-dependent and castration-resistant prostate cancer. *Pharmacol Ther* 140(3):223–238.
3. Ferraldeschi R, Welti J, Luo J, Attard G, de Bono JS (2014) Targeting the androgen receptor pathway in castration-resistant prostate cancer: Progresses and prospects. *Oncogene*, 10.1038/onc.2014.115.
4. Yuan X, Balk SP (2009) Mechanisms mediating androgen receptor reactivation after castration. *Urol Oncol* 27(1):36–41.
5. Chen CD, et al. (2004) Molecular determinants of resistance to antiandrogen therapy. *Nat Med* 10(1):33–39.
6. Joseph JD, et al. (2013) A clinically relevant androgen receptor mutation confers resistance to second-generation antiandrogens enzalutamide and ARN-509. *Cancer Disc* 3(9):1020–1029.
7. Marneros AG, Olsen BR (2005) Physiological role of collagen XVIII and endostatin. *FASEB J* 19(7):716–728.
8. O'Reilly MS, et al. (1997) Endostatin: An endogenous inhibitor of angiogenesis and tumor growth. *Cell* 88(2):277–285.
9. Skovseth DK, Veuger MJ, Sorensen DR, De Angelis PM, Haraldsen G (2005) Endostatin dramatically inhibits endothelial cell migration, vascular morphogenesis, and perivascular cell recruitment in vivo. *Blood* 105(3):1044–1051.
10. Thomas JP, et al. (2003) Phase I pharmacokinetic and pharmacodynamic study of recombinant human endostatin in patients with advanced solid tumors. *J Clin Oncol* 21(2):223–231.
11. Fu Y, Tang H, Huang Y, Song N, Luo Y (2009) Unraveling the mysteries of endostatin. *IUBMB Life* 61(6):613–626.
12. Kisker O, et al. (2001) Continuous administration of endostatin by intraperitoneally implanted osmotic pump improves the efficacy and potency of therapy in a mouse xenograft tumor model. *Cancer Res* 61(20):7669–7674.
13. Sauter BV, Martinet O, Zhang WJ, Mandeli J, Woo SL (2000) Adenovirus-mediated gene transfer of endostatin in vivo results in high level of transgene expression and inhibition of tumor growth and metastases. *Proc Natl Acad Sci USA* 97(9):4802–4807.
14. Abdollahi A, et al. (2007) Transcriptional network governing the angiogenic switch in human pancreatic cancer. *Proc Natl Acad Sci USA* 104(31):12890–12895.
15. Isayeva T, Chanda D, Kallman L, Eltoum IE, Ponnazhagan S (2007) Effects of sustained antiangiogenic therapy in multistage prostate cancer in TRAMP model. *Cancer Res* 67(12):5789–5797.
16. Chang C, Lee SO, Yeh S, Chang TM (2014) Androgen receptor (AR) differential roles in hormone-related tumors including prostate, bladder, kidney, lung, breast and liver. *Oncogene* 33(25):3225–3234.
17. He B, et al. (2004) Structural basis for androgen receptor interdomain and coactivator interactions suggests a transition in nuclear receptor activation function dominance. *Mol Cell* 16(3):425–438.
18. He B, Wilson EM (2002) The NH(2)-terminal and carboxyl-terminal interaction in the human androgen receptor. *Mol Genet Metab* 75(4):293–298.
19. Bai S, He B, Wilson EM (2005) Melanoma antigen gene protein MAGE-11 regulates androgen receptor function by modulating the interdomain interaction. *Mol Cell Biol* 25(4):1238–1257.
20. Hur E, et al. (2004) Recognition and accommodation at the androgen receptor coactivator binding interface. *PLoS Biol* 2(9):E274.
21. He B, Wilson EM (2003) Electrostatic modulation in steroid receptor recruitment of LXXLL and FXXLF motifs. *Mol Cell Biol* 23(6):2135–2150.
22. Hohenester E, Sasaki T, Olsen BR, Timpl R (1998) Crystal structure of the angiogenesis inhibitor endostatin at 1.5 A resolution. *EMBO J* 17(6):1656–1664.
23. Ding YH, et al. (1998) Zinc-dependent dimers observed in crystals of human endostatin. *Proc Natl Acad Sci USA* 95(18):10443–10448.
24. Chura-Chambi RM, Genova LA, Affonso R, Morganti L (2008) Refolding of endostatin from inclusion bodies using high hydrostatic pressure. *Anal Biochem* 379(1):32–39.
25. Huang X, et al. (2001) Soluble recombinant endostatin purified from Escherichia coli: Antiangiogenic activity and antitumor effect. *Cancer Res* 61(2):478–481.
26. Dhanabal M, et al. (1999) Endostatin induces endothelial cell apoptosis. *J Biol Chem* 274(17):11721–11726.
27. Wickström SA, Alitalo K, Keski-Oja J (2002) Endostatin associates with integrin alpha5beta1 and caveolin-1, and activates Src via a tyrosyl phosphatase-dependent pathway in human endothelial cells. *Cancer Res* 62(19):5580–5589.
28. Isayeva T, Moore LD, Chanda D, Chen D, Ponnazhagan S (2009) Tumoristatic effects of endostatin in prostate cancer is dependent on androgen receptor status. *Prostate* 69(10):1055–1066.
29. Lee DK, Chang C (2003) Endocrine mechanisms of disease: Expression and degradation of androgen receptor: Mechanism and clinical implication. *J Clin Endocrinol Metab* 88(9):4043–4054.
30. Balbas MD, et al. (2013) Overcoming mutation-based resistance to antiandrogens with rational drug design. *eLife* 2:e00499.
31. Li B, Wu X, Zhou H, Chen Q, Luo Y (2004) Acid-induced unfolding mechanism of recombinant human endostatin. *Biochemistry* 43(9):2550–2557.
32. Zhou H, Wang W, Luo Y (2005) Contributions of disulfide bonds in a nested pattern to the structure, stability, and biological functions of endostatin. *J Biol Chem* 280(12):11303–11312.
33. Mikkonen L, Pihlajamaa P, Sahu B, Zhang FP, Jänne OA (2010) Androgen receptor and androgen-dependent gene expression in lung. *Mol Cell Endocrinol* 317(1-2):14–24.
34. Recchia AG, et al. (2009) A cross-talk between the androgen receptor and the epidermal growth factor receptor leads to p38MAPK-dependent activation of mTOR and cyclinD1 expression in prostate and lung cancer cells. *Int J Biochem Cell Biol* 41(3):603–614.
35. Arora VK, et al. (2013) Glucocorticoid receptor confers resistance to antiandrogens by bypassing androgen receptor blockade. *Cell* 155(6):1309–1322.
36. Centenera MM, Harris JM, Tilley WD, Butler LM (2008) The contribution of different androgen receptor domains to receptor dimerization and signaling. *Mol Endocrinol* 22(11):2373–2382.

Published OnlineFirst January 30, 2015; DOI: 10.1158/1541-7786.MCR-14-0492

Cell Death and Survival

Molecular Cancer Research

Variants of Osteoprotegerin Lacking TRAIL Binding for Therapeutic Bone Remodeling in Osteolytic Malignancies

Jerome T. Higgs[1], John S. Jarboe[2,3], Joo Hyoung Lee[1], Diptiman Chanda[1], Carnellia M. Lee[1], Champion Deivanayagam[4], and Selvarangan Ponnazhagan[1]

Abstract

Osteolytic bone damage is a major cause of morbidity in several metastatic pathologies. Current therapies using bisphosphonates provide modest improvement, but cytotoxic side effects still occur prompting the need to develop more effective therapies to target aggressive osteoclastogenesis. Increased levels of receptor activator of NF–κB ligand (TNFSF11/RANKL), leading to RANKL-RANK signaling, remain the key axis for osteoclast activation and bone resorption. Osteoprotegerin (TNFRSF11B/OPG), a decoy receptor for RANKL, is significantly decreased in patients who present with bone lesions. Despite its potential in inhibiting osteoclast activation, OPG also binds to TNF-related apoptosis-inducing ligand (TNFSF10/TRAIL), making tumor cells resistant to apoptosis. Toward uncoupling the events of TRAIL binding of OPG and to improve its utility for bone remodeling without inducing tumor resistance to apoptosis, OPG mutants were developed by structural homology modeling based on interactive domain identification and by superimposing models of OPG, TRAIL, and its receptor DR5 (TNFRSF10B) to identify regions of OPG for rational design. The OPG mutants were purified and extensively characterized for their ability to decrease osteoclast damage without affecting tumor apoptosis pathway both *in vitro* and *in vivo*, confirming their potential in bone remodeling following cancer-induced osteolytic damage.

Implications: OPG variants were developed that lack TRAIL binding, yet retain RANKL binding and suggest new possibilities for therapeutic targeting in osteolytic malignancies. *Mol Cancer Res; 13(5); 819–27. ©2015 AACR.*

Introduction

The therapeutic potential of OPG in bone remodeling has been of great interest in the last decade. Human OPG is composed of 401 amino acids with a molecular weight of approximately 60 kDa. Structurally, OPG consists of four cysteine-rich pseudorepeats at the N-terminus, two death domains, a heparin-binding site at the C-terminus, and a 21-amino acid signal peptide (1, 2). The importance of OPG as a negative regulator of osteoclastogenesis is evident from studies with transgenic mice where overexpression of OPG has been shown to cause severe osteopetrosis and reduce the number of mature osteoclasts, while OPG gene knockout leads to osteoporosis (3). This understanding led to the use of OPG as a potential therapeutic molecule for various diseases, including glucocorticoid-induced osteoporosis, rheumatoid arthritis, vascular calcification, and osteolytic malignancies (1, 4–6).

The key regulators of bone remodeling in respect to osteoclast biology belong to the TNF superfamily. Activation and maturation of osteoclasts result from the binding of receptor activator of NF-κB ligand (RANKL) to its receptor RANK, found on osteoclasts and osteoclast precursor cells of monocyte lineage (3, 7, 8). Osteoprotegerin, which is a soluble glycoprotein, is a member of the TNF receptor family and acts as a decoy receptor by binding RANKL with a higher affinity than RANK, thus neutralizing the RANK–RANKL interaction and ultimately osteoclastogenesis (8).

Despite its potential as a possible molecule for therapeutic targeting of osteolytic damage in bone metastasis, OPG also acts as a receptor for the cytotoxic ligand, TRAIL, thereby conferring resistance to tumor cell apoptosis. Thus, although OPG can effectively block osteoclastogenesis, it also promotes tumor cell survival by impairing TRAIL function. To overcome this limitation and to improve the clinical utility of OPG for bone remodeling in osteolytic malignancies, the current study sought to uncouple these two properties of OPG. By using structural homology modeling of OPG, RANKL, and TRAIL, we have identified, developed, and validated genetic mutants of OPG, lacking TRAIL binding but preserving RANKL binding. The OPG-mutants were first functionally characterized *in vitro* to demonstrate selective inhibition of RANKL-mediated osteoclastogenesis, and then their low binding affinity to TRAIL facilitating caspase-3–induced apoptosis of tumor cells upon treatment with TRAIL. Furthermore, *in vivo* validation of two such OPG mutants, in a preclinical mouse model of a bone-disseminated osteolytic tumor, demonstrated their potential in restoring bone remodeling. The two novel OPG variants will be promising for therapeutic targeting of

[1]Department of Pathology, The University of Alabama at Birmingham, Birmingham, Alabama. [2]Department of Biochemistry, The University of Alabama at Birmingham, Birmingham, Alabama. [3]Department of Radiation Oncology, The University of Alabama at Birmingham, Birmingham, Alabama. [4]Department of Vision Sciences, The University of Alabama at Birmingham, Birmingham, Alabama.

Corresponding Author: Selvarangan Ponnazhagan, The University of Alabama at Birmingham, 1825 University Boulevard, SHEL 814, Birmingham, AL 35294. Phone: 205-934-6731; Fax: 205-975-4919; E-mail: pons@uab.edu

doi: 10.1158/1541-7786.MCR-14-0492

Published OnlineFirst January 30, 2015; DOI: 10.1158/1541-7786.MCR-14-0492

aggressive osteoclast-induced bone damage and associated morbidity in several osteolytic malignancies.

Materials and Methods

Modeling of OPG–TRAIL complex

The structural model of OPG/TRAIL complex was generated by superimposition of human TRAIL monomer (PDB code: 1D4V) onto human RANKL/OPG complex structure (PDB code: 3URF) using human RANKL monomer as a reference structure. The generated model includes binding interface between a monomer of OPG and two monomers of trimeric ligands. Rigid body movement and model analysis were carried out using both UCSF Chimera (9) and Coot (10), and all figures were made with the PyMol program (http://www.PyMol.org).

Cell lines and reagents

The human osteolytic prostate cancer cell line PC3, expressing firefly luciferase, (a kind gift from Dr. Kenneth J. Pienta, University of Michigan, Ann Arbor, MI), was maintained in RPMI-1640 medium (Mediatech Inc) supplemented with 10% FBS (Mediatech Inc.) and penicillin/streptomycin (Mediatech Inc). The murine macrophage cell line, RAW-264.7, was maintained in DMEM supplemented with 10% FBS, 4 mmol/L L-glutamine, 1% antibiotics, and 10% macrophage colony-stimulating factor [M-CSF, a kind gift from Dr. Xu Feng, The University of Alabama (UAB) at Birmingham, AL]. The human melanoma cell line MDA-MB-435 was maintained in 50% DMEM, 50% DMEM F12, 1% penicillin/streptomycin, 10% FBS, and nonessential amino acids. HEK-293 cells were purchased from ATCC and maintained in DMEM supplemented with 10% new born calf serum and 1% penicillin-streptomycin. The proliferation index of PC3 cells was determined by CellTiter 96 AQueous One Solution Cell Proliferation Assay Kit (Promega Corporation) as recommended by the manufacturer. Recombinant OPG was purchased from R&D Systems and recombinant TRAIL was purchased from Millipore. Purified RANKL was a kind gift from Dr. Xu Feng, UAB. Transfections were performed using Purefection reagent (System Bioscience).

Animal use and care

Athymic nude mice (nu/nu), 6- to 8 weeks of age, were purchased from Frederick National Laboratory-NCI Frederick and housed in the animal facility at UAB. Animal care and treatments were conducted in accordance with established guidelines and protocols approved by the University of Alabama at Birmingham Institutional Animal Care and Use Committee.

Cloning of OPG expression vector

The recombinant OPG used in this study for creating genetic variants was composed of the ligand-binding domain of human OPG (1-201 amino acids), fused to the Fc domain of human IgG. The OPG-Fc fusion gene was isolated from an adenoviral construct (kindly provided by Dr. Joanne Douglas, UAB) and subcloned into pcDNA3.1 under control of the CMV promoter by directional subcloning using BamH1 restriction site. The recombinant plasmids were verified for proper orientation by restriction digestion, and the open-reading frame (ORF) by DNA sequencing at the UAB Center for AIDS Research DNA Sequencing Core.

Site-directed mutagenesis

The OPG mutants (Y49R, N81A, F96A, and F107A) were generated based on putative OPG residues identified from structural model of OPG–TRAIL complex. The sequences of primers used for mutagenesis are given in Table 1. Site-directed mutagenesis was performed using Quickchange XL Kit (Stratagene) and *PfuTurbo* DNA Polymerase (Stratagene) as per the manufacturer's instructions with a "touch-down" PCR protocol as follows: after an initial denaturation step at 95°C for 2 minutes, cycles were performed at 95°C denaturation for 50 seconds, followed by annealing at 65°C, and extension at 72°C for 2 minutes per kilobase pair of template DNA. The annealing step was reduced by 1°C for 10 cycles until an annealing temperature of 55°C was reached. Eight more cycles were then repeated at an annealing temperature of 55°C for a total of 18 cycles. A final extension step at 72°C was then performed and the reaction mix was digested with restriction enzyme DpnI to remove the template DNA. Five microliters of the reaction mix were then transformed into One-Shot Top10 competent cells (Invitrogen) and plated onto agar containing 100 μg/mL ampicillin. Clones were screened for the identification of respective mutations by DNA sequencing. All DNA sequencing was performed at the UAB Center for AIDS Research DNA Sequencing Core.

Expression of recombinant OPG proteins

HEK-293 cells were transfected with either OPG^{wt} or OPG^{mut} (Y49R, N81A, F96A, and Y107A) plasmid constructs individually. Forty-eight hours after transfection, culture media were collected and concentrated using a 30 kDa cut-off centrifugal filter unit (Amicon). The expression of recombinant OPGs in the culture media were analyzed by Western blot analysis using antibodies against OPG (R&D Systems, Inc.) and Fc (Sigma-Aldrich).

Osteoclast assay

Primary murine macrophage cells were cultured in 48-well dishes at a density of 2×10^4 cells per well. Cells were allowed 24 hours to attach at which point 200 ng of recombinant OPG, OPG^{wt}, or OPG^{mut} were added to individual wells in combination with or without 60 ng of purified RANKL. The medium was changed every 48 hours with fresh supplementation of OPG and RANKL. The cultures were maintained for 10 days following

Table 1. Sequences of primers used for site-directed mutagenesis

OPG-Y49R	5′-CCCTTGCCCTGACCACTACCGCACAGACAGCTGGCACACC-3′ Forward
	5′-GGTGTGCCAGCTGTCTGTGCGGTAGTGGTCAGGGCAAGGG-3′ Reverse
OPG-N81A	5′-GAGTGCAATCGCACCCACGCCCGCGTGTCG-3′ Forward
	5′-GCATTCGCACACGCGGGCGTGGGTGCGA-3′ Reverse
OPG-F96A	5′-GGGCGCTACCTTGAGATAGAGGCCTGCTTGAAACATAGGAGCTGC-3′ Forward
	5′-GCAGCTCCTATGTTTCAAGCAGGCCTCTATCTCAAGGTAGCGCCC-3′ Reverse
OPG-F107A	5′-GGAGCTGCCCTCCTGGAGCTGGAGTGGTGCAAGCTGG-3′ Forward
	5′-CCAGCTTGCACCACTCCAGCTCCAGGAGGGCAGCTCC-3′ Reverse

Published OnlineFirst January 30, 2015; DOI: 10.1158/1541-7786.MCR-14-0492

which tartrate-resistant acid phosphotase (TRAP) staining was carried out to identify multinucleated TRAP-positive osteoclasts. While assessing under light microscope, 10 fields of view were randomly selected to quantify the number of osteoclasts.

Cell proliferation assay

MDA-MB-435 cells were cultured in 96-well dishes at a density of 4×10^4 cells per well. Twenty-four hours later, 100 ng of recombinant TRAIL was added to each well in combination with 200 ng of recombinant OPG, OPG^{wt}, or OPG^{mut}. After 48 hours, the cells were fixed in 3.7% paraformaldehyde and stained with 0.05% crystal violet (Sigma) for 30 minutes and analyzed under a light microscope (×100). In addition, from replicate cultures, cell proliferation was determined 48 hours later using 3-(4,5-dimethylthiazol-2-yl)-5-(3-carboxymethoxyphenyl)-2-(4-sulfophenyl)-2H-tetrazolium, inner salt (MTS) and then colorimetrically measured at 490 nm. The assay was performed three times independently.

TRAIL-mediated apoptosis

To demonstrate further that TRAIL binding to OPG^{wt} and not OPG^{mut} was responsible for apoptosis induction in cancer cells, downstream caspase activity was determined following TRAIL and OPG treatments as above. Briefly, the human osteolytic prostate cancer cell line, PC3 was cultured in 60-mm dishes at 10^6 cells per dish and allowed to adhere for 24 hours. Combinations of 100 ng of recombinant TRAIL and 200 ng of recombinant OPG, OPG^{wt}, or OPG^{mut} were added to the cells and cultured for additional 3 hours. The cells were then harvested and lysed using cell culture lysis reagent (Promega). Cell lysates were tested by Western blot analysis using cleaved caspase-3 antibody (Santa Cruz Biotechnology Inc.).

Development of genetically engineered human mesenchymal stem cells for cell therapy

Human mesenchymal stem cells (MSC) were isolated from surgical bone marrow transplant remnants of healthy donors from UAB following an Institutional Review Board-approved protocol. The cells were cultured in DMEM, 10% FBS, and 1% penicillin-streptomycin to confluence for cell sorting. Upon FACS analysis for positive MSC surface markers CD44, CD73, CD90 and after verifying the pluripotency by lineage differentiation into adipocytes, chondrocytes, and osteoblasts (11), MSCs were transfected with pcDNA-$OPG^{wt/mut}$ expression vectors using purefection reagent (Systems Bioscience) as per the manufacturer's instructions. Media from MSC, transfected with OPG^{wt} or OPG^{mut} (Y49R or F107A) constructs were collected and concentrated using a 30-kDa filter and analyzed by Western blotting using OPG and Fc antibodies.

Therapeutic potential of genetically engineered MSC expressing OPG^{mut} (Y49R and F107A), in a mouse model of tumor-induced osteolysis *in vivo*

Athymic nude mice were injected intra-tibially with approximately 1×10^5 human osteolytic prostate cancer line, PC3, constitutively expressing firefly luciferase. Twenty-four hours later, noninvasive imaging was performed to confirm implantation of the cells within the tibia and mice were injected with approximately 3×10^5 MSC, transfected with either OPG^{wt} or OPG^{mut} (Y49R or F107A) in the same tibia. Similar cohorts of mice were also used to test the therapeutic potential of MSC, engineered to express OPG^{wt} or OPG^{mut}, through systemic administration following implantation of PC3 cells in the tibia. In this group of experiment, 24 hours after implantation of PC3 cells in tibia, 3×10^5 MSC-$OPG^{wt/mut}$ were systemically administered through tail vein. Mice from both routes of MSC administration were noninvasively imaged for tumor growth based on luciferase expression up to 14 days post MSC therapy and sacrificed for analysis of osteolytic damage and bone remodeling.

Micro-computed tomograph analysis of bone tissue

Superficial CT scanning of the tibiae was performed on bone tissues using micro-CAT II (Imtek Inc.). For the determination of the three-dimensional architecture of trabecular bone, mice were sacrificed, tibiae harvested, and then analyzed in an advanced micro-CT instrument (μCT 40, Scanco Medical AG). Two scans were performed on each tibia, one for whole tibial bone with 16-μm resolution and one for trabecular analysis with a 6-μm resolution. A three-dimensional reconstruction of the images was created with the region of interest consisting of the trabecular area under the growth plate. The scan of the trabecular bone was performed beginning 25 slices below the growth plate and 100 slices were used for analysis and 3D reconstruction.

Statistical analysis

Significance levels of the experimental data were determined by Student *t* test and *P* values less than 0.05 were considered as statistically significant.

Results

Development of genetically engineered OPG variants

Toward developing OPG variants that lack TRAIL binding, yet retain RANKL binding, the binding interface of OPG with RANKL and TRAIL was structurally aligned. Because the crystal structure of OPG/TRAIL complex was not available, we generated the structural model of OPG/TRAIL complex by rigid body movement to the homologous structure. The RANKL/OPG complex (PDB code: 3URF) was utilized as a reference structure where the structure of TRAIL monomer from TRAIL/DR5 complex (PDB code: 1D4V) was superimposed onto RANKL (rms = 0.735, Fig. 1A). The generated model of OPG/TRAIL complex was then analyzed by using Coot and UCSF Chimera modeling softwares, which further helped in the identification of putative interaction sites between TRAIL, RANKL, and OPG (Fig. 1B and 1C). The most striking difference between RANKL and TRAIL was an amino acid loop that showed possible interactions of TRAIL and OPG (Fig. 1A). Analysis of the model indicated that the amino acid loop of TRAIL may interact with OPG in a similar manner as it interacted with DR5. A close-up view of the amino acid loop indicated that residues Y49 and N81 in OPG shared a similar mode of interaction with TRAIL as the respective conserved residues in DR5. However, F107 appeared to be projecting away from the loop. There also appeared to be possible contacts with Q95 and F96 in the 90s loop of OPG. None of these interactions appeared to take place with RANKL. These observations suggest that the OPG-binding interface may include amino acid residues Y49, N81, F96, and F107 that potentially interact with TRAIL (Fig. 1C). To test this

Published OnlineFirst January 30, 2015; DOI: 10.1158/1541-7786.MCR-14-0492

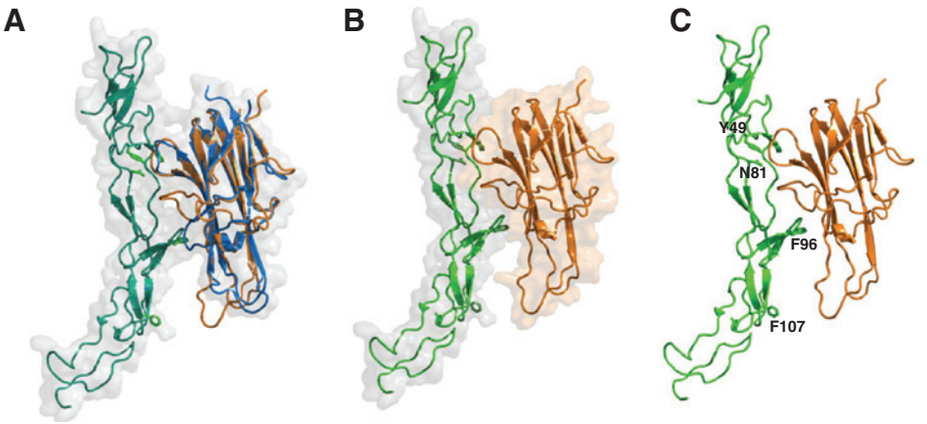

Figure 1.
Structure model of OPG–TRAIL complex. Superposition of human TRAIL (orange) with human RANKL (blue)–OPG (green) complex using a RANKL monomer as a reference (A), surface diagram of TRAIL (orange) and OPG (green; B), and putative OPG residues (in green) interacting with TRAIL (C) are shown. Designated amino acid residues (Y49, N81, F96, and F107) were subjected to site-directed mutagenesis. Ribbon and surface diagrams were created with the PyMol program.

hypothesis, the above residues were substituted to Y49R, N81A, F96A, and F107A to create individual OPG-mutant ORF.

Expression, purification and characterization of OPG mutants

To produce OPG mutants in a eukaryotic expression system, the ORF of OPG was subcloned in pcDNA3.1 vector together with the Fc portion of human immunoglobulin molecule as a fusion protein at the C-terminus to enhance the stability of recombinant proteins. Site-directed mutagenesis was performed using this OPG construct and primers corresponding to single point mutations in putative TRAIL-binding sites of OPG (Y49R, N81A, F96A, and F107A). Following verification by sequence analysis of both the DNA strands, plasmids encoding OPG^{wt} and OPG^{mut} were transfected into HEK-293 cells. The supernatants from plasmid-transfected cells, containing OPG^{wt} and OPG^{mut}, were concentrated and analyzed by SDS-PAGE to confirm the molecular mass at the expected size. As a measure of loading control for the culture supernatants, identical volume of conditioned media from OPG^{wt} and OPG^{mut} plasmid-transfected HEK-293 cells were resolved in SDS-PAGE and the gel was stained with Coomassie Blue. Results, confirming concentration of proteins between samples is shown in Fig. 2A. Immunoblotting with OPG and Fc antibodies confirmed the specificity of the proteins in monomeric and dimeric configurations (Figs. 2B and C).

OPG mutants inhibit RANKL-induced osteoclastogenesis

To determine the ability of OPG mutants to inhibit osteoclastogenesis, RAW-264.7 cells were cultured in the presence of RANKL, and OPG^{wt} or OPG^{mut}. Results of TRAP staining indicated the appearance of large, multinucleated osteoclasts in RAW-264.7 cell cultures with RANKL only (Fig. 3A). Cultures with RANKL and recombinant OPG or OPG^{wt} and RANKL resulted in no osteoclast differentiation, as expected. Interestingly, in cultures containing OPG^{mut} proteins, there was also a significant reduction in the formation of osteoclasts even in the presence of RANKL, confirming that the genetically engineered OPG mutants were functionally active in inhibiting osteoclast formation by retaining RANKL-binding affinity. Quantitative analysis of osteoclasts from different culture conditions indicated a statistically significant difference in osteoclast formation between RANKL-treated controls and those treated with recombinant wild-type or mutant OPG, in combination with RANKL (Fig. 3B).

OPG mutants do not interfere with TRAIL-induced apoptosis of cancer cells

After confirming that the OPG-mutants effectively inhibited osteoclastogenesis, they were assessed for interference with TRAIL-mediated apoptosis of cancer cells. Supernatants containing OPG^{mut} were concentrated using a 30-kDa filter and tested in MDA-MB-435 cells, in the presence or absence of recombinant human TRAIL. MDA-MB-435 cells were used in this study as they express the TRAIL receptor, DR5, and have been shown to be sensitive to TRAIL (12, 13). Results of the study indicated that MDA-MB-435 cells underwent cell death when cultured with TRAIL. Conversely, OPG^{wt} inhibited cytotoxic effects of TRAIL as proliferation of cancer cells was found to be comparable with untreated cells (Fig. 4A). While analyzing the mutants for blocking TRAIL-induced apoptosis, the mutant N81A appeared to bind to TRAIL, inhibiting its apoptosis-inducing property, as MDA-MB-435 cells demonstrated resistance to TRAIL treatment. However, OPG-mutants Y49R, F96A, and F107A showed abolished TRAIL binding with a significant decrease in cell proliferation and increased cell apoptosis (Fig. 4B). The MDA-MB-435 cells, cultured with recombinant OPG, OPG-wt, and OPG^{mut} N81A indicated that these two forms of OPG retained intact TRAIL binding, and inhibited TRAIL-mediated apoptosis leading to cell survival (Fig. 4B). To determine the downstream signaling pathway for TRAIL-induced apoptosis, MDA-MB-435 cells were cultured with OPG^{wt} or OPG^{mut} (Y49R or F107A) and TRAIL to determine activation of cleaved caspase-3 for apoptotic cell death. Western blot analysis confirmed that OPG mutants (Y49R and F107A) did not interfere with TRAIL-mediated apoptosis, as shown in Fig. 4C.

Osteoprotegerin mutants Y49R and F107A demonstrated bone protection from cancer-induced osteolysis *in vivo*

After determining the biologic activity of the OPG-mutants *in vitro*, based on the results from osteoclast and TRAIL assays, we sought to determine the effects of mutant Y49R and F107A (which demonstrated highest activity in RANKL binding and TRAIL-mediated apoptosis) in bone remodeling following cancer-induced osteolysis *in vivo*. A genetically engineered stem cell therapy approach was used to deliver the OPG-mutant proteins (Y49R and F107A) *in vivo* in a therapy model of bone-disseminated human osteolytic prostate cancer in mouse. Cohorts of male athymic nude mice were challenged intra-tibially with a

Published OnlineFirst January 30, 2015; DOI: 10.1158/1541-7786.MCR-14-0492

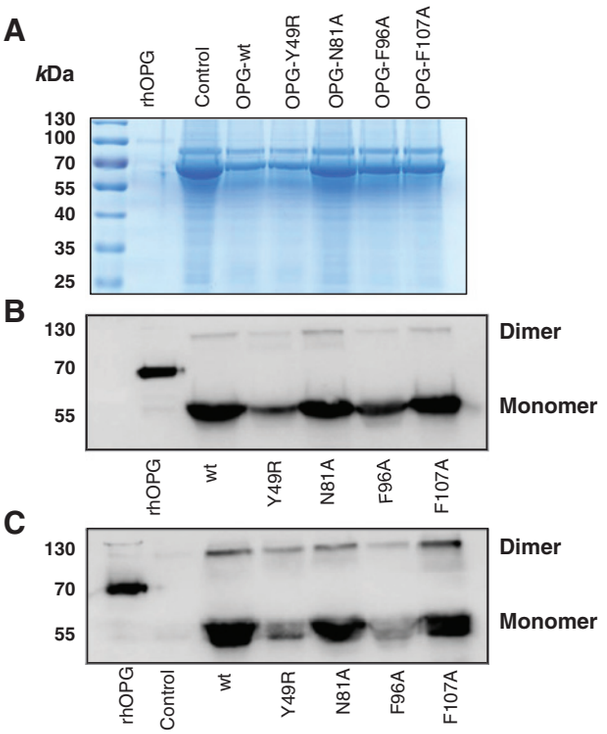

Figure 2.
Immunoblot analysis of purified OPG mutants. Forty-eight hours following transfection of expression plasmids containing the sequences of OPG-wt and OPG-mutants in HEK-293 cells, supernatant media were collected and concentrated using a 30 kDa filter. The concentrated media were then separated in a SDS-PAGE and transferred to nitrocellulose membrane. Loading control was assessed by Coomassie Blue staining (A) and detection of OPG-wt and OPG mutants was performed using antibodies for IgG (B) and OPG (C).

human osteolytic prostate cancer cell line PC3, constitutively expressing firefly luciferase. Following confirmation of engraftment of the tumor cells by noninvasive imaging, human MSC, transfected with expression vectors encoding OPG^{wt} or OPG^{mut} (Y49R or F107A), were injected in the same tumor microenvironment within the tibia or systemically via tail vein. Mice were sacrificed on day 14 post MSC therapy and tibiae were isolated for micro-CT analysis. Results of this analysis confirmed significant bone destruction in the naïve group that received PC3 cells only. However, mice treated with either OPG^{wt} or OPG^{mut} (Y49R or F107A) demonstrated a significant increase in trabecular bone architecture and trabecular connectivity density as compared with the control group both by intratumoral and systemic administration of genetically engineered MSC, expressing OPG^{mut} thereby providing evidence that the developed OPG mutants Y49R and F107A were therapeutically effective *in vivo* against cancer-induced osteolytic bone damage (Fig. 5A and B).

Discussion

Osteoclasts are the primary cells for physiologic and pathologic bone resorption during bone remodeling, and RANKL is critically involved in the differentiation, activation, and survival of these cells upon binding to its specific receptor RANK and inducing osteoclast differentiation of progenitor macrophages (7, 14). Increased expression of RANKL with certain malignancies, including breast cancer, prostate cancer, and multiple myeloma, causes activation of osteoclasts and remains an important mechanism in the formation of osteolytic bone lesions (15–17). The RANKL-RANK signaling axis, therefore, has become an important target for therapeutic intervention of osteolytic bone pathology. On the basis of the potent inhibitory actions of OPG on osteoclast differentiation and function, the therapeutic application of OPG in treatment of metastatic bone destruction has been recently studied (18–22). The outcome of phase I clinical trial using purified OPG in patients with multiple myeloma and breast cancer indicated that OPG was well tolerated and that a single dose suppressed levels of bone resorption markers, comparable to treatment with pamidronate (23). Thus, improving the biologic properties of OPG by uncoupling its TRAIL-binding ability will provide a crucial advancement in the utility of OPG for treatment of osteolytic malignancies. Results from the present study indicate that the two novel OPG variants, Y49R and F107A, indeed show a positive effect in bone remodeling following cancer-induced

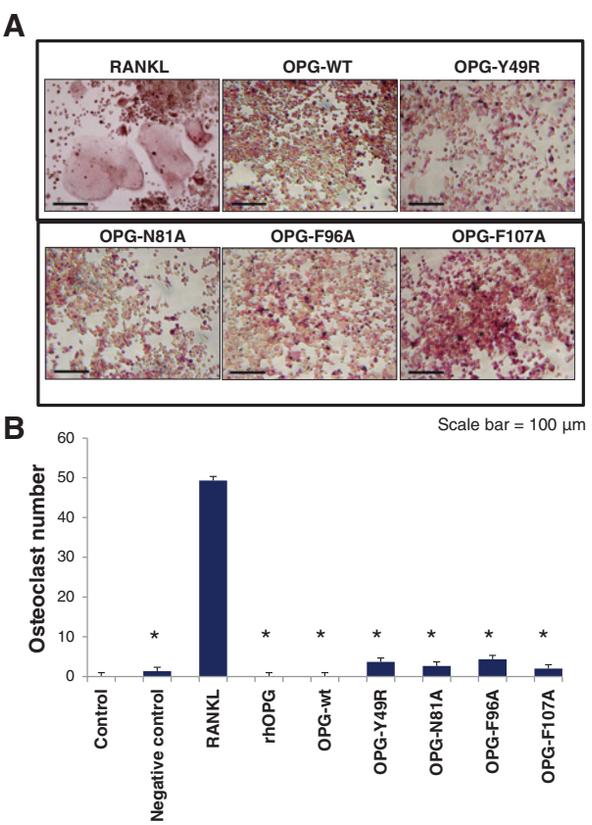

Figure 3.
Osteoclast assay to determine retention of RANKL binding of OPG mutants. Primary macrophage cells were cultured in the presence of 200 ng of recombinant OPG, OPG-wt, or indicated OPG mutants in the presence or absence of 60 ng of recombinant RANKL. As a positive control, macrophage cells were cultured with RANKL alone. TRAP staining of macrophage cell cultures were performed 7 to 14 days after cells were cultured in the presence of OPG-wt or OPG-mutants and RANKL (A). Quantitative analysis based on the number osteoclast seen in 10 random fields (B; *, $P < 0.005$ compared with culture with RANKL only).

Published OnlineFirst January 30, 2015; DOI: 10.1158/1541-7786.MCR-14-0492

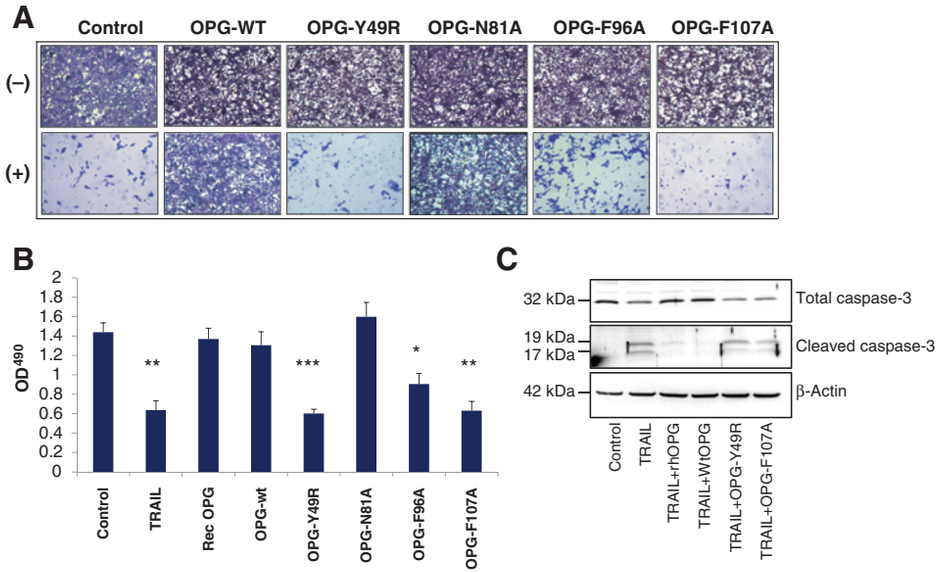

Figure 4.
Apoptosis assay to determine abrogation of TRAIL binding by OPG-mutants. MDA-MB-435 cells were cultured in the presence of 100 ng of TRAIL and 200 ng of OPG-wt or OPG-mutants. As a positive control, MDA-MB-435 cells were cultured with TRAIL alone. After 24 hours, MDA-MB-435 cells were either fixed in 3.7% paraformaldehyde and then stained with 0.05% Crystal violet for 30 minutes and viewed using a light microscope (×100; A) or cultured with 20 μL of the solution 3-(4,5-dimethylthiazol-2-yl)-5-(3-carboxymethoxyphenyl)-2-(4-sulfophenyl)-2H-tetrazolium, inner salt (MTS) for 2 hours, and then measured at an absorbance of 490 nm (B; *, $P < 0.05$; **, $P < 0.005$; ***, $P < 0.001$, compared with control). To determine downstream activity of TRAIL function, a human osteolytic cancer cell line, PC3, was cultured in a combination of TRAIL and OPG^{wt} or OPG^{mut} (Y49R or F107A) for 3 hours. Cells lysates were prepared by harvesting the cultures and Western blot analysis was performed for cleaved caspase-3 activity (C).

osteolytic damage without inhibiting TRAIL-induced apoptosis of cancer cells suggesting a strong therapeutic potential.

Osteoprotegerin also binds to TRAIL with similar affinity as with RANKL (24, 25), and therefore, OPG treatment raises the concern that it may affect the function of TRAIL. TRAIL is a cytokine expressed on the surface of tumor-infiltrating macrophages that induce apoptosis, specifically in malignant cells via interactions with the death receptors DR4 and DR5 (26). Although a precise mechanism by which TRAIL specifically induces death of transformed cells is not known, a substantial role for TRAIL has been established as a critical effector molecule in tumor immunosurveillance (27–31), and TRAIL-deficient mice suffer from increased susceptibility to tumor initiation and metastases (32). These studies highlight the importance of TRAIL and

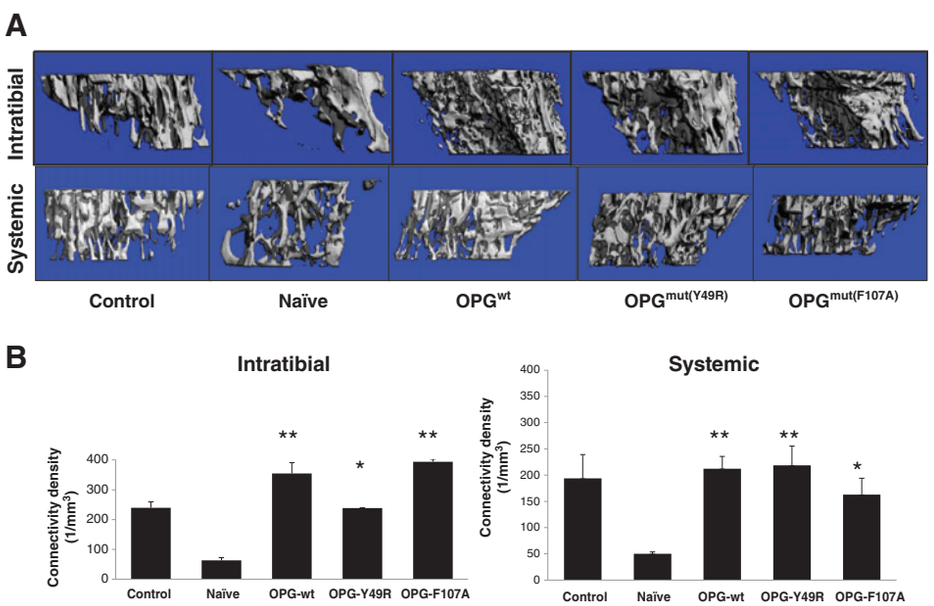

Figure 5.
Micro-CT assessment to determine the potential of OPG^{mut} in inhibiting tumor-induced osteolytic damage. Nude mice were injected intra-tibially with approximately 1×10^5 osteolytic prostate cancer cell line PC3. Twenty-four hours later, approximately 3×10^5 MSC overexpressing OPG^{wt}, OPG^{mY49R}, or OPG^{mF107A} were injected into the same tibia for intratumoral administration and by tail vein injection for systemic administration. Mice from both routes of MSC administration were sacrificed 14 days post MSC therapy and tibia were collected for micro-CT analysis to determine changes in the overall trabecular architecture (A) and connectivity density (B; *, $P < 0.05$; **, $P < 0.01$ compared with Naïve).

Published OnlineFirst January 30, 2015; DOI: 10.1158/1541-7786.MCR-14-0492

raise the concern that therapeutic administration of OPG might also diminish host immune defense mechanisms against malignant cells. Thus, the newly developed and characterized OPG mutants in this study will have the potential to overcome this limitation and concern.

Osteoprotegerin and RANK are members of the TNF-R superfamily, whereas RANKL and TRAIL are members of the TNF superfamily. The crystal structures of RANKL/OPG and TRAIL/DR5 complex have been resolved and the atomic models demonstrate conserved structural features of their respective superfamilies (33–37). Proteins in the TNF-R family adopt the elongated structures characterized by variable numbers of cysteine-rich domains (CRD) that form a scaffold of disulfide bridges (38) where the DR5 and OPG contains two and four CRDs, respectively. Monomers of both RANKL and TRAIL contain two antiparallel β-pleated sheets that form a β-sandwich as a core scaffold, which interact with adjacent subunits in a head-to-tail fashion to form a bell-shaped homotrimer (33–36). The elongated receptors fit into the grooves of adjacent protomers of the homotrimeric ligands, and this particular mode of interaction was demonstrated by the crystal structure of TRAIL/DR5 and RANKL/OPG (34, 35). Because of this conserved mode of interaction between the TNF and TNF-R family members, we hypothesized that OPG also shared a similar mode of interaction with TRAIL. Conservation in residues among family members is an indication of their functional importance; hence, it is plausible that the amino acid loop of TRAIL might also interact with the conserved residues in OPG in a similar manner. Because RANKL lacks this elongated loop structure, we predicted that the amino acid loop of TRAIL may provide a unique interaction with OPG and mutations on OPG residues that bind to TRAIL would generate OPG variants that will inhibit osteoclastogenesis but not TRAIL-mediated apoptosis of cancer cells. The crystal structure of OPG in complex with RANKL indicated that CRD2 and CRD3 of OPG play substantial roles in binding of OPG and RANKL, where the binding interface consists of two binding sites: site-1 identifying amino acid loop 50s (H47-L65) in CRD2 and site-2 indentifying amino acid loop 90s (A90-L98) in CRD3 (39). Of the mutants generated and characterized for therapeutic bone remodeling, mutant Y49R falls within binding site-1 and mutant F96R falls within binding site-2. However, mutant F107A does not fall within these binding sites yet resulted in significant abolishment of TRAIL binding. It remains possible that conformational changes in the amino acid F107 to F107A may have altered the binding that may have been retained in full-length OPG protein as opposed to truncated OPG containing CRDs.

Results of the *in vitro* studies also confirmed that despite mutagenesis at amino acids, based on interactive domain analysis, abolishment of TRAIL-binding domains in three of the mutants did not affect binding of RANKL to the OPG mutants. In the osteoclast assay, all recombinant OPG proteins significantly inhibited RANKL-mediated osteoclastogenesis confirming functionality of the mutated proteins. When functionally testing for TRAIL-binding activity, the OPG-mutant N81A strongly inhibited TRAIL-mediated apoptosis, similar to wild-type OPG indicating that despite the amino acid substitution, the binding affinity of OPG to TRAIL was retained. However, OPG mutants Y49R, F96A, and F107A demonstrated a significant decrease in TRAIL binding, which resulted in a significant decrease in cell viability. Furthermore, results of the *in vivo* studies provided key evidence confirming functional activity of these two OPG mutants in a preclinical mouse model of a bone disseminated osteolytic tumor demonstrated protection from bone destruction in both trabecular architecture and connectivity density.

Realizing the therapeutic potential of OPG in bone remodeling for tumor-induced osteolytic damage, much effort has gone to its clinical utility. In this study, we proposed the use of a novel OPG-mutant protein against cancer-induced osteolysis while potentially not interfering with TRAILs ability to induce apoptosis in cancer cells. Often times, epithelial carcinomas such as that of breast and prostate metastasize to the spine and long bones causing severe bone damage. With OPG being the native inhibitory protein of osteoclastogenesis, using this protein in conditions where there is severe osteolysis due to an imbalance in the RANKL/RANK/OPG signaling triad can potentially result in increased bone healing and low toxicity. In this regard, soluble RANK and antibodies targeting RANK have shown to be effective (40, 41), but toxicity remains an issue and therefore, direct site injection of OPG^{mut}, abolished in TRAIL binding by cell/gene therapy approach whereby low, yet sustained concentration of OPG can be systemically released to inhibit aggressive osteolytic damage. Moreover, the fact that the OPG mutants possess an altered TRAIL-binding domain would potentially allow endogenous TRAIL to target transformed cells. Furthermore, exogenous TRAIL therapy can be combined with the proposed OPG^{mut} therapy to diminish both osteolytic burden and tumor cell killing. In many advanced osteolytic malignancies where osteolytic lesions exist throughout the skeleton, a systemic approach will be more beneficial. In this context, it is noteworthy that used MSC is currently being tested in clinical studies (42).

Taken together, the current study demonstrates that RANKL-OPG-TRAIL molecular triad may be a valid target to develop novel therapy, particularly for tumor-associated bone destruction. The potential therapeutic application of the variant OPG that effectively inhibits osteoclastogenesis by retaining RANKL binding, while abolishing TRAIL binding, will be beneficial in malignant osteolytic bone pathologies encountered in breast cancer, prostate cancer, and multiple myeloma. The novel variants of OPG presented here may be used in therapeutic applications either as purified protein or by gene-based approaches through cell and gene therapy applications depending on the required duration of the therapy. Both OPG and TRAIL have been tested in preclinical settings and both proteins were well tolerated when used to treat pathologic conditions (43, 44). Furthermore, as studies have shown cells from human osteolytic malignancies such as U266, RPMI8226, MDA-MB-231 are sensitive to TRAIL (13, 45, 46) using OPG therapy in combination with TRAIL should result in the protection of bone from aggressive osteoclast damage and increase cancer cell death due to cytotoxic effects of TRAIL.

Disclosure of Potential Conflicts of Interest

No potential conflicts of interest were disclosed.

Authors' Contributions

Conception and design: J.T. Higgs, J.S. Jarboe, S. Ponnazhagan

Development of methodology: J.T. Higgs, J.S. Jarboe, D. Chanda, S. Ponnazhagan

Acquisition of data (provided animals, acquired and managed patients, provided facilities, etc.): J.T. Higgs, J.S. Jarboe, JH Lee, C. Deivanayagam, S. Ponnazhagan

Analysis and interpretation of data (e.g., statistical analysis, biostatistics, computational analysis): J.T. Higgs, J.S. Jarboe, JH Lee, S. Ponnazhagan

Writing, review, and/or revision of the manuscript: J.T. Higgs, JH Lee, S. Ponnazhagan

Administrative, technical, or material support (i.e., reporting or organizing data, constructing databases): S. Ponnazhagan
Study supervision: C. Deivanayagam, S. Ponnazhagan

Grant Support

This work was financially supported by NIH grants AR050251, AR560948, CA132077, CA133737, P30 AR046031, and P30 AR48311, and DoD grant DoD-BC101411.

The costs of publication of this article were defrayed in part by the payment of page charges. This article must therefore be hereby marked *advertisement* in accordance with 18 U.S.C. Section 1734 solely to indicate this fact.

Received September 9, 2014; revised January 13, 2015; accepted January 18, 2015; published OnlineFirst January 30, 2015.

References

1. Khosla S. Minireview: the OPG/RANKL/RANK system. Endocrinology 2001;142:5050–5.
2. Maginn EN, Browne PV, Hayden P, Vandenberghe E, MacDonagh B, Evans P, et al. PBOX-15, a novel microtubule targeting agent, induces apoptosis, upregulates death receptors, and potentiates TRAIL-mediated apoptosis in multiple myeloma cells. Br J Cancer 2011;104:281–9.
3. Suda T, Takahashi N, Udagawa N, Jimi E, Gillespie MT, Martin TJ. Modulation of osteoclast differentiation and function by the new members of the tumor necrosis factor receptor and ligand families. Endocr Rev 1999; 20:345–57.
4. Hofbauer LC, Khosla S, Dunstan CR, Lacey DL, Spelsberg TC, Riggs BL. Estrogen stimulates gene expression and protein production of osteoprotegerin in human osteoblastic cells. Endocrinology 1999;140:4367–70.
5. Hofbauer LC, Gori F, Riggs BL, Lacey DL, Dunstan CR, Spelsberg TC, et al. Stimulation of osteoprotegerin ligand and inhibition of osteoprotegerin production by glucocorticoids in human osteoblastic lineage cells: potential paracrine mechanisms of glucocorticoid-induced osteoporosis. Endocrinology 1999;140:4382–9.
6. Itonaga I, Fujikawa Y, Sabokbar A, Murray DW, Athanasou NA. Rheumatoid arthritis synovial macrophage-osteoclast differentiation is osteoprotegerin ligand-dependent. J Pathol 2000;192:97–104.
7. Yasuda H, Shima N, Nakagawa N, Yamaguchi K, Kinosaki M, Mochizuki S, et al. Osteoclast differentiation factor is a ligand for osteoprotegerin/osteoclastogenesis-inhibitory factor and is identical to TRANCE/RANKL. Proc Natl Acad Sci U S A 1998;95:3597–602.
8. Simonet WS, Lacey DL, Dunstan CR, Kelley M, Chang MS, Lüthy R, et al. Osteoprotegerin: a novel secreted protein involved in the regulation of bone density. Cell 1997;89:309–19.
9. Pettersen EF, Goddard TD, Huang CC, Couch GS, Greenblatt DM, Meng EC, et al. UCSF Chimera–a visualization system for exploratory research and analysis. J Comput Chem 2004;25:1605–12.
10. Emsley P, Cowtan K. Coot: model-building tools for molecular graphics. Acta Crystallogr D Biol Crystallogr 2004;60:2126–32.
11. Chanda D, Kumar S, Ponnazhagan S. Therapeutic potential of adult bone marrow-derived mesenchymal stem cells in diseases of the skeleton. J Cell Biochem 2010;111:249–57.
12. Szafran AA, Folks K, Warram J, Chanda D, Wang D, Zinn KR. Death receptor 5 agonist TRA8 in combination with the bisphosphonate zoledronic acid attenuated the growth of breast cancer metastasis. Cancer Biol Ther 2009;8:1109–16.
13. Zhu L, Huang X, Choi KY, Ma Y, Zhang F, Liu G, et al. Real-time monitoring of caspase cascade activation in living cells. J Control Release 2012;163: 55–62.
14. Lacey DL, Timms E, Tan HL, Kelley MJ, Dunstan CR, Burgess T, et al. Osteoprotegerin ligand is a cytokine that regulates osteoclast differentiation and activation. Cell 1998;93:165–76.
15. Kitazawa S, Kitazawa R. RANK ligand is a prerequisite for cancer-associated osteolytic lesions. J Pathol 2002;198:228–36.
16. Thomas RJ, Guise TA, Yin JJ, Elliott J, Horwood NJ, Martin TJ, et al. Breast cancer cells interact with osteoblasts to support osteoclast formation. Endocrinology 1999;140:4451–58.
17. Wittrant Y, Theoleyre S, Chipoy C, Padrines M, Blanchard F, Heymann D, et al. RANKL/RANK/OPG: new therapeutic targets in bone tumours and associated osteolysis. Biochim Biophys Acta 2004;1704:49–57.
18. Corey E, Brown LG, Kiefer JA, Quinn JE, Pitts TE, Blair JM, et al. Osteoprotegerin in prostate cancer bone metastasis. Cancer Res 2005;65:1710–8.
19. Croucher PI, Shipman CM, Lippitt J, Perry M, Asosingh K, Hijzen A, et al. Osteoprotegerin inhibits the development of osteolytic bone disease in multiple myeloma. Blood 2001;98:3534–40.
20. Morony S, Capparelli C, Sarosi I, Lacey DL, Dunstan CR, Kostenuik PJ. Osteoprotegerin inhibits osteolysis and decreases skeletal tumor burden in syngeneic and nude mouse models of experimental bone metastasis. Cancer Res 2001;61:4432–6.
21. Vanderkerken K, De Leenheer E, Shipman C, Asosingh K, Willems A, Van Camp B, et al. Recombinant osteoprotegerin decreases tumor burden and increases survival in a murine model of multiple myeloma. Cancer Res 2003;63:287–9.
22. Zhang J, Dai J, Qi Y, Lin DL, Smith P, Strayhorn C, et al. Osteoprotegerin inhibits prostate cancer-induced osteoclastogenesis and prevents prostate tumor growth in the bone. J Clin Invest 2001;107:1235–44.
23. Body JJ, Greipp P, Coleman RE, Facon T, Geurs F, Fermand JP, et al. A phase I study of AMGN-0007, a recombinant osteoprotegerin construct, in patients with multiple myeloma or breast carcinoma related bone metastases. Cancer 2003;97:887–92.
24. Emery JG, McDonnell P, Burke MB, Deen KC, Lyn S, Silverman C, et al. Osteoprotegerin is a receptor for the cytotoxic ligand TRAIL. J Biol Chem 1998;273:14363–7.
25. Vitovski S, Phillips JS, Sayers J, Croucher PI. Investigating the interaction between osteoprotegerin and receptor activator of NF-kappaB or tumor necrosis factor-related apoptosis-inducing ligand: evidence for a pivotal role for osteoprotegerin in regulating two distinct pathways. J Biol Chem 2007;282:31601–9.
26. Griffith TS, Wiley SR, Kubin MZ, Sedger LM, Maliszewski CR, Fanger NA. Monocyte-mediated tumoricidal activity via the tumor necrosis factor-related cytokine, TRAIL. J Exp Med 1999;189:1343–54.
27. Smyth MJ, Cretney E, Takeda K, Wiltrout RH, Sedger LM, Kayagaki N, et al. Tumor necrosis factor-related apoptosis-inducing ligand (TRAIL) contributes to interferon gamma-dependent natural killer cell protection from tumor metastasis. J Exp Med 2001;193:661–70.
28. Takeda K, Hayakawa Y, Smyth MJ, Kayagaki N, Yamaguchi N, Kakuta S, et al. Involvement of tumor necrosis factor-related apoptosis-inducing ligand in surveillance of tumor metastasis by liver natural killer cells. Nat Med 2001;7:94–100.
29. Takeda K, Smyth MJ, Cretney E, Hayakawa Y, Yamaguchi N, Yagita H, et al. Involvement of tumor necrosis factor-related apoptosis-inducing ligand in NK cell-mediated and IFN-gamma-dependent suppression of subcutaneous tumor growth. Cell Immunol 2001;214:194–200.
30. Zerafa N, Westwood JA, Cretney E, Mitchell S, Waring P, Iezzi M, et al. Cutting edge: TRAIL deficiency accelerates hematological malignancies. J Immunol 2005;175:5586–90.
31. Takeda K, Smyth MJ, Cretney E, Hayakawa Y, Kayagaki N, Yagita H, et al. Critical role for tumor necrosis factor-related apoptosis-inducing ligand in immune surveillance against tumor development. J Exp Med 2002;195: 161–9.
32. Cretney E, Takeda K, Yagita H, Glaccum M, Peschon JJ, Smyth MJ. Increased susceptibility to tumor initiation and metastasis in TNF-related apoptosis-inducing ligand-deficient mice. J Immunol 2002;168: 1356–61.
33. Cha SS, Kim MS, Choi YH, Sung BJ, Shin NK, Shin HC, et al. 2.8 A resolution crystal structure of human TRAIL, a cytokine with selective antitumor activity. Immunity 1999;11:253–61.
34. Cha SS, Sung BJ, Kim YA, Song YL, Kim HJ, Kim S, et al. Crystal structure of TRAIL-DR5 complex identifies a critical role of the unique frame insertion in conferring recognition specificity. J Biol Chem 2000;275: 31171–7.
35. Hymowitz SG, Christinger HW, Fuh G, Ultsch M, O'Connell M, Kelley RF, et al. Triggering cell death: the crystal structure of Apo2L/TRAIL in a complex with death receptor 5. Mol Cell 1999;4:563–71.

Published OnlineFirst January 30, 2015; DOI: 10.1158/1541-7786.MCR-14-0492

36. Lam J, Nelson CA, Ross FP, Teitelbaum SL, Fremont DH. Crystal structure of the TRANCE/RANKL cytokine reveals determinants of receptor-ligand specificity. J Clin Invest 2001;108:971–9.
37. Mongkolsapaya J, Grimes JM, Chen N, Xu XN, Stuart DI, Jones EY, et al. Structure of the TRAIL-DR5 complex reveals mechanisms conferring specificity in apoptotic initiation. Nat Struct Biol 1999;6:1048–53.
38. Naismith JH, Devine TQ, Kohno T, Sprang SR. Structures of the extracellular domain of the type I tumor necrosis factor receptor. Structure 1996;4:1251–62.
39. Nelson CA, Warren JT, Wang MW, Teitelbaum SL, Fremont DH. RANKL Employs Distinct Binding Modes to Engage RANK and the Osteoprotegerin Decoy Receptor. Structure 2012;20:1971–82.
40. Cummings SR, San Martin J, McClung MR, Siris ES, Eastell R, Reid IR, et al. Denosumab for prevention of fractures in postmenopausal women with osteoporosis. N Engl J Med 2009;361:756–65.
41. Zhou Z, Chen C, Zhang J, Ji X, Liu L, Zhang G, et al. Safety of denosumab in postmenopausal women with osteoporosis or low bone mineral density: a meta-analysis. Int J Clin Exp Pathol 2014;7:2113–22.
42. Gopal K, Amirhamed HA, Kamarul T. Advances of human bone marrow-derived mesenchymal stem cells in the treatment of cartilage defects: a systematic review. Exp Biol Med 2014;239:663–9.
43. Zierhut ML, Gastonguay MR, Martin SW, Vicini P, Bekker PJ, Holloway D, et al. Population PK-PD model for Fc-osteoprotegerin in healthy postmenopausal women. J Pharmacokinet Pharmacodyn 2008;35:379–9.
44. Doi T, Murakami H, Ohtsu A, Fuse N, Yoshino T, Yamamoto N, et al. Phase 1 study of conatumumab, a pro-apoptotic death receptor 5 agonist antibody, in Japanese patients with advanced solid tumors. Cancer Chemother Pharmacol 2011;68:733–7.
45. Shipman CM, Croucher PI. Osteoprotegerin is a soluble decoy receptor for tumor necrosis factor-related apoptosis-inducing ligand/Apo2 ligand and can function as a paracrine survival factor for human myeloma cells. Cancer Res 2003;63:912–6.
46. Labrinidis A, Diamond P, Martin S, Hay S, Liapis V, Zinonos I, et al. Apo2L/TRAIL inhibits tumor growth and bone destruction in a murine model of multiple myeloma. Clin Cancer Res 2009;15:1998–2009.

Published OnlineFirst January 30, 2015; DOI: 10.1158/1541-7786.MCR-14-0492

Molecular Cancer Research

Variants of Osteoprotegerin Lacking TRAIL Binding for Therapeutic Bone Remodeling in Osteolytic Malignancies

Jerome T. Higgs, John S. Jarboe, Joo Hyoung Lee, et al.

Mol Cancer Res 2015;13:819-827. Published OnlineFirst January 30, 2015.